

UCLA

UCLA Electronic Theses and Dissertations

Title

Meniscus Shape Engineering Through Micro and Nano Fabrication

Permalink

<https://escholarship.org/uc/item/057587tb>

Author

Liu, Tingyi

Publication Date

2014

Peer reviewed|Thesis/dissertation

UNIVERSITY OF CALIFORNIA

Los Angeles

Meniscus Shape Engineering Through Micro and Nano Fabrication

A dissertation submitted in partial satisfaction of the
requirements for the degree Doctor of Philosophy
in Mechanical Engineering

by

Tingyi Liu

2014

© Copyright by

Tingyi Liu

2014

ABSTRACT

Meniscus Shape Engineering Through Micro and Nano Fabrication

by

Tingyi Liu

Doctor of Philosophy in Mechanical Engineering

University of California, Los Angeles, 2014

Professor Chang-Jin Kim, Chair

Realizing the dominance of surface tensional forces helps us understand many phenomena in nature and industrial processes where the critical feature size is below a few millimeters. Causing many unfavorable phenomena in engineering practice, a liquid meniscus can also be purposely engineered to produce unmatched properties for useful applications. Surface tension and contact angles are two major parameters describing a meniscus in contact with solid and vapor. We first study the meniscus under different vapor and solid conditions to advance the knowledge of the meniscus behavior. We then show three novel examples of modifying surface conditions to certain microscale details with micro and nano fabrication techniques so that the engineered meniscus shape manifests dramatic improvements that cannot be achieved otherwise.

The dissertation of Tingyi Liu is approved.

Robert Thomas M'Closkey

Chih-Kong Ken Yang

Chang-Jin Kim, Committee Chair

University of California, Los Angeles

2014

I dedicate my dissertation to
my families for their unconditional love and endless support
my teachers and mentors for their comprehensive guidance
my adversaries for their pressure that forces me better

TABLE OF CONTENTS

ABSTRACT	ii
TABLE OF CONTENTS	v
LIST OF FIGURES	ix
LIST OF TABLES.....	xiii
NOMENCLATURE	xiv
ACKNOWLEDGEMENTS.....	xvi
VITA.....	xix
Chapter 1 Introduction.....	1
1.1 Backgrounds	1
1.1.1 Significance of Liquid Surface Tension at Micro Scale.....	1
1.1.2 Liquid Meniscus Shapes: Young-Laplace Equation	2
1.1.3 Liquid Meniscus in Contact with Solid: Young’s Equation.....	2
1.2 Applications of Meniscus Shape Engineering and Challenges	3
1.3 Scope of the Research.....	5
1.4 References.....	6
Chapter 2 Characterization of Liquid Metal Galinstan®	7
2.1 Introduction.....	7
2.2 Experiment Design	9
2.2.1 Contact Angles of Galinstan® on Different Materials.....	9
2.2.2 Surface Tension of Galinstan® under Controlled Oxidation	10
2.3 Results and Discussion	11
2.3.1 Contact Angles of Galinstan® on Different Materials.....	11
2.3.2 Surface Tension of Galinstan® under Controlled Oxidation	13
2.4 Summary.....	15
2.5 References.....	16
Chapter 3 Generalized Cassie-Baxter Model	20
3.1 Introduction.....	20
3.1.1 Cassie-Baxter (CB) Model for Contact Angles on Structured Surfaces	21
3.1.2 Existing Modified CB Models for Dynamic Contact Angles.....	22
3.1.3 Existing Experimental Method to Measure Dynamic Contact Angles.....	23
3.1.4 Limitations of Existing Experimental Studies on Contact Angle Hysteresis.....	24
3.1.5 Summary of Our Approach	26
3.2 Theory.....	27
3.2.1 Why the Original CB model Fails to Predict Dynamic Contact Angles	27

3.2.2	Modified Cassie-Baxter Model for 2-D Contact Line Sliding	28
3.2.3	Generalization to 3-D by Introducing Line Solid Fraction.....	30
3.3	Experiments	32
3.4	Results and Discussion	33
3.4.1	Verification of Generalized 2-D CB Model	33
3.4.2	Verification of Generalized 3-D CB Model	36
3.5	Future Works	38
3.6	Conclusions.....	38
3.7	References.....	39
Chapter 4	Electrostatically Driven Rotary Stage on Conductive Liquid Bearings	42
4.1	Introduction.....	42
4.1.1	Existing Micro Bearings for Rotation and Their Limitations.....	44
4.1.1.1	Solid-Solid Contact Bearings	44
4.1.1.2	Gas-Lubricated Bearings	44
4.1.1.3	Liquid Bearings	45
4.1.2	Difficulties in Power Transmission to Rotating Components	45
4.2	Theory and Design.....	46
4.2.1	Overall Design.....	46
4.2.2	Engineering Meniscus Shape to Form Liquid Rings.....	47
4.2.2.1	Liquid Rings as a Mechanical Bearing.....	48
4.2.2.2	Liquid Rings: Static and Dynamic Friction.....	52
4.2.2.3	Liquid Rings as a Electrical Pathway	54
4.2.3	Actuation, Sensing, and Feedback Control	55
4.2.3.1	Electrostatic Actuation via Voltage Control Variable Capacitance	55
4.2.3.2	Design of Bottom Driven Electrodes for Actuation and Sensing.....	60
4.3	Experiments	61
4.3.1	Fabrication and Assembly	61
4.3.2	Tests.....	63
4.4	Results and Discussion	64
4.4.1	Fabricated Device and Assembly	64
4.4.2	Electrostatic Actuation and Start-Up Torque	66
4.4.3	Position Capacitive Sensing and Feedback Control	68
4.5	Summary and Future Works	69
4.6	References.....	70
Chapter 5	Superomniphobic Surface Repellent to All Liquids	73
5.1	Introduction.....	73
5.1.1	Natural Super-repellent Surfaces.....	73
5.1.2	Current Engineered Super-repellent Surfaces	74
5.1.2.1	Superhydrophobic and Superoleophobic Surfaces	74
5.1.2.2	Slippery Liquid-Infused Porous Surfaces (SLIPS).....	75
5.1.2.3	Smooth Perfluorinated Hybrid Surfaces.....	76
5.1.3	Clarifying the Definition of Superomniphobicity	76
5.1.4	Our Design Philosophy Based on Current Limits	77
5.2	Theory and Design.....	78
5.2.1	Requirements to Achieve Superomniphobicity	78

5.2.1.1	Liquid Suspension by Micro and Nano Structures	78
5.2.1.2	Small Solid-Liquid Contact Fraction.....	82
5.2.1.3	Key Geometries to Maximize Repellency.....	84
5.2.2	Surface Structure Design and Material Selection.....	85
5.3	Experiments	86
5.3.1	Fabrication	86
5.3.1.1	Fabrication Process of Structured Surfaces	86
5.3.1.2	Process Conditions and Parameters	88
5.3.2	Liquids for Tests	90
5.3.3	Advancing and Receding Contact Angles	91
5.3.4	Roll-off Angle Measurement.....	92
5.3.5	Static and Dynamic Pressure Resistance	93
5.3.6	High Temperature Stabilities.....	93
5.3.7	Visualization of Meniscus Location	94
5.3.8	Wetting Transition from Capillary Condensation	94
5.4	Results and Discussion	95
5.4.1	Doubly Re-entrant SiO ₂ Surfaces	95
5.4.2	Liquids Beading on Superomniphobic SiO ₂ Surface	97
5.4.3	Apparent Advancing and Receding Contact Angles	98
5.4.4	Roll-off Angles	104
5.4.5	Static Pressure Resistance: the Break-in Pressure.....	104
5.4.6	Dynamic Pressure Resistance: Droplet Rebounding	106
5.4.7	High-temperature Superomniphobicity	107
5.4.8	Visualization of Meniscus Location on Doubly Re-entrant Structures.....	109
5.4.9	Minimization of Capillary Condensation by Enhanced Evaporation	110
5.5	Summary and Applications.....	110
5.6	References.....	112
Chapter 6	Artificial Cavities to Enhance Nucleate Boiling of Refrigerants.....	117
6.1	Introduction.....	117
6.1.1	Boiling Heat Transfer for Thermal Management.....	117
6.1.2	Challenges in using Refrigerants for Boiling Heat Transfer	118
6.2	Theory and Design.....	118
6.2.1	Meniscus Shape on Artificial Cavities for Enhanced Boiling Transfer	118
6.2.2	Theoretical Temperatures of Boiling Incipience and Dormancy	119
6.2.3	Shift of Saturation Curve by Capillary Condensation	121
6.3	Experiments	123
6.3.1	Chip Design and Fabrication	123
6.3.2	Pool Boiling Tests	125
6.4	Results and Discussion	126
6.4.1	Fabrication Results	126
6.4.2	Measurements of Nucleation Incipience	126
6.4.3	Restart Boiling Nucleation from Doubly Re-entrant Cavities.....	128
6.4.4	No Resume of Boiling Nucleation if Cooled Below Saturation Point	129
6.5	Summary.....	130
6.6	References.....	131

Chapter 7	Summaries and Future Directions.....	132
7.1	Dissertation Summaries	132
7.2	Future Research Directions.....	134

LIST OF FIGURES

Figure 1-1 Examples of meniscus shape engineering for micro and nano applications.....	4
Figure 2-1 Schematic of Galinstan advancing/receding contact angle measurement using captive needles in the glove box with < 1ppm oxygen	9
Figure 2-2 Three-phase contact regions of Galinstan [®] on a glass in ambient air (~20.9% oxygen).....	13
Figure 2-3 Surface tension of Galinstan [®] measured during the first 40 minutes of the quasi-static droplet growth	14
Figure 2-4 Deviation of the Galinstan [®] pendent drop profile from the Young-Laplace equation due to the elasticity of the oxidized skin	15
Figure 3-1 Cassie-state droplets advancing and receding on non-wetting structured surfaces	24
Figure 3-2 Top view of contact line motions	26
Figure 3-3 Force balances at contact lines on smooth and structured surfaces.....	29
Figure 3-4 Definition of line solid fraction from microscopic droplet boundary.....	31
Figure 3-5 Apparatus to create and measure 2-D contact line motion	33
Figure 3-6 Snapshots of menisci above (a) receding and (b) advancing contact line, overlapping in time sequence on a micro-grating surface with solid fraction $f_s = 0.5$ and pitch $P = 200 \mu\text{m}$	34
Figure 3-7 Apparent and local contact angles measured from a high-speed image of water receding on a structured surface with $f_s = 0.5$	35
Figure 3-8 Apparent receding contact angles measured on surfaces with different f_s are compared with various models.....	35
Figure 3-9 Comparing apparent receding contact angles of water reported in literature (symbols) and the modified Cassie-Baxter equation (Eq. 3.16) generalized by us (lines)	37
Figure 4-1 Schematic of the electrostatic bottom-driven rotary stage on liquid-rings bearings	46
Figure 4-2 Formation of stable liquid rings.....	48
Figure 4-3 Cross-sectional view of the rotary stage	49

Figure 4-4 Liquid-ring groove with different width on the rotor and the substrate	52
Figure 4-5 Distortion of the contact line lead to asymmetric of the meniscus.....	53
Figure 4-6 Electrical and sensing pathways provided by the liquid-ring bearings	55
Figure 4-7 Equivalent lumped circuit of an electrostatic transducer.....	56
Figure 4-8 Electrostatic side-driving configuration.....	57
Figure 4-9 Electrostatic bottom-driving configuration.....	59
Figure 4-10 Equivalent circuit of the sensing path through actuation electrodes on stator and the rotor.....	61
Figure 4-11 Process flows to fabricate (a) the substrate, (b) the rotor, and (c) the stators	62
Figure 4-12 3-D illustration of process to fabricate rotor (similar for the substrate as well).....	63
Figure 4-13 Fabricated rotary stage and assembly	64
Figure 4-14 Rotor-substrate gap controlled through liquid volume to form the liquid ring	65
Figure 4-15 Schematic of actuation, sensing and feedback circuit	69
Figure 4-16 Phase of impedance measured at different rotor positions	69
Figure 5-1 Liquid suspension on surface structures of three different topologies	80
Figure 5-2 Relationship between intrinsic contact angle θ_Y and different surface structures for successful liquid suspension	81
Figure 5-3 Relationship between apparent contact angle θ^* and solid fraction f_s for ideal Cassie state droplets with intrinsic contact angle θ_Y as a parameter	84
Figure 5-4 Designed surface of micro-posts with doubly re-entrant nano-overhangs	86
Figure 5-5 Process flow to fabricate (a) vertical, (b) re-entrant, and (c) doubly re-entrant posts.....	87
Figure 5-6 Process flow to fabricate doubly re-entrant posts with backside of the surface opened to atmosphere.....	95
Figure 5-7 SEM micrographs of the fabricated doubly re-entrant SiO_2 surface	96
Figure 5-8 SEM micrographs of all fabricated structured surfaces.....	96

Figure 5-9 Liquids beading up as droplets on the superomniphobic SiO ₂ surface.....	98
Figure 5-10 Apparent advancing and receding contact angles of the fourteen liquids measured on three liquid-repellent surfaces – our omniphobic surface and two control surfaces of the same nominal solid fraction ($f_s \sim 5\%$)	99
Figure 5-11 Illustration of why the contact-angle data of smaller-capillary-length liquids scatter more in Figure 5-10, using water and FC-72 droplets	102
Figure 5-12 Relations of contact angles on smooth surface ($\cos \theta_Y$) and on a structured surface ($\cos \theta^*$)	103
Figure 5-13 Roll-off angles of the fourteen liquids measured on the superomniphobic SiO ₂ surface	104
Figure 5-14 Break-in pressure measured from an evaporating FC-72 droplet.....	106
Figure 5-15 Robust repellency of the structured SiO ₂ surface demonstrated by bouncing water, methanol, and FC-72 off the surface	107
Figure 5-16 Super-repellency of the reported surfaces under very high temperature	108
Figure 5-17 SEM images of an epoxy ball cured as a droplet on the doubly re-entrant posts.....	109
Figure 5-18 Summary of conditions to achieve liquid-repellent surfaces.....	111
Figure 6-1 Three types of cavities in literature to enhance boiling nucleation	119
Figure 6-2 Pressure-temperature relationship (p - T) of a boiling bubble	120
Figure 6-3 Schematic illustration of how the saturation equilibrium changes by capillary condensation.....	122
Figure 6-4 Normal saturation curve of a liquid-vapor system and a couple of curves shifted towards a higher saturation temperature due to the capillary condensation on a rough wetting surface	123
Figure 6-5 Design of boiling chips to study the nucleation dynamics	124
Figure 6-6 Process to fabricate boiling chip consists of doubly re-entrant cavities by micro and nano Si machining.....	124
Figure 6-7 Experimental setup of FC-72 pool boiling test.....	125
Figure 6-8 SEM micrograph of fabricated boiling chips.....	126
Figure 6-9 Comparison of liquid superheats required to maintain nucleation on different cavities ($n = 3$ for each experimental datum).....	128

Figure 6-10 Nucleation ceasing and resuming on doubly re-entrant cavities129

LIST OF TABLES

Table 2-1 Comparison of properties of Galinstan [®] and mercury	8
Table 2-2 Surface preparation of different materials tested for contact angles	10
Table 2-3 Contact angles of Galinstan [®] on different materials	12
Table 3-1 Summary of existing models elaborated to predict dynamic contact angles ...	23
Table 3-2 Line solid fraction λ_s used in Figure 3-9 for different surface structures and receding conditions.....	37
Table 4-1 Summary of COMSOL simulation on liquid-ring dynamic drag	54
Table 4-2 Start-up of rotary stages of different bearings.....	68
Table 5-1 Physical and chemical properties of the tested liquids.....	91
Table 5-2 Contact angles (°) of tested liquids measured on different smooth and structured surfaces in this report	100

NOMENCLATURE

γ – surface tension of the liquid, also called as liquid-air interfacial tension denoted as γ_{LV}

γ_{SV}, γ_{SL} – surface tension of the solid-vapor and solid-liquid interface

Δp – pressure difference across the meniscus

p_l, p_a – pressure of the liquid and pressure of the atmosphere

θ – contact angle of liquid on solid surface

θ_Y – intrinsic contact angle, i.e., Young's angle

θ_A, θ_R –advancing and receding contact angle

$\theta^*, \theta_A^*, \theta_R^*$ – apparent static, advancing, and receding contact angle

α – meniscus angle formed between the liquid-air interface at the edge of the groove and the base of the groove

f_s, f_g –liquid-solid and liquid-gas contact fraction of a composite surface, also known as the solid fraction and gas fraction

λ_s –line solid fraction defined as the ratio of the three-phase contact line to the apparent contact line

τ – frictional force acting on the three-phase contact line to account for the hysteresis

P – pitch of the periodic geometries

φ – rotational angle of the rotor

r – radius of the groove

R – radius of curvature of a curve meniscus; radius of the electrodes for actuation

h – distance between the rotor and substrate

g – electrostatic gap between the electrode rotor and stator

W, H, D – geometric parameters, standing for the width, height and diameter, respectively

C_{ring} – total (including both inner and outer) perimeter of a liquid ring

k – spring constant of a spring, such as liquid-ring bearing

F_{support} – vertical supporting force to the rotor provided by the liquid-ring bearings

$F_{\text{electrostatic}}$ – electrostatic force for rotation

V – voltage applied across the rotor electrode and stator electrode

C – capacitance between two electrodes

ε – permittivity of the environment (i.e., in vacuum, $\varepsilon = \varepsilon_0 = 8.85 \times 10^{-12}$ F/m)

L – length notation used for scaling analysis

\mathcal{H} – the mean curvature of a three-dimensional surface, $\mathcal{H} = 1/2 \cdot (1/R_1 + 1/R_2)$

\mathcal{R} – the ideal gas constant, $\mathcal{R} = 8.31$ J/(mol·K)

$V_{m,l}$ – liquid molar volume, equals to the ratio of molar mass to mass density

$p_{v,eq}, T_{v,eq}$ – equilibrium vapor pressure and temperature (curved meniscus)

$p_{\text{sat}}, T_{\text{sat}}$ – saturation vapor pressure and temperature (flat meniscus)

ΔT – liquid superheat, i.e., the temperature difference over the saturation temperature

R_b, R_m, R_r – radius of curvature of the bubble, cavity mouth, and surface roughness

ΔT_{sat} – the shift of saturation temperature

h_{lv} – latent heat of vaporization

ACKNOWLEDGEMENTS

Foremost, I would like to express my deepest gratitude to my Ph.D. advisor Prof. CJ Kim, and I am so proud of being one of his students. He was extremely insightful to see my potential at the very beginning even when I just joined the lab for 2.5 months. As a mentor, he has a very unique way of training so that I was always pushed out of my comfort zone to explore something new. As a researcher, he set himself as an example to teach me how to always keep the big picture in mind while solving a problem and not to be drunk by small technological details. His emails, quick responses, and support even at late nights have always encouraged me to work harder. His continuous passion and strong belief in solving the problem has always encouraged me to overcome difficulties.

I would also like to thank Prof. Sungtaek Ju and Prof. Ken Yang for their support in developing the rotary stage. Their professional insight helped me find light in the hopeless difficulties. Their students were also very supportive, and communication was always pleasant. I would like to express my sincere appreciation to Prof. Robert M'Closkey for his kindness to be on my committee, his advice for my career, and his guidance me through proposal writing. I am very grateful to Prof. Bruce Dunn for his valuable comments and keen suggestions on my work of super-repellent surfaces. I would especially like to thank Prof. Laurent Pilon for his great regard for my career and welcoming encouragement in auditing his heat transfer course. I am deeply indebted to Prof. Ren Sun who started the UCLA-CSST Program and brought me to UCLA for the summer and winter program in 2008-2009 where I met lots of friend for life and career. His enthusiasm in cross-disciplinary research continuously inspires us to see a broadened world.

Many thanks go to my colleagues who shared the ups and downs of research with me these years. I am indebted to Dr. Prosenjit Sen, who mentored me at the beginning of my Ph.D. and taught me how to do research. I thank Dr. Guangyi Sun and Dr. Wook Choi for their training and valuable experience on microfabrication. I thank Dr. Gaurav Shah, Dr. Wyatt Nelson, Dr. Supin Chen, Dr. Janet Hur, and Mr. Zhiyu Chen for their help on all different kinds of seemingly small but critical issues throughout my early research. I thank Ms. Coco Huang and Ms. Bonhye Koo for our study times in the first and second year. I thank Mr. James Jenkins for his guidance to be a TA and patience in answering English-related questions. I really enjoyed the discussion of research and life with Mr. Muchen Xu, Mr. Ke Ding, and Mr. Wei-Yang Sun. I extend thanks to Mr. Ryan Freeman who did lots of proofreading for my paper.

I am truly thankful to my dear friend and roommate Mr. Chengjie Wang for the time we spend together: teaching me driving, rock-climbing, discussing research, etc. I also owe sincere and earnest thankfulness to all my friends met through CSST program and grew up together in these years: Ms. Lingyan Ran, Ms. Murong Lang, Mr. Yang Yang, Ms. Yan Jin, naming just a few. I would also like to acknowledge my high school friends, Mr. Shengyang Zhong, Mr. Jia Ning, and Mr. Pengliang Li, for our royal friendship and every happy reunion.

Finally, but most importantly, this dissertation would not have been possible without the support from my family. I owe sincere and earnest thankfulness to my parents who love me and support me at all times and at all aspects: success, upset, or difficulties. My immense thank go to Dr. Russell Fung, my cousin and friend, who gave me guidance throughout my Ph.D. from daily life to way of thinking. My deepest thanks extend to Ms.

Xiaoxiao Ma for her love and support. I feel so lucky to meet her at UCLA. Our laughs, long talks, and occasional stupid little fights have been lived within my heart. We not only stand by each other on good days but also stand even closer on bad days. When being with her, everything is beautiful and every moment is joyful.

VITA

- 2009 B. E., Electrical Engineering (with honors)
Zhengjiang University, Hangzhou, China
- 2011 M.S., Mechanical Engineering
University of California, Los Angeles, USA
- 2009-2014 Graduate Student Researcher
Teaching Assistant
Mechanical and Aerospace Engineering Department
University of California, Los Angeles

JOURNAL PUBLICATIONS

T. Liu and C.-J. Kim, "Turning any material super-repellent to all liquids," *Science* (under review)

G. Sun, T. Liu, P. Sen, W. Shen, C. Gudeman and C.-J. Kim, "Electrostatic Side-Drive Rotary Stage on Liquid-Ring Bearing," *J. Microelectromech. Syst.*, Vol. 23, Iss. 1, Feb. 2014, pp. 147-156.

T. Liu, P. Sen, and C.-J. Kim, "Characterization of Nontoxic Liquid-Metal Alloy Galinstan[®] for Applications in Micro Devices," *J. Microelectromech. Syst.*, Vol. 21, Iss. 2, April 2012, pp. 443-450.

CONFERENCE PUBLICATIONS & PRESENTATIONS

[It is noteworthy that the following Conferences of (1) Int. Conf. on Micro Electro Mechanical Systems (MEMS), (2) Int. Conf. on Solid-State Sensors, Actuators, and Microsystems (Transducers), and (3) Solid-State Sensor, Actuator, and Microsystems Workshop (Hilton Head) are one of the most highly-regarded conference publication in the area of Microsystems and MEMS. The acceptance rate is typically below 35% down to 10%.]

T. Liu^{*} and C.-J. Kim, "Microstructured SiO₂ Surface Repellant To Liquids without Coating," *IEEE Transducers '13*, Barcelona, Spain, June 2013, pp. 1609-1612, **ORAL**.

T. Liu^{*}, G. Sun, J. J. Kim, C.-K. K. Yang, and C.-J. Kim, "Electrostatic Bottom-Driven Rotary Stage on Multiple Conductive Liquid-Ring Bearings," *Proc. IEEE Int. Conf. MEMS*, Taipei, Taiwan, Jan. 2013, pp. 86-89, **ORAL**.

G. Sun^{*}, T. Liu, P. Sen, W. Shen, C. Gudeman, and C.-J. Kim, “Electrostatically Driven Rotor on Conductive Liquid Ring Bearings,” *Technical Digest, Solid-State Sensor, Actuator and Microsystems Workshop*, Hilton Head Island, SC, June 2012, pp. 78-81, **ORAL**.

T. Liu^{*}, P. Sen, and C.-J. Kim, “Characterization of Liquid-Metal Galinstan[®] for Droplet Applications”, *Proc. IEEE Int. Conf. MEMS*, Hong Kong, China, Jan. 2010, pp. 560-563, **POSTER**.

(* indicates the presenter)

PATENT

C.-J. Kim and T. Liu, “Liquid-Repellent Surfaces Made of Any Materials”, UC. Case No. 2014-186-1, Provisional No. 61/883.8 (Sep. 27, 2013).

Chapter 1 Introduction

1.1 Backgrounds

In the world of small organisms, lives are very different from ours. For example, water striders can walk on water surface; lotus leaves remain clean even in dirty environment; desert beetles collect water from moisture; naming just a few. One of the major differences of those small organisms compared to us is that they handle liquids in an efficient way for their scale so that they can survive in the small-scale world.

1.1.1 Significance of Liquid Surface Tension at Micro Scale

The seemingly magical phenomena in the microscale world are not by changes in physics principles but simply by changes in relative magnitude of forces. Unlike body forces such as gravitational forces and surface forces such as stress, surface tensional force is a line force and therefore scales much slower than other forces so that it becomes more significant with miniaturization. Surface tension of a liquid comes from the unbalanced forces across the interface, where the inner liquid molecules attract much stronger than the vapor molecules outside the liquid. Because of liquid surface tension, small water droplets bead up as pearls on lotus leaves [1] and water strider can walk on water's "tough" surface without sinking [2]. Examples of the strong effect of surface tension can also be found in daily life such as paper clips floating on water, ink wicking through the capillaries in a fountain pen, hair or beard stuck on blades, etc. Depending on the different surface wettability and pressure balance, liquid forms different liquid-vapor interfaces, i.e., meniscus shape, leading to different phenomena of beading or spreading, repelling or attracting, and rolling or flowing.

1.1.2 Liquid Meniscus Shapes: Young-Laplace Equation

Surface tension plays a major role in determination of the meniscus shape at equilibrium. With a large surface tension, the attraction from the liquid side is stronger and therefore the meniscus is more likely to curve more. The principal mathematical tool used to calculate the shape of the meniscus is the Young-Laplace equation [3] as follows,

$$\Delta p = \gamma \left(\frac{1}{R_1} + \frac{1}{R_2} \right) \quad (1.1)$$

where Δp is the pressure difference/jump across a liquid-vapor interface, aka. Laplace pressure, R_1 and R_2 are the radii of curvature and γ is the liquid surface tension. If the Δp is defined as the liquid pressure minus the vapor pressure, i.e., $\Delta p = p_l - p_v$, then the sign of R_1 and R_2 is defined to be positive if the center of the radius is within the liquid side and negative if it is on the vapor side. Note that R_1 and R_2 are not necessarily the principal radii of curvature as long as their planes are mutually orthogonal [4]. Because the Young-Laplace equation (Eq. 1.1) relates the liquid surface tension, meniscus geometries, and the pressure difference at each point along the interface, it can be used to predict the distorted meniscus shape due to other forces, e.g., gravitational forces (i.e., hydrostatic pressure) or electrostatic forces (i.e., electrostatic stress). Alternatively, if the shape of the interface can be measured experimentally, we can use Eq. 1.1 to determine the surface tension.

1.1.3 Liquid Meniscus in Contact with Solid: Young's Equation

Generally, when a liquid droplet is put in contact with a solid surface, two distinct equilibrium regimes may be found: complete wetting or partial wetting with a finite contact angle denoted as θ . In the case of complete wetting ($\theta \sim 0^\circ$), a liquid film is

formed and thus the meniscus is flat. In the case of partial wetting ($0^\circ < \theta < 180^\circ$), the droplet forms three-phase contact line defining a boundary within which the solid is wetted. The shape of the meniscus will display spreading ($0^\circ < \theta < 90^\circ$) or beading ($90^\circ < \theta < 180^\circ$). Ideally, for a chemically homogeneous, physically smooth and rigid surface, the static contact angle θ_Y is described by the Young's equation [5] as,

$$\cos\theta_Y = \frac{\gamma_{SV} - \gamma_{SL}}{\gamma} \quad (1.2)$$

where γ_{SV} , γ_{SL} , and γ are the interfacial tension between the solid-vapor, solid-liquid, and liquid-vapor interface, respectively. Note that γ is normally referred to as the liquid surface tension. This angle of contact is satisfied at each point along the contact line requiring that any local change of the interfacial tension will result in an adjustment of the contact angle and consequently the meniscus shape.

1.2 Applications of Meniscus Shape Engineering and Challenges

Due to the dominance of surface tensional forces in microscale, liquid manipulation is usually much more difficult in microscale compared to macroscale. However, proper engineering approach would allow modification of the meniscus shape by utilizing rather than suffering from the surface tension, providing unique opportunities to solve some problems in an elegantly simple way.

Moving a liquid at microscale is more difficult than in the macroscale mainly because macroscale methods that utilize gravity and pressure become inefficient in overcoming the pressure drop in microchannels. If the liquid is to be moved in discrete volumes, i.e., as droplets, surface tension would hinder the movement. Figure 1-1 summarizes several established ways to move liquid, especially droplets, efficiently. Figure 1-1(a) shows a

liquid droplet on a solid surface, whose chemical composition has a gradient, forms different contact angles on two ends and therefore move spontaneously due to the unbalanced surface tensional force [6], [7]. If the force gradient is of electrostatic in nature rather than chemical, liquid droplet can be moved similarly but by electrowetting forces [8], as shown in Figure 1-1(b). When the meniscus is confined by certain solid geometry, it requires much larger pressure for liquid to penetrate. As shown in Figure 1-1(c), superhydrophobic surfaces can be made by roughening hydrophobic material where liquid meniscus can be suspended on asperities and therefore freely rolling on the surface [1], [9]. Without using macroscale pressurized gas, liquid can be continuously pumped by microscale bubbles' directional growing and venting [10], as shown in Figure 1-1(d).

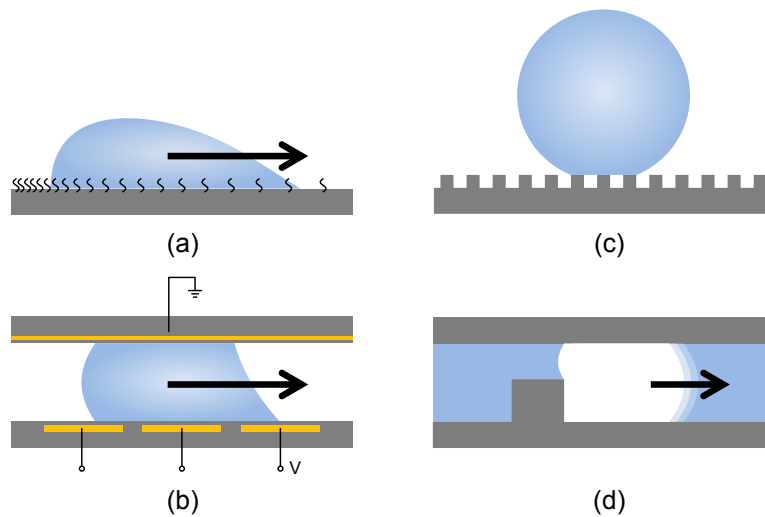


Figure 1-1 Examples of meniscus shape engineering for micro and nano applications. (a) Droplet movement enabled by chemical gradient induced difference contact angles formed on two sides of the droplet [6], [7]. (b) Droplet transportation in designed paths using electrowetting forces [8]. (c) Superhydrophobic surface generated by textured hydrophobic surfaces where droplet is suspended on surface structures [1], [9]. (d) Directional liquid pumping using bubble growth and venting [10].

The key challenge for meniscus shape engineering is how to induce the desired shapes within the design constraints, requiring solid understanding and educated intuition of physics in microscale as well as creative imagination for engineering design. With the data from similar examples unavailable, a slight shift of the critical parameter in design may lead to completely unexpected results. Therefore, it is important to visualize the development process and perform simple experiments whenever possible to better understand uncertain details in advance during the design stage. Because meniscus is very sensitive to all the phases it relates to (i.e., liquid, solid, and vapor), any deviation from the ideal conditions (e.g., contamination) may lead to the results unexpected in the original design. Finally, one needs to consider the limitations of materials and fabrication tools, while being resourceful, throughout the development process.

1.3 Scope of the Research

We focus on studying and engineering the two critical parameters of a meniscus, the surface tension and the contact angles, for which the central equations are given in Eq. 1.1 and 1.2. Because the interfaces we study normally involve all three phases, i.e., solid, liquid, and vapor, we can study and engineer the menisci by varying the conditions imposed on them. Chapters 2 to 6 present five different projects related to meniscus shape engineering: Chapters 2 and 3 study the scientific aspects of a meniscus shape with changing condition of vapor or solid, while Chapters 4 to 6 present three examples of meniscus engineering. Chapter 4 presents a rotary stage supported by low-friction liquid-ring bearings created through surface physical and chemical modification. Chapter 5 demonstrates the theory and realization of a truly superomniphobic surface, revising the

existing wetting theories and enabling any material to be super-repellent by micro and nano structuring of the solid surface with particular details. Chapter 6 shows artificial surface cavities that help refrigerants perform for nucleate boiling. Chapter 7 summarizes the dissertation and provides future research directions.

1.4 References

- [1] D. Quéré, “Non-sticking drops,” *Rep. Prog. Phys.*, vol. 68, no. 11, p. 2495, 2005.
- [2] X. Gao and L. Jiang, “Biophysics: Water-repellent legs of water striders,” *Nature*, vol. 432, no. 7013, pp. 36–36, Nov. 2004.
- [3] P. S. Laplace, *Traité de mécanique céleste*, vol. 4. de l’Imprimerie de Crapelet, 1805.
- [4] A. W. Adamson and A. P. Gast, *Physical Chemistry of Surfaces*, 6 edition. New York: Wiley-Interscience, 1997.
- [5] T. Young, “An Essay on the Cohesion of Fluids,” *Philos. Trans. R. Soc. Lond.*, vol. 95, pp. 65–87, Jan. 1805.
- [6] F. D. Dos Santos and T. Ondarçuhu, “Free-Running Droplets,” *Phys. Rev. Lett.*, vol. 75, no. 16, pp. 2972–2975, Oct. 1995.
- [7] S. Daniel, M. K. Chaudhury, and J. C. Chen, “Fast Drop Movements Resulting from the Phase Change on a Gradient Surface,” *Science*, vol. 291, no. 5504, pp. 633–636, Jan. 2001.
- [8] S. K. Cho, H. Moon, and C.-J. Kim, “Creating, transporting, cutting, and merging liquid droplets by electrowetting-based actuation for digital microfluidic circuits,” *J. Microelectromechanical Syst.*, vol. 12, no. 1, pp. 70–80, Feb. 2003.
- [9] D. Quéré, “Wetting and Roughness,” *Annu. Rev. Mater. Res.*, vol. 38, no. 1, pp. 71–99, 2008.
- [10] D. D. Meng and C.-J. Kim, “Micropumping of liquid by directional growth and selective venting of gas bubbles,” *Lab. Chip*, vol. 8, no. 6, pp. 958–968, 2008.

Chapter 2 Characterization of Liquid Metal Galinstan[®]

2.1 Introduction

For the excellent conductivities of a metal and the fluidic properties of a liquid, metals are often employed in their liquid state: mercury, gallium (alloy), aluminum, and tin, etc. At room temperature, however, the choice is significantly limited; mercury, used commonly for thermometers and electromechanical relays, remains the only liquid metal as an element. Gallium and many of its alloys are a liquid near but above room temperature. Although some laboratories may have produced some in-house, a room-temperature liquid metal has not become available until recently. Galinstan[®], an alloy of 68.5% Ga, 21.5% In, and 10.0% Sn, is a commercially available (from Geratherm[®] Medical AG in Germany and distributed by RG Medical Diagnostics in USA) nontoxic liquid-metal that replaces mercury mostly in thermometers [1]. Physical properties of Galinstan[®] and mercury [1], [2] are summarized in Table 2-1 for comparison. Like mercury, Galinstan[®] retains its liquid state well below 0°C. Its nontoxic nature and ultra low vapor pressure ($<10^{-6}$ Pa at 500°C) make Galinstan[®] a better substitute for mercury in many liquid-metal applications, e.g., electromechanical relays [3], coolants [4], and ion sources [5]. In microelectromechanical systems (MEMS), Galinstan[®] has already been used [6], [7] or is in line to replace mercury [8], [9]. It has, however, failed to produce many successful results in MEMS as initially anticipated, and mercury is still the common choice of liquid metal in research at room temperature. The main reason for the slow adoption in micro devices is the fast oxidation of Galinstan[®], as it was for gallium [10], making any study or development involving Galinstan[®] below millimeters difficult. In addition, several parameters important for microdevices are unavailable for this

relatively new material. Even worse, some information available on the Internet (e.g., that Galinstan[®] wets glass) lacks rigor and often misleads.

Table 2-1 Comparison of properties of Galinstan[®] and mercury

Property	Galinstan [®] [1]	Mercury [2]
Color	Silver	Silver
Odour	Odourless	Odourless
Boiling point	> 1300°C	356.72°C
Melting point	-19°C	-38.84°C
Vapor pressure	<10 ⁻⁶ Pa at 500 °C	0.16 Pa at 0°C, 36.38 Pa at 100°C
Density	6440 kg/m ³	13550 kg/m ³
Solubility	Insoluble	Insoluble
Viscosity	0.0024 Pa·s at 20°C	0.015 Pa·s
Thermal conductivity	16.5 W·m ⁻¹ ·K ⁻¹	8.30 W·m ⁻¹ ·K ⁻¹
Electrical Conductivity	2.30×10 ⁶ S/m	1 x 10 ⁶ S/m

Due to the dominance of the capillary effect at microscale, contact angles and surface tension are two key properties of a liquid used in MEMS, especially the droplet-based micro devices. The major challenge of characterizing Galinstan[®] lies in the fact that its surface oxidizes instantaneously in air, much more profound in microscale where the surface-to-volume ration is large. It has been found that, from my undergraduate research [11], [12], in order to obtain genuine properties not obscured by the surface oxidation, Galinstan[®] should be placed inside a glove box (VAC 101965 with oxygen and moisture sensors) of high-purity inert environment where the oxygen levels are controlled below 1 part per million (ppm) so that Galinstan[®] behaves like a true liquid rather than a gel. The surface tension of Galinstan[®] was measured by the pendent drop method to be 534.6±10.7 mN/m [11], [12]. However, no systematic study on contact angles has been reported so far and the effect of oxidation on Galinstan[®] surface tension has not been quantified. Those are the gaps we are going to fill in this chapter.

2.2 Experiment Design

2.2.1 Contact Angles of Galinstan[®] on Different Materials

Imitating the commercial instruments (e.g. First Ten Angstroms FTÅ200) which measure contact angles using drop shape analysis, we developed a setup inside the glove box for contact angle measurements of Galinstan[®], as schematically depicted in Figure 2-1. A syringe with liquid-metal compatible needle (Hamilton 50 μL syringe 1705RN and removable needle 7770-02 RN NDL with inner diameter 0.41 mm) was used to generate sessile droplets of Galinstan[®] on various solid surfaces.

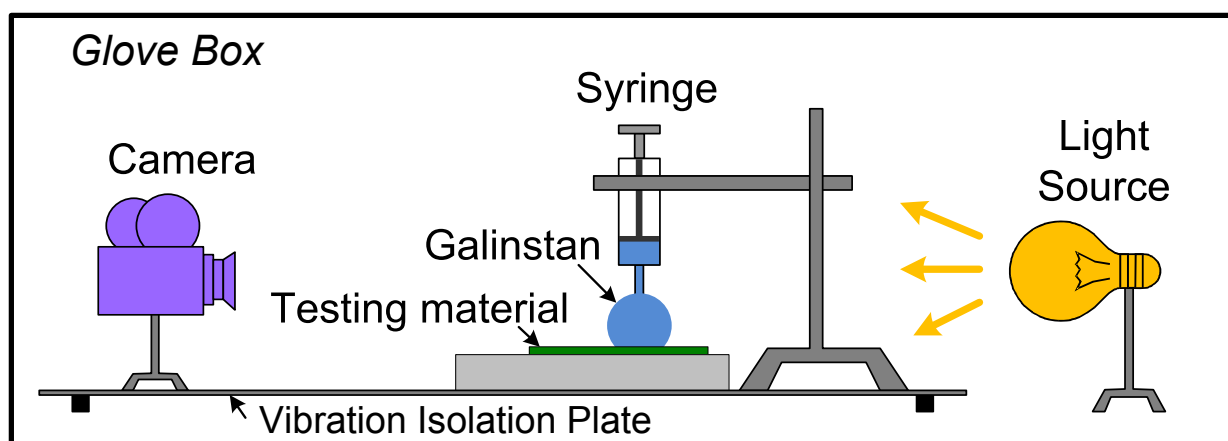


Figure 2-1 Schematic of Galinstan advancing/receding contact angle measurement using captive needles in the glove box with < 1 ppm oxygen

The experiments proceeded as follows. First, a captive Galinstan[®] drop was created by dispensing it manually from a syringe through the needle. The droplet was made much larger than the needle tip to minimize the surface distortion by the tip [13]. Second, the sessile droplet was expanded or contracted by pumping the liquid in and out of the syringe continuously and slowly ($\sim 0.25 \mu\text{L/s}$) to maintain quasi-static states, while recording the side views of the droplet with a video camera (Edmund Optics EO-0413C)

in audio video interleave (AVI) file format at 28 frames per second. Slow pumping of Galinstan[®] was more difficult than aqueous solutions (e.g. water), because liquid-metals have much larger surface tension and do not wet the needle material. Fresh Galinstan[®] was used for every test to prevent potential contamination. Finally, after the experiment was done, the video was inspected frame-by-frame and advancing and receding contact angles were obtained from the snapshot right before the contact line moved.

We measured the contact angles of Galinstan[®] on several solid materials commonly used in micro devices. Among metals, almost all of which chemically react with gallium and gallium alloys [14], tungsten was chosen for its chemical resistance. Mica was chosen for their well-known surface smoothness, despite its rare use in MEMS. Methods of surface preparation for all the materials tested are summarized in Table 2-2. After completing contact angle measurements, surface roughness was measured for all the tested materials using atomic force microscopy (AFM) on three different $1\ \mu\text{m} \times 1\ \mu\text{m}$ spots.

Table 2-2 Surface preparation of different materials tested for contact angles

Type	Material	Thickness	Preparation Method
Conductor	Tungsten	200 nm	Sputtered on silicon wafer
Insulator	Silicon nitride	1 μm	Low-stress LPCVD on silicon wafer
	Glass	1 mm	Degreased soda-lime microscope slide (Fisherfinest [®])
Polymer	Parylene	1 μm	Vapor deposition on microscope slide
	Teflon [®]	560 nm	Spin-coated on PECVD silicon nitride on ITO-coated glass
Mica	Phlogopite	500 μm	Cleaved from its natural form provided by Cogebi, Inc.
	Muscovite	400 μm	Cleaved from its natural form provided by Cogebi, Inc.

2.2.2 Surface Tension of Galinstan[®] under Controlled Oxidation

Following our previous work [11], [12], surface tension was measured by the pendant drop method, which the testing material and its substrate were removed from the contact

angle measurement setup of Figure 2-1 while a plumb bob that provides a reference vertical line in the camera view was added. To qualitatively study the effect of oxidation on Galinstan[®] surface tension, we also added a controlled valve that connects to atmosphere. Materials and analytical procedures are kept exactly the same as [11], [12] so that we can directly compare the surface tension of an oxidized Galinstan[®] with our previous oxygen-free results. To obtain certain O₂ level, we purposely turned off the build-in purifying system of the glove box and waited until the reading of the oxygen sensor stabilized so that the induced O₂ are maintained constant and equilibrated within the glove box.

2.3 Results and Discussion

2.3.1 Contact Angles of Galinstan[®] on Different Materials

Results of contact angle measurements of Galinstan[®] on different solid surfaces are summarized in Table 2-3 along with the roughness information of the surfaces obtained by AFM measurements. The contact angles were calculated with sub-pixel accuracy [15]. The roughness was quantified by different parameters interpreting the vertical deviations of the roughness profile from the mean line: R_q being the root mean square of the deviations; R_a being the arithmetic average of the absolute values; R_{max} being the maximum difference between the peaks and valleys; and surface area ratio being the ratio between the increased surface area (due to the roughness) and the perfectly flat surface. Galinstan[®] was found nonwetting on all surfaces tested.

However, we found that, once Galinstan[®] gets oxidized, the oxide shell, though thin, sticks on the surface and gives the illusion that Galinstan[®] wets almost all materials. To

emphasize the detrimental impact of oxidation on measuring the wetting properties of Galinstan[®], we measured its advancing and receding contact angles on glass in ambient air (~20.9% oxygen) as well, as shown in Figure 2-2. The experiment setup remained exactly the same except that the glove box was vented to air. For example, the oxide shell was pinned on the glass surface during receding until most of the Galinstan[®] liquid has been pumped back into the syringe, as shown in Figure 2-2(b). Such pinning effect resulted in incorrect advancing and receding contact angles of 165° and 7°, in contrast to the accurate angles of 146.8° and 121.5°, respectively, in Table 2-3. The receding angle would have been even lower than 7°, if the measurement had not been ended prematurely by the liquid disconnection during the suction back.

Table 2-3 Contact angles of Galinstan[®] on different materials

Type	Material	Contact Angles			Surface Roughness			
		$\theta_A/^\circ$	$\theta_R/^\circ$	$(\theta_A-\theta_R)/^\circ$	R_q/nm	R_a/nm	R_{max}/nm	Surfaces Area Ratio
Conductor	Tungsten	161.3	119.6	41.7	3.31	2.54	27.27	0.13%
Insulator	Silicon nitride	147.0	126.1	20.9	1.38	1.09	13.43	0.37%
	Glass	146.8	121.5	25.3	2.05	1.38	30.2	0.30%
Polymer	Parylene	146.3	112.6	33.7	13.48	9.02	105.37	0.85%
	Teflon [®]	161.2	144.4	16.8	2.04	1.62	21.03	0.59%
Mica	Phlogopite	148.0	124.5	23.5	1.97	1.59	13.57	0.23%
	Muscovite	163.6	148.1	15.5	1.02	0.82	7.64	0.11%

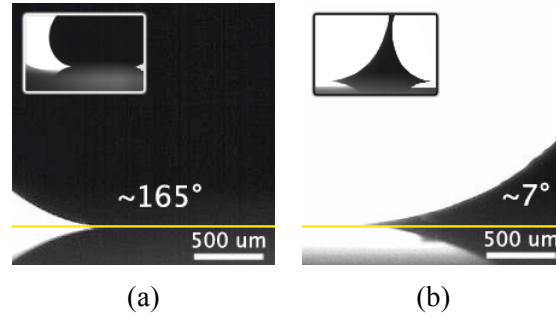


Figure 2-2 Three-phase contact regions of Galinstan[®] on a glass in ambient air (~20.9% oxygen). (a) advancing angle and (b) near receding angle. Pinning of the oxide skin makes the receding angle appear very low. Both (a) and (b) include an inset showing the larger field of view. The measurement of receding contact angle ended prematurely when the droplet was separated from the top needle.

The contact angle information of Galinstan[®] is rare at this point. Kocourek [16] reported that contact angle of Galinstan[®] on glass is 122° in air and 166° in 6% hydrochloric acid. Their result in air stays within the wide range we observed in air, i.e., 7° and 165°. However, a direct comparison is inadvisable, because Kocourek reported only one contact angle instead of advancing and receding angles, and did not provide additional information such as roughness of the glass surface and details of the measurement procedure.

2.3.2 Surface Tension of Galinstan[®] under Controlled Oxidation

Because oxidation affects the surface tension measurement, the reading would drift as a freshly formed pendant droplet gets oxidized over time. As shown in Figure 2-3, the main data (in O₂ < 0.5 ppm) stayed constant, confirming that the obtained value was free of any oxidation effect. To compare, we have run a pair of controlled experiments in slightly higher oxygen levels (in O₂ ~ 20 ppm and 500 ppm), which clearly reveal the oxidation effect on the surface tension measurement. The scatters in the data were caused mostly by

the shocks and vibrations from the environment not filtered out by the current vibration-isolation plate. Despite the excessive scatters in the data of 20 ppm oxygen during 10-15 minutes, the overall trend is still clear. We also found that if the pendent drop was exposed at higher oxygen levels (e.g., 2%), the long time dangling of such a pendent drop would actually stretch the oxidized skin and hold more liquid. The additional elastic force from the oxidized skin force the droplet profile to deviate from the ideal pendent drop profile, which is determined solely by surface tension and gravitational deformation. This viscoelastic properties of the oxidized Galinstan[®] skin has also been reported by Dickey et al. [17].

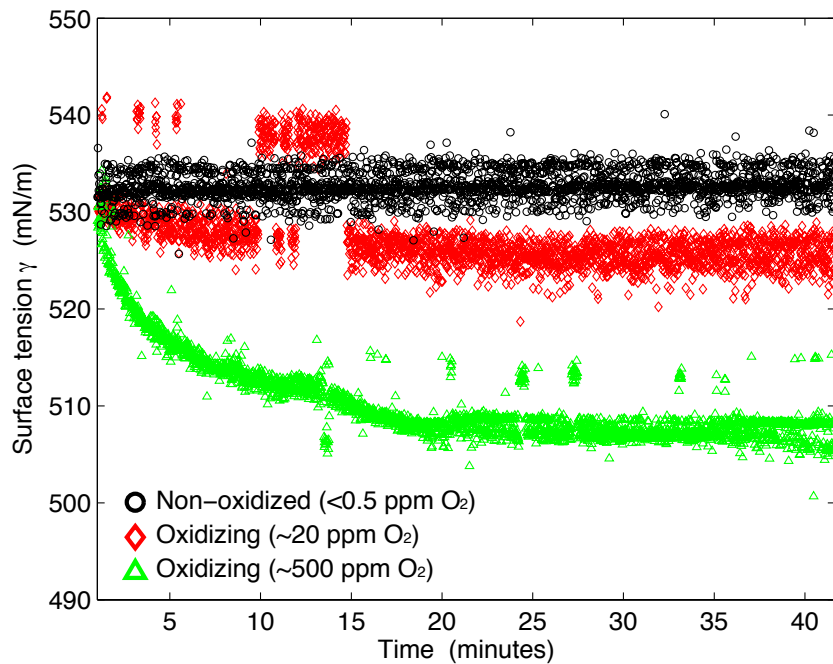


Figure 2-3 Surface tension of Galinstan[®] measured during the first 40 minutes of the quasi-static droplet growth. Canny edge detection algorithm was used for calculation of surface tension every second. The surface tension in this report (solid black circles for O₂ < 0.5 ppm) displays virtually constant values, showing no effect of oxidation. In contrast, the values in two slightly oxidizing conditions (red hollow diamonds for O₂ ~ 20 ppm; green hollow triangles for O₂ ~ 500 ppm) show the effect of oxidation before the measurements were completed.

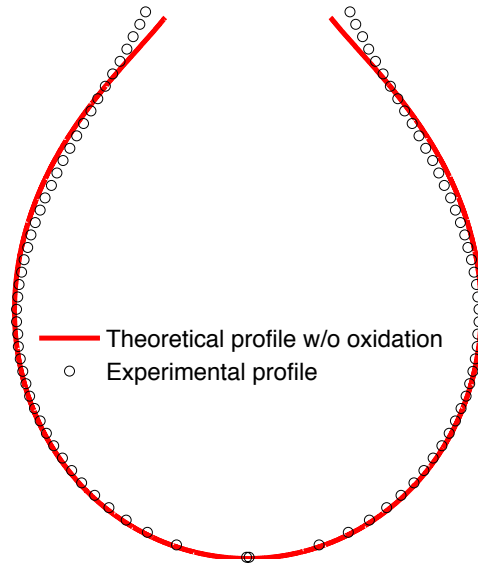


Figure 2-4 Deviation of the Galinstan[®] pendent drop profile from the Young-Laplace equation due to the elasticity of the oxidized skin. Selected pixels on an experimental profile are plotted in black circles while the red solid line draws the curved integral from the Young-Laplace equation. The snapshot was obtained from experiment with 500 ppm O₂ levels.

2.4 Summary

We have characterized the interfacial properties of Galinstan[®] that are important for the design of microdevices: contact angles and surface tension. Overcoming the strong oxidation of Galinstan[®] by performing the entire experiments inside a glove box of high-purity inert environment, the contact angles of Galinstan[®] have been measured by sessile droplets on several materials commonly used in MEMS devices, and the surface roughness of the materials was also reported. For example, the advancing and receding contact angles of Galinstan[®] on glass were measured to be 146.8° and 121.5°, respectively. In comparison, we have also tested the contact angles in ambient air and confirmed that the illusion of Galinstan[®] wetting solid surfaces, including glass, was caused by the oxide skin sticking on the surfaces. Compared with the true surface tension of Galinstan[®] free from oxidation, oxidized Galinstan[®] has shown reduced surface

tension with increasing oxygen levels. As a high-level hermetic packaging of MEMS devices becomes available to prevent oxidation, Galinstan[®] is expected to eventually substitute mercury for microscale applications. The work in this chapter has been published in [18] and has already stimulated a great increase of utilization of Galinstan[®] for various applications, as seen from citation [19]–[43].

2.5 References

- [1] Geratherm Medical AG, “Galinstan Safety Data Sheet,” 20-Jul-2011. [Online]. Available: <http://www.rgmd.com/msds/msds.pdf>.
- [2] Prosenjit Sen and Chang-Jin Kim, “Microscale Liquid-Metal Switches—A Review,” *IEEE Trans. Ind. Electron.*, vol. 56, pp. 1314–1330, 2009.
- [3] Alan S. Fitz Gerald, “Mercury relay,” 1773036, 12-Aug-1930.
- [4] A. H. Fleitman and J. R. Weeks, “Mercury as a nuclear coolant,” *Nucl. Eng. Des.*, vol. 16, pp. 266–278, 1971.
- [5] R. Clampitt and D. K. Jefferies, “Miniature ion sources for analytical instruments,” *Nucl. Instrum. Methods*, vol. 149, pp. 739–742, 1978.
- [6] A. Cao, P. Yuen, and L. Lin, “Microrelays With Bidirectional Electrothermal Electromagnetic Actuators and Liquid Metal Wetted Contacts,” *J. Microelectromechanical Syst.*, vol. 16, pp. 700–708, 2007.
- [7] K. A. Shaikh, Shifeng Li, and Chang Liu, “Development of a Latchable Microvalve Employing a Low-Melting-Temperature Metal Alloy,” *J. Microelectromechanical Syst.*, vol. 17, pp. 1195–1203, 2008.
- [8] P. Sen and C.-J. Kim, “A Fast Liquid-Metal Droplet Microswitch Using EWOD-Driven Contact-Line Sliding,” *J. Microelectromechanical Syst.*, vol. 18, pp. 174–185, 2009.
- [9] P. Sen and C.-J. Kim, “A Liquid–Solid Direct Contact Low-Loss RF Micro Switch,” *J. Microelectromechanical Syst.*, vol. 18, pp. 990–997, 2009.
- [10] Trung D. Truong, “Selective Deposition of Micro Scale Liquid Gallium Alloy Droplets,” M.S. thesis, University of California (UCLA), Los Angeles, 2000.

- [11] T. Liu, “Electromechanical Characterization of Liquid-Metal Galinstan Droplets,” Bachelor thesis, Zhejiang University, Hangzhou, 2009.
- [12] T. Liu, P. Sen, and C.-J. Kim, “Characterization of liquid-metal Galinstan for droplet applications,” in *Proc. IEEE Int. Conf. MEMS*, 2010, pp. 560–563.
- [13] Roger P. Woodward, “Contact Angle Measurements Using the Drop Shape Method,” 20-Jul-2011. .
- [14] Richard N. Lyon, *Liquid-Metal Handbook*, 2nd ed. Washington, D.C.: Atomic Energy Commission, Dept. of the Navy, 1952.
- [15] P. Sen, “Driving Liquid-Metal Droplets for RF Microswitches,” Ph.D. Dissertation, University of California (UCLA), Los Angeles, CA, 2007.
- [16] V. Kocourek, *Elektromagnetisches Abstützen von Flüssigmetall-Tropfen*. Ilmenau University of Technology Library, Germany, 2008.
- [17] M. D. Dickey, R. C. Chiechi, R. J. Larsen, E. A. Weiss, D. A. Weitz, and G. M. Whitesides, “Eutectic Gallium-Indium (EGaIn): A Liquid Metal Alloy for the Formation of Stable Structures in Microchannels at Room Temperature,” *Adv. Funct. Mater.*, vol. 18, no. 7, pp. 1097–1104, 2008.
- [18] T. Liu, P. Sen, and C.-J. Kim, “Characterization of nontoxic liquid-metal alloy galinstan for applications in microdevices,” *J. Microelectromechanical Syst.*, vol. 21, no. 2, pp. 443–450, 2012.
- [19] S.-Y. Tang, K. Khoshmanesh, V. Sivan, P. Petersen, A. P. O’Mullane, D. Abbott, A. Mitchell, and K. Kalantar-zadeh, “Liquid metal enabled pump,” *Proc. Natl. Acad. Sci.*, vol. 111, no. 9, pp. 3304–3309, 2014.
- [20] A. M. Morishita, C. K. Y. Kitamura, A. T. Ohta, and W. A. Shiroma, “Two-octave tunable liquid-metal monopole antenna,” *Electron. Lett.*, vol. 50, no. 1, pp. 19–20, 2014.
- [21] D. Kim, D. Jung, J. H. Yoo, Y. Lee, W. Choi, G. S. Lee, K. Yoo, and J.-B. Lee, “Stretchable and bendable carbon nanotube on PDMS super-lyophobic sheet for liquid metal manipulation,” *J. Micromechanics Microengineering*, vol. 24, no. 5, p. 055018, 2014.
- [22] A. Fassler and C. Majidi, “3D structures of liquid-phase GaIn alloy embedded in PDMS with freeze casting,” *Lab. Chip*, vol. 13, no. 22, pp. 4442–4450, 2013.
- [23] Y. Damgaci and B. A. Cetiner, “A frequency reconfigurable antenna based on digital microfluidics,” *Lab. Chip*, vol. 13, no. 15, pp. 2883–2887, 2013.
- [24] A. Morishita, C. Kitamura, A. Ohta, and W. Shiroma, “A Liquid-Metal Monopole Array With Tunable Frequency, Gain, and Beam Steering,” 2013.

- [25] J. Thelen, M. D. Dickey, and T. Ward, “A study of the production and reversible stability of EGaIn liquid metal microspheres using flow focusing,” *Lab. Chip*, vol. 12, no. 20, pp. 3961–3967, 2012.
- [26] D. Kim, D.-W. Lee, W. Choi, and J.-B. Lee, “A Super-Lyophobic 3-D PDMS Channel as a Novel Microfluidic Platform to Manipulate Oxidized Galinstan,” 2013.
- [27] R. Ma, C. Guo, Y. Zhou, and J. Liu, “Break-up phenomena of liquid metal thin film induced by high electric current,” *ArXiv Prepr. ArXiv13090601*, 2013.
- [28] J. Delacroix and L. Davoust, “Electrical activity of the Hartmann layers relative to surface viscous shearing in an annular magnetohydrodynamic flow,” *Phys. Fluids 1994-Present*, vol. 26, no. 3, p. 037102, 2014.
- [29] S.-Y. Tang, V. Sivan, K. Khoshmanesh, A. P. O’Mullane, X. Tang, B. Gol, N. Eshtiaghi, F. Lieder, P. Petersen, and A. Mitchell, “Electrochemically induced actuation of liquid metal marbles,” *Nanoscale*, vol. 5, no. 13, pp. 5949–5957, 2013.
- [30] D. K. Kim, M. Hwang, and J. P. Lagerwall, “Liquid crystal functionalization of electrospun polymer fibers,” *J. Polym. Sci. Part B Polym. Phys.*, vol. 51, no. 11, pp. 855–867, 2013.
- [31] V. Sivan, S.-Y. Tang, A. P. O’Mullane, P. Petersen, N. Eshtiaghi, K. Kalantar-zadeh, and A. Mitchell, “Liquid metal marbles,” *Adv. Funct. Mater.*, vol. 23, no. 2, pp. 144–152, 2013.
- [32] L. Wang and J. Liu, “Liquid metal material genome: Initiation of a new research track towards discovery of advanced energy materials,” *Front. Energy*, vol. 7, no. 3, pp. 317–332, 2013.
- [33] Q. Zhang and J. Liu, “Nano liquid metal as an emerging functional material in energy management, conversion and storage,” *Nano Energy*, vol. 2, no. 5, pp. 863–872, 2013.
- [34] M. Hodes, R. Zhang, L. S. Lam, R. Wilcoxon, and N. Lower, “On the Potential of Galinstan-Based Minichannel and Minigap Cooling,” 2013.
- [35] G. Li, M. Parmar, D. Kim, J.-B. J. Lee, and D.-W. Lee, “PDMS based coplanar microfluidic channels for the surface reduction of oxidized Galinstan,” *Lab. Chip*, vol. 14, no. 1, pp. 200–209, 2014.
- [36] C.-I. Chang, M.-H. Tsai, Y.-C. Liu, C.-M. Sun, and W. Fang, “Pick-and-place process for sensitivity improvement of the capacitive type CMOS MEMS 2-axis tilt sensor,” *J. Micromechanics Microengineering*, vol. 23, no. 9, p. 095029, 2013.
- [37] T. Lu, L. Finkenauer, J. Wissman, and C. Majidi, “Rapid Prototyping for Soft-Matter Electronics,” *Adv. Funct. Mater.*, 2014.

- [38] B. L. Cumby, G. J. Hayes, M. D. Dickey, R. S. Justice, C. E. Tabor, and J. C. Heikenfeld, "Reconfigurable liquid metal circuits by Laplace pressure shaping," *Appl. Phys. Lett.*, vol. 101, no. 17, p. 174102, 2012.
- [39] H. Li, S. Mei, L. Wang, Y. Gao, and J. Liu, "Splashing phenomena of room temperature liquid metal droplet striking on the pool of the same liquid under ambient air environment," *ArXiv Prepr. ArXiv13091075*, 2013.
- [40] X. Wu and D. Lee, "MEMS and Nanotechnology Laboratory, School of Mechanical Engineering, Chonnam National University, Gwangju, 500757, Republic of Korea," in *Nanotechnology (IEEE-NANO), 2013 13th IEEE Conference on*, 2013, pp. 1026–1029.
- [41] D. Kim, J. H. Yoo, Y. Lee, W. Choi, K. Yoo, and J.-B. J. Lee, "Gallium-based liquid metal inkjet printing," in *Micro Electro Mechanical Systems (MEMS), 2014 IEEE 27th International Conference on*, 2014, pp. 967–970.
- [42] V. Sivan, S. Tang, A. O'Mullane, P. Petersen, N. Eshtiaghi, K. Kalantar Zadeh, and A. Mitchell, "Enhanced electrochemical heavy metal ion sensor using liquid metal marbles-towards on-chip application," in *COMMAD 2012*, 2012, pp. 213–214.
- [43] W. G. Tonaki, W. Hu, A. T. Ohta, and W. A. Shiroma, "A reconfigurable, liquid-metal-based low-pass filter with reversible tuning," in *Wireless Symposium (IWS), 2013 IEEE International*, 2013, pp. 1–3.

Chapter 3 Generalized Cassie-Baxter Model

3.1 Introduction

Wetting and spreading is the central topic in many industrial processes, such as cleaning, drying, painting, coating, cooling, pesticide applications [1], [2], many of which are closely related to daily life as well. Although contact angles are commonly employed to evaluate the wetting property of a surface, it is the contact angle hysteresis, i.e., the difference between the contact angle at the advancing and receding meniscus, that is the main resistance of inhibiting droplet movement on a surface and thus of key importance for actual applications such as droplet-based microfluidics [3]. Contact angle hysteresis originates from the molecular interactions between the liquid and the solid due to many factors, such as roughness, chemical heterogeneity, solutes, etc. [1]. In searching for a “ideal” surface, it has been found that remarkably small contact angle hysteresis could be formed on a very rough (i.e., structured) hydrophobic surface [4]. The Cassie-Baxter (CB) model [5] has been used to describe the apparent contact angles of a liquid suspended on surface structures in terms of areal average of different interfacial components. The model was originally derived for apparent advancing contact angle, although the most common usage has been for apparent static contact angles assuming a thermodynamic equilibrium [6]. The paper further suggested the model to be used for receding contact angle as well [5], but much of the recent experimental data showed significant deviations [7]–[17]. Considering a droplet moving on posts, for example, the receding contact line effectively controls the droplet motion because the receding contact angles is much smaller than the advancing angle, which nears the maximum value (180°) for most cases anyway [7]–[18]. Since the receding angle varies significantly depending

on the surface structures, its knowledge is most crucial. Unfortunately, the CB equation fails to predict the receding contact angles on many of the today's superhydrophobic surfaces, prompting many to develop a modified CB model [7]–[11], [14], [16], [18].

The work presented in this Chapter has been developed based on Mr. Zhiyu Chen's M.S. thesis [19] and μ TAS paper [20]. In this Introduction session, we first review the existing models and their experimental methods to verify their model, and then point out an intrinsic shortcoming of those studies.

3.1.1 Cassie-Baxter (CB) Model for Contact Angles on Structured Surfaces

The contact angle for a droplet deposited on a rough/structured surface is generally described by the original CB model [5] in terms of areal average of contact angle on different interfacial components.

$$\cos\theta_i^* = f_s \cos\theta_i - f_g \quad (3.1)$$

where θ_i^* is the apparent contact angle, θ_i is the contact angle formed on the solid surface, f_s is the liquid-solid contact fraction, or solid fraction for short, i.e., the proportion of liquid-solid contact area (including the wetted regions inside the roughness) to the projected area of the entire composite interface, and f_g is the gas fraction similarly defined for liquid-vapor interface. This definition of f_s and f_g follows Cassie and Baxter's original paper [5], which included all the non-flat (e.g., rough, curved) effect on the liquid-solid and liquid-vapor interface and therefore $f_s + f_g \geq 1$. Such definition automatically including the Wenzel model [21] as a special case of Eq. 3.1 where $f_g = 0$ [5]. We note that θ in Eq. 3.1 can be the Young's angle θ_Y (i.e., intrinsic contact angle) or the advancing or receding contact angle θ_A or θ_R to predict the apparent contact angle in

the static, or advancing, or receding case, respectively. Although Eq. 3.1 was nowadays widely used to predict static contact angles using θ_V assuming a thermodynamic equilibrium [6], we point out that it was originally derived for an advancing meniscus using θ_A , and generalized for a receding meniscus by Cassie and Baxter [5], with no reason however, using θ_R while f_s and f_g are obtained from the advancing case [5].

3.1.2 Existing Modified CB Models for Dynamic Contact Angles

In order to accommodate the contact-angle hysteresis in the CB theory, recent studies have shown the contact angle behavior is mostly determined by the liquid interaction close to the three-phase contact line (abbr. as “contact line” from now on) [7]–[10], [18], [22]–[24]. Based on this phenomenon, two main approaches have been developed: One approach replaced the areal average of contact angles with a linear average of contact angles solely along the three-phase contact line, considering the dominance of differential behavior on the contact line [8], [9], [18]. The other approach calculated hysteresis from the local deformed meniscus shape, which creates a surface energy barrier against contact line motion [10], [11]. We summarize those models in Table 3-1 with their related reference.

Table 3-1 Summary of existing models elaborated to predict dynamic contact angles

Approach	Equation	Eq. #	Notes	Ref.
Linear average of contact angle along the perimeter of the drop	$\theta_A^* = \lambda_p (\theta_A + \omega) + (1 - \lambda_p) \theta_{\text{air}}$ $\theta_R^* = \lambda_p \theta_R + (1 - \lambda_p) \theta_{\text{air}}$	(3.2) (3.3)	$\theta_{\text{air}} = 180^\circ$; λ_p is the linear fraction of the contact line on asperities; ω is the rise angle of the asperity side; ideal Cassie case ($f_s + f_g = 1$)	[7]
Linear average of cosine of contact angle along the perimeter of the drop	$\cos \theta_i^* = r_\phi \phi_{d,i} \cos \theta_Y + (1 - \phi_{d,i}) \cos \theta_2$	(3.4)	θ_Y is the Young's angle on solid; $\phi_{d,i}$ is the differential area fraction solid-liquid and liquid-air interfaces at the contact line; r_ϕ is the roughness wetted surface; $\theta_2 = 180^\circ$ (stripes, posts) or 0° (holes)	[8], [18]
Linear average of cosine of advancing or receding contact angle along the perimeter of the drop	$\cos \theta_A^* = f_{\text{max}} \cos \theta_A - (1 - f_{\text{max}})$ $\cos \theta_R^* = f_{\text{max}} \cos \theta_R - (1 - f_{\text{max}})$	(3.5) (3.6)	$f_{\text{max}} = 0$ for advancing on posts and $f_{\text{max}} = D/P$ for receding on post where D is the diameter and P is the pitch; $f_{\text{max}} = D/P$ for advancing on holes and $f_{\text{max}} = 1$ for receding on holes; Equations derived for heterogeneous surface and simplified for structured hydrophobic surface here	[9]
Lateral deformation of the receding meniscus	$\cos \theta_R^* - \cos \theta_A^* = \frac{a}{4} f_s \ln \left(\frac{\pi}{f_s} \right)$	(3.7)	$a = 3.8$ from data fitting yet a is expected to be 2; f_s is the solid fraction; $\theta_A^* = 180^\circ$	[10]
Upward deformation of the receding meniscus	$\cos \theta_R^* - \cos \theta_A^* = \frac{A(\theta_R)}{P^2}$	(3.8)	P is the pitch; $A(\theta_R)$ is the deformed surface area approx. by integration of catenoid; $\theta_A^* = 180^\circ$	[11]
Remaining liquid layer on the receded structures	$\cos \theta_R^* = 2f_s - 1$	(3.9)	A special case of Eq. 3.1 where $\theta_R = 0^\circ$ and for ideal Cassie case ($f_s + f_g = 1$)	[25]

3.1.3 Existing Experimental Method to Measure Dynamic Contact Angles

Contact angles are commonly measured by methods using sessile drop/bubble, vertical rod, tensiometer, horizontal liquid surface, and capillaries [26], among which the most convenient way is the sessile drop/bubble method where the contact angle is optically analyzed from a side view of a sessile drop or bubble placed on a solid surface. In order

to measure dynamic contact angles on structured surfaces using sessile drops, the droplet should form advancing or receding meniscus by expanding/contracting or sliding on the test surface, as shown in Figure 3-1. Contact angles measured by these methods assume that the droplet is axisymmetric (which is obvious not the case such as Figure 3-1b), i.e., apparent contact angles are independent on viewing angles. However, due to the highly tortuous contact line formed on a structured surface, apparent contact angles are usually different when measured from different angles, i.e., three dimensional (3-D) contact angles are projected on a two dimensional (2-D) view plane, leading to the major problem in using those experimental observations to verify any models proposed above. Additionally, there is no direct parameter in determining the “apparentness” of the contact angles measured, which is affected by the relative size of the surface structures and tools used for measurement (such as needle/pipette to hold the droplet).

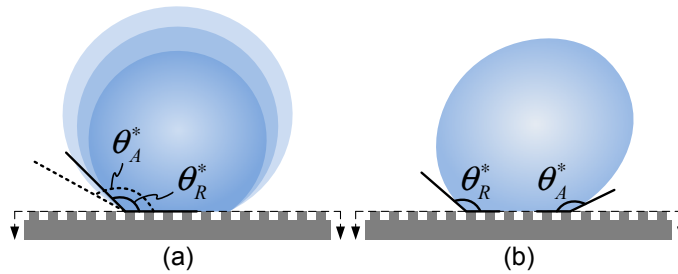


Figure 3-1 Cassie-state droplets advancing and receding on non-wetting structured surfaces. (a) and (b) show the side view of meniscus advancing and receding by (a) adding/subtracting liquid to/from a droplet and (b) sliding droplet on the surface. θ_A^* and θ_R^* represent the apparent advancing and receding contact angle, respectively.

3.1.4 Limitations of Existing Experimental Studies on Contact Angle Hysteresis

Although these approaches explained their own data and some other data in the literature, they lacked a *direct* comparison between theory and experiments. One common

shortcoming has been that the proposed theory was derived for a two-dimensional (2-D) configuration as was the original CB model, but the experimental data, typically the apparent contact angles, were obtained in a three-dimensional (3-D) condition [8]–[11], [18]. For the rare case of a 3-D model based on finite element method, fitting the simulated and experimental data would leave some discrepancies that could not be physically explained [23]. We first note that no matter how the advancing and receding contact angles were measured, either by adding/subtracting liquids (Figure 3-1a) or sliding droplets on the surface (Figure 3-1b), there exists an intrinsic mismatch between the apparent contact line of the usual droplets that are circular and the typical surface patterns that are linear, as shown in (Figure 3-2a, b, d, e), causing the measured apparent contact angles to be affected by all other neighboring contact angles along the contact line that are under different moving conditions. Such mismatch could be resolved only when the contact line and the underlying pattern can align. One example is a spherical droplet on a circular surface pattern, as shown Figure 3-2(c). Another example is a rectangular droplet on a linear surface pattern, as shown in Figure 3-2(f).

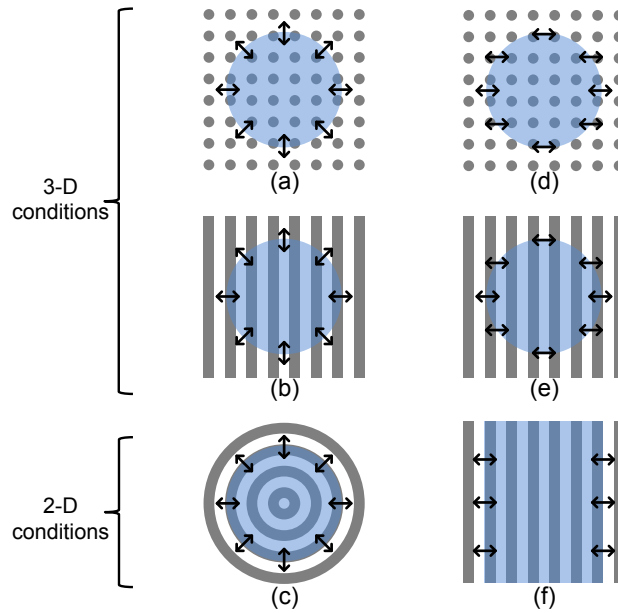


Figure 3-2 Top view of contact line motions. (a–c) show the contact line motions of a spherical droplet advances or recedes by liquid addition or subtraction. (d–f) show the contact line motions of droplet sliding on a structured surface. (a), (b), (d), and (e) show the top view of contact line motions commonly employed to study dynamic contact angles in literature. While the surface structures are in a linear pattern, the contact line sliding on them is circular, creating 3-D conditions. (c) and (f) show the top view of contact line motions allowing dynamic contact angles in 2-D conditions. (c) is a scenario of a spherical droplet expanding or contracting on a concentric ring pattern. (f) is a scenario of a cylindrical droplet traversing across parallel stripes, adopted for the current study.

3.1.5 Summary of Our Approach

We first pinpoint why the original CB equation failed to predict the apparent contact angles at a receding meniscus and derive a new model to correct the fault. We then develop a new experiment that resembles Figure 3-2(f) following [20] and use the resulting 2-D data to confirm the new model. The 2-D data also reveal the flaws in the existing models in the literature. Encouraged by the success, we then generalize our model from 2-D to 3-D and find it agrees well with other published data in the literature, validating the generalized CB model.

3.2 Theory

An “apparent” receding contact angle is an angle seen far enough from the microstructured surface so as not to be affected by the local contact angles and their variations right on the surface. When the receding meniscus slides across structures so that the local contact line has to jump between them, the apparent receding contact angle represents a time-averaged angle.

3.2.1 Why the Original CB model Fails to Predict Dynamic Contact Angles

We present the derivation of CB model and our modified model for ideal 2-D surface based on force balancing at the contact line. As shown in Figure 3-3(a), the angle of contact at equilibrium on an ideal surface (smooth, homogeneous, and rigid) can be given by the Young’s equation [27]:

$$\gamma_{SV} = \gamma_{SL} + \gamma \cos \theta_Y \quad (3.10)$$

where γ_{SV} and γ_{SL} are the surface tension at the solid-vapor and solid-liquid interface, θ_Y is the intrinsic contact angle (i.e., Young’s angle). In reality, the angle at the advancing meniscus is greater and the angle at the receding meniscus is smaller than the Young’s angle. We quantify such difference, following the early works [28]–[30], by introducing a friction force (τ) acting on the contact line which shows excellent agreement with experimental data [29], [30]. For example, on a receding meniscus depicted in Figure 3-3(b), we have the force balance as,

$$\gamma_{SV} + \tau_R = \gamma_{SL} + \gamma \cos \theta_R \quad (3.11)$$

where θ_R is the receding contact angle and τ_R is the receding line friction which can be calculated from Eq. 3.10 and 3.11:

$$\frac{\tau_R}{\gamma} = \cos\theta_R - \cos\theta_Y \quad (3.12)$$

Now if we examine a meniscus receding on an infinitely long periodic gratings (i.e., true 2-D) with solid fraction f_s and gas fraction f_g , i.e., $f_s = (\text{solid-liquid interface})/(\text{pitch})$ and $f_g = (\text{liquid-air interface})/(\text{pitch})$. During receding, as shown in Figure 3-3 (c) and Figure 3-3 (d), the meniscus can be on air and on solid and experience sliding friction as zero and τ_R , respectively. If the sliding on air and on solid were of same speed, then the apparent receding contact angle θ_R^* can be written as the average of the two angles as

$$\phi_s \gamma_{SV} + \phi_g \cdot 0 + \phi_s f_R = \phi_s \gamma_{SL} + \phi_g \gamma + \gamma \cos\theta_R^* \quad (3.13)$$

which, when combined with Eq. 3.11, reduces to the original CB model for a receding meniscus: $\cos\theta_R^* = f_s \cdot \cos\theta_R - f_g$. However, in reality the contact line recedes much faster on air than on solid, which the original CB model cannot address.

3.2.2 Modified Cassie-Baxter Model for 2-D Contact Line Sliding

Since the friction of sliding on air is practically zero, the time of sliding on air is negligible compared with that on solid, rewriting Eq. 3.13 as:

$$f_s \gamma_{SV} + \tau_R = f_s \gamma_{SL} + f_g \gamma + \gamma \cos\theta_R^* \quad (3.14)$$

Utilizing the CB model for the apparent static contact angle θ^* [6],

$$\cos\theta^* = f_s \cos\theta_Y - f_g \quad (3.1)$$

we combine Eq. 3.1 with Eq. 3.10–3.12 and Eq. 3.14 and eliminate γ_{SV} , γ_{SL} , and τ_R , yielding the modified Cassie-Baxter equation for 2-D receding meniscus:

$$\cos\theta_R^* = \cos\theta^* + (\cos\theta_R - \cos\theta_Y) \quad (3.15)$$

Equation 3.15 provides the physical interpretation of the apparent receding contact angle: the static contact angle calculated from the CB equation (Eq. 3.1) plus the resistance from the contact line receding on the solid surface (Eq. 3.12) and on air (which is zero).

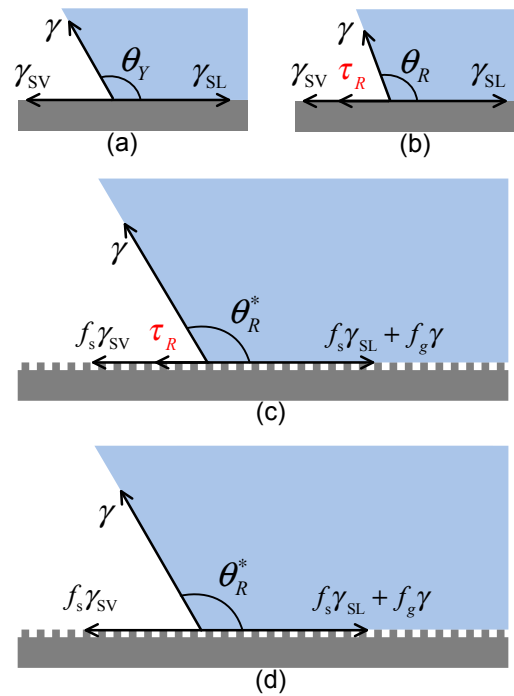


Figure 3-3 Force balances at contact lines on smooth and structured surfaces. (a) Young's relation describes the balance in equilibrium for an ideal surface without hysteresis. (b) Forces balance at the receding contact line on a smooth surface by introducing line friction τ_R to represent the contact angle hysteresis (c, d) Forces balance at the receding contact line on a structured surface of infinitely long ridges. (c) When receding on air, the contact line does not experience any friction. (d) When receding on solid, the contact line experience the same friction τ_R as on the smooth surface.

So far, we have only considered the apparent receding contact angle. For 2-D advancing, Eq. 3.15 can be used by replacing the receding contact angle θ_R with an advancing contact angle θ_A . However, the advancing contact angle should use the advancing contact angle on air ($\theta_A = 180^\circ$) since, assuming the liquid moves from left to right, the advancing meniscus is pinned at right edge of the microstructures and can advance only

when the local contact angle reaches the advancing contact angle of air. In contrast, the receding meniscus is pinned at the left edge of the microstructure until it slides on the solid surface. By plugging in $\theta_A = 180^\circ$, the apparent advancing contact angle is calculated to be 180° regardless of the solid fraction.

3.2.3 Generalization to 3-D by Introducing Line Solid Fraction

The next question naturally is whether Eq. 3.15, which was derived by considering a 2-D condition, can be generalized for 3-D conditions. To do so, we examine the two terms that contributed to the apparent receding contact angle in Eq. 3.15. The first term, which is the static contact angle term calculated from the Cassie-Baxter equation, considers only the solid fraction and is therefore unchanged for 3-D conditions. However, the second term, which includes the line friction τ_R , should be fractionalized for 3-D contact lines so that only the three-phase part experiences a resistance from receding on a solid structure while the liquid-vapor part (suspended meniscus) experiences no resistance while receding on air. Because τ_R exerts solely on the contact line in the direction opposite to the movement, the net resistance should be calculated as the sum (i.e., line integral) along the entire contact line. Therefore, we modify Eq. 3.15 to accommodate receding contact lines in 3-D conditions:

$$\cos\theta_R^* = \cos\theta^* + (\cos\theta_R - \cos\theta_Y)\lambda_s \quad (3.16)$$

where λ_s is defined as the solid line fraction, i.e., the length ratio of three-phase contact line to the projected contact line for a receding meniscus. As shown in Figure 3-4, we define the line solid fraction λ_s to be the ratio of real solid-liquid-air (three-phase) contact line \widehat{l}_s to the apparent (projected) line l , as follows:

$$\lambda_s = \frac{\widehat{l}_s}{l} \quad (3.17)$$

As schematically presented in Figure 3-4, the apparent/projected/macrosopic contact line of a sessile drop is a circle on a microstructured surface, while the real/microscopic contact line is intermittent and contorted. This line solid fraction is analogous to the solid areal fraction f_s of Cassie's definition in [5].

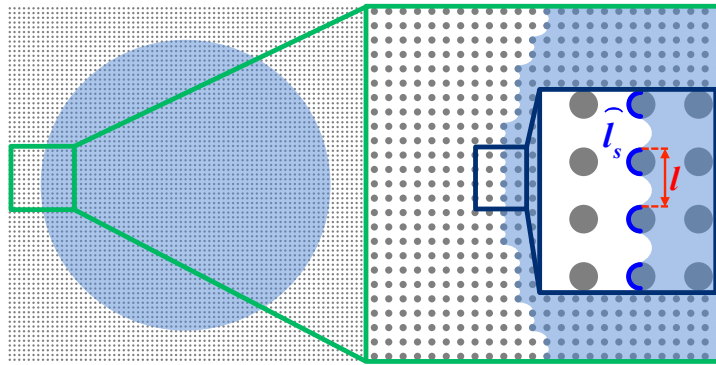


Figure 3-4 Definition of line solid fraction from microscopic droplet boundary

Since in our experiment the apparent contact angled remained unchanged during the microscopic contact line sliding and jumping, we consider λ_s is mostly determined when contact line is pinned and ignore the effect from the short period of sliding and jumping. Particularly, Eq. 3.16 reduces to Eq. 3.15, if the surface structures are micro-gratings (i.e., stripes), i.e., $\lambda_s = 1$. Although λ_s in Eq. 3.16 may appear similar to some other parameters proposed in literature [7], [15], [31], we further point out that λ_s depends not only on geometries and solid fraction but also on the conditions of receding and, therefore, needs to be determined case by case. For example, on sparse posts, $\lambda_s = (\text{post perimeter})/(\text{pitch})$ for slow receding (e.g., evaporation of water in [31]), but on dense posts, λ_s may be smaller due to fast sliding or may be larger due to secondary pinning [32]. We also note

that for microstructure of an asymmetric geometry (e.g. triangular posts) λ_s may depend on the direction of receding.

3.3 Experiments

To verify our modified CB model (Eq. 3.15) for 2-D contact line motion, we followed Figure 3-2(f) and Chen's earlier work [19], [20], which created a near 2-D motion by traversing an elongated droplet on superhydrophobic micro-gratings. An elongated droplet is against the natural tendency of a liquid forming a sphere to minimize its surface, but we can shape a liquid by a wetting pattern on a confining solid [33], [34]. As shown in Figure 3-5, we coated and patterned a photoresist layer on glass to open a hydrophilic rectangle on which a droplet was confined. After careful alignment, the elongated droplet was put into contact with the superhydrophobic grating surface underneath. Held by the hydrophilic window on the top plate, the droplet formed advancing and receding meniscus on the superhydrophobic substrate to be sliding parallel to the top plate. Since the contact line traversing across the structures was closest to a 2-D condition at the middle of the long droplet, we focused a high-speed camera at the middle to capture the details of this dynamic event.

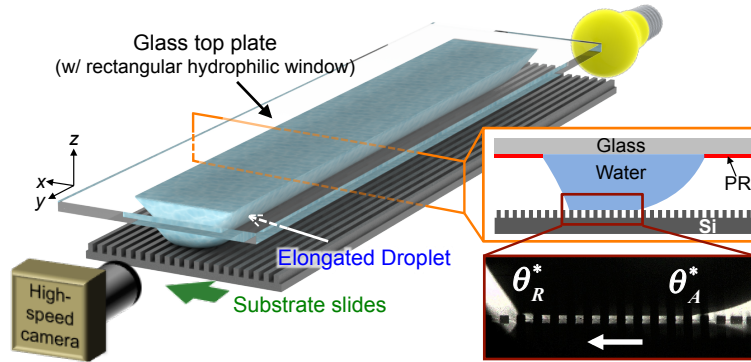


Figure 3-5 Apparatus to create and measure 2-D contact line motion. An elongated droplet was created by sandwiching a water droplet between a patterned glass top plate and the structured superhydrophobic surface. The cross-sectional views show the device configuration with a zoomed-in image captured in our experiment.

3.4 Results and Discussion

3.4.1 Verification of Generalized 2-D CB Model

We tested grating structures of a fixed pitch of $200\ \mu\text{m}$ with solid fraction f_s from 0.2 to 0.8. Figure 3-6 collected the time-lapsed images of menisci receding and advancing on surface structures with $f_s = 0.5$. Overall, the receding contact line jumped and advancing contact line rolled onto the next structure. Similar contact line motions have also been reported by other researchers [12]–[15]. However, taking advantage of the high-speed imaging and 2-D condition, we were able to capture far more details. As shown in Figure 3-7, there were two different contact angles depending on the measurement scale: the local or microscopic receding contact angle measured at the same length scale as the pitch of the gratings and the apparent or macroscopic receding contact angle measured at a much larger length scale. The local receding contact angle was found to be invariant for all tested surfaces and coincided with the receding contact angle on a smooth Teflon[®] surface (i.e., $\theta_R = 110^\circ$), but the apparent receding contact angles increased with decreasing solid fraction f_s (Figure 3-8). On the other hand, the apparent angle did not

change during the short period of microscopic contact line jumping and the local contact angle varying significantly (from $\sim 110^\circ$ at 107.17 ms to $\sim 147^\circ$ at 108.50 ms, as shown in Figure 3-6(a)). We note that these observations were all included in our model, as elaborated below. The line friction force on the solid is irrelevant to the solid fraction. The apparent contact angles are only affected by the solid fraction but unaffected by the local contact angle changes during sliding and jumping. We also point out that the apparent contact angles shown between 0-80 ms are intermediate angles not regarded as receding angles since the meniscus is pinned on the top plate and prevented the recovery of the apparent receding contact angle. This intermediate phase would not exist in an ideal 2-D model, i.e., the top plate at an infinite distance. Figure 3-8 compares our data with Eq. 3.15 and other models in literature [5], [7], [8], [10], [25]. Only Eq. 3.15 accurately predicts the apparent receding contact angles measured under a 2-D condition. Although the measurement of apparent advancing contact angle is difficult with our experimental setup because of the finite distance between the top plate and bottom substrate as shown in Figure 3-6, plenty of papers confirmed $\theta_A^* = 180^\circ$ in the literature [8], [11], [13]–[16].

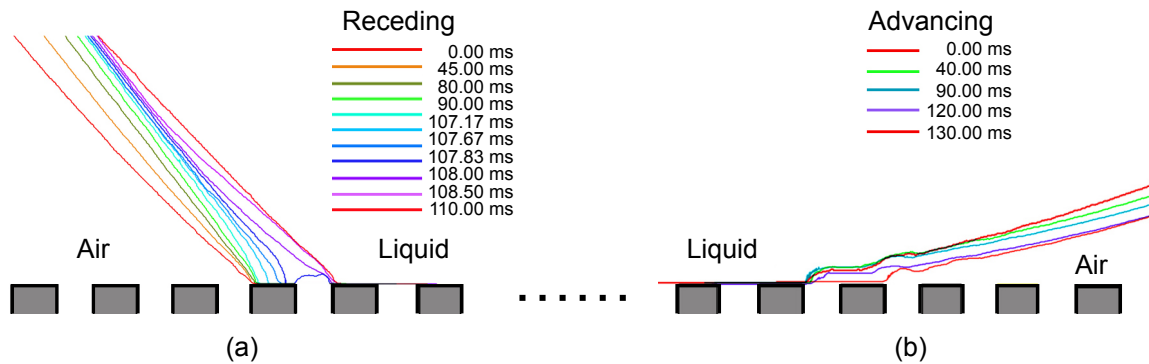


Figure 3-6 Snapshots of menisci above (a) receding and (b) advancing contact line, overlapping in time sequence on a micro-grating surface with solid fraction $f_s = 0.5$ and pitch $P = 200 \mu\text{m}$. The meniscus lines were obtained from the high-speed images by edge detection using MATLAB software.

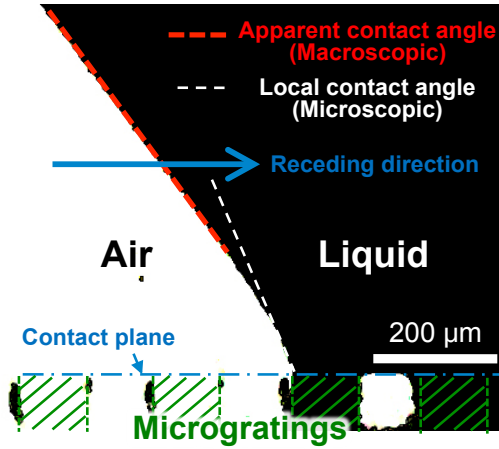


Figure 3-7 Apparent and local contact angles measured from a high-speed image of water receding on a structured surface with $f_s = 0.5$. The image has been converted into black and white for better contrast. Microstructures not in contact with the droplet are less visible due to the strong lighting from behind.

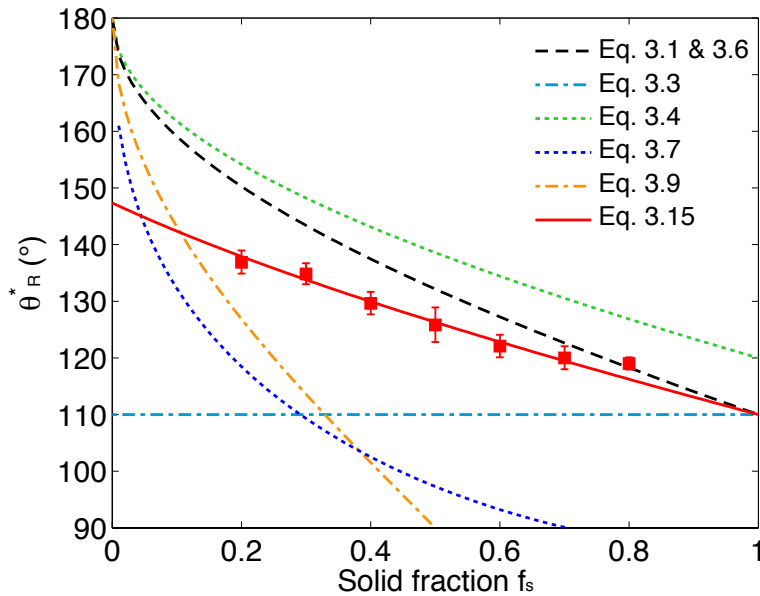


Figure 3-8 Apparent receding contact angles measured on surfaces with different f_s are compared with various models. Our model (Eq. 3.15) was the only one that fit the 2-D experimental data. For all the models, $\theta_Y = 120^\circ$ and $\theta_R = 110^\circ$ (measured from a Teflon[®] coated on silicon surface) were used to calculate theoretical θ_R^* .

3.4.2 Verification of Generalized 3-D CB Model

Following our definition of the line solid fraction λ_s , we examined Eq. 3.16 with λ_s determined for each case and found it matched well not only with our 2-D data but also with the 3-D data reported in literature [11], [16], [17], [23], [31], as illustrated in Figure 3-9. The receding conditions and related λ_s are summarized in Table 3-2. The line solid fraction is approximately determined in one unit of the microstructures. When the droplet recedes by subtraction, the three-phase contact line is given by the perimeter of the microstructures (column 2-4). In comparison, when the droplet recedes by sliding, the maximum solid contact attained in the sliding direction gives the three-phase contact line. The apparent contact line is usually the pitch of the microstructures unless it is asymmetry and the receding is determined by kink as explained in [23]. One group of the data (blue rightwards triangles) from Priest et al. [16] were measured on holes structures and appeared more scattered than other data which were measured on post structures. We note that although Eq. 3.16 gives good agreement with data in the literature, it should not be forgotten that Eq. 3.16 considers only the case where the liquid can slide on the solid surface without trace. In other words, it does not include the cases where the meniscus ruptures as it detaches from microstructures and leaves droplets behind [8], [35], [36].

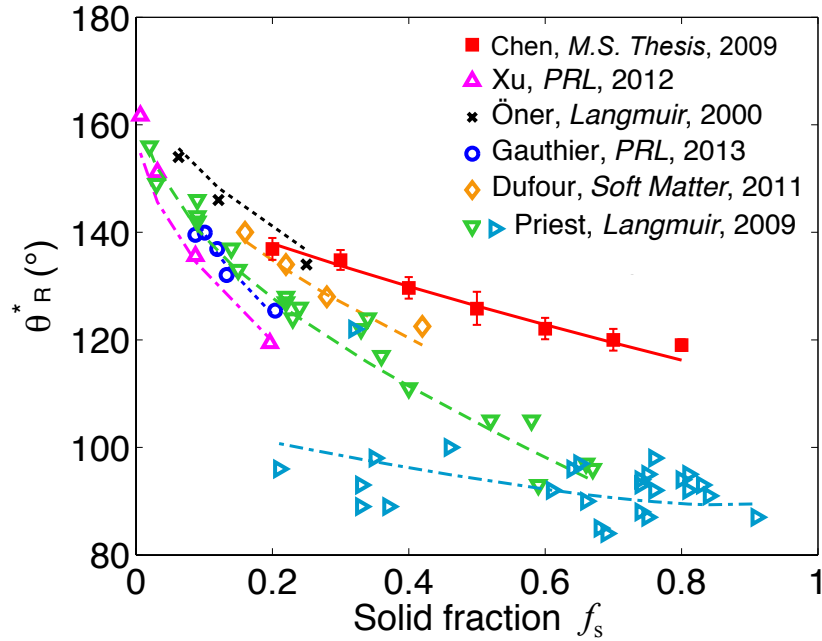
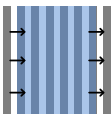
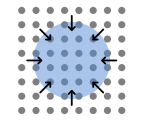
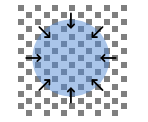
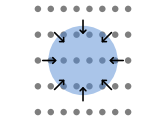
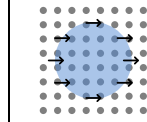
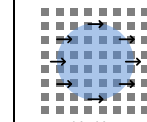
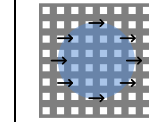
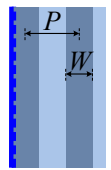
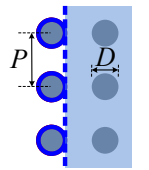
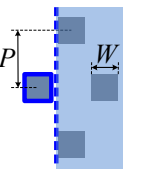
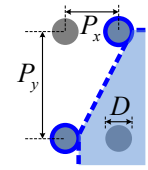
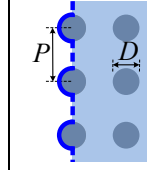
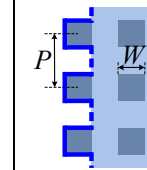
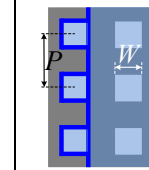


Figure 3-9 Comparing apparent receding contact angles of water reported in literature (symbols) and the modified Cassie-Baxter equation (Eq. 3.16) generalized by us (lines). The solid symbols and line represent our data measured on 2-D condition. λ_s and receding conditions are summarized in Table 3-2.

Table 3-2 Line solid fraction λ_s used in Figure 3-9 for different surface structures and receding conditions

	This work	Xu, [31]	Öner, [17]	Gauthier, [23]	Dufour, [11]	Priest, [16]	
Receding conditions	 Sliding	 Subtraction	 Subtraction	 Subtraction	 Sliding	 Sliding	 Sliding
Contact line top view							
λ_s	1	$\pi D/P$	$4W/P$	$\pi D/(P_x^2 + P_y^2)^{0.5}$	$1/2 \cdot \pi D/P$	$3W/P$	$3W/P + 1$

3.5 Future Works

A generalization of Eq. 3.16 to smooth heterogeneous surface can be performed in the same way, which results in an Eq. 3.18 as follows.

$$\cos\theta_R^* = \cos\theta^* + \sum_i \lambda_i (\cos\theta_{R_i} - \cos\theta_{Y_i}) \quad (3.18)$$

$$\cos\theta_A^* = \cos\theta^* + \sum_i \lambda_i (\cos\theta_{Y_i} - \cos\theta_{A_0}), \theta_{A_0} \geq \theta_{A_i} \quad (3.19)$$

Limited by the data availability in literature, examination of Eq. 3.18 and 3.19 are quite limited and need to be collected in the future. Further more, the cases where a receding meniscus ruptures may be modeled so that a universal equation can be consequently derived.

3.6 Conclusions

In conclusion, we have generalized CB equation to describe advancing and receding contact angles of a liquid suspended on hydrophobic microstructures. Our model consists of simple force balance at the three-phase contact line by including a line friction force to describe the contact angle hysteresis. To avoid the typical but incorrect practice of verifying 2-D models through 3-D measurement of contact angles, we have created a near 2-D condition by sliding an elongated droplet on micro-gratings. The 2-D experiments supported the proposed model, while revealing all the existing models in literature were not general. By introducing a line solid fraction λ_s in analogy to Cassie's areal fraction, a generalized Cassie-Baxter equation has been proposed and showed good agreement with the data in literature.

3.7 References

- [1] P. G. de Gennes, “Wetting: statics and dynamics,” *Rev. Mod. Phys.*, vol. 57, no. 3, pp. 827–863, Jul. 1985.
- [2] D. Bonn, J. Eggers, J. Indekeu, J. Meunier, and E. Rolley, “Wetting and spreading,” *Rev. Mod. Phys.*, vol. 81, no. 2, pp. 739–805, May 2009.
- [3] W. C. Nelson and C.-J. Kim, “Droplet Actuation by Electrowetting-on-Dielectric (EWOD): A Review,” *J. Adhes. Sci. Technol.*, vol. 26, no. 12–17, pp. 1747–1771, 2012.
- [4] Robert H. Dettre and Rulon E. Johnson, “Contact Angle Hysteresis,” in *Contact Angle, Wettability, and Adhesion*, vol. 43, American Chemical Society, 1964, pp. 136–144.
- [5] A. Cassie and S. Baxter, “Wettability of porous surfaces,” *Trans. Faraday Soc.*, vol. 40, pp. 546–551, 1944.
- [6] R. E. Johnson and R. H. Dettre, “Contact Angle Hysteresis,” in *Contact Angle, Wettability, and Adhesion*, vol. 43, 0 vols., AMERICAN CHEMICAL SOCIETY, 1964, pp. 112–135.
- [7] C. W. Extrand, “Model for contact angles and hysteresis on rough and ultraphobic surfaces,” *Langmuir*, vol. 18, no. 21, pp. 7991–7999, 2002.
- [8] W. Choi, A. Tuteja, J. M. Mabry, R. E. Cohen, and G. H. McKinley, “A modified Cassie-Baxter relationship to explain contact angle hysteresis and anisotropy on non-wetting textured surfaces,” *J. Colloid Interface Sci.*, vol. 339, no. 1, pp. 208–216, 2009.
- [9] R. Raj, R. Enright, Y. Zhu, S. Adera, and E. N. Wang, “Unified Model for Contact Angle Hysteresis on Heterogeneous and Superhydrophobic Surfaces,” *Langmuir*, vol. 28, no. 45, pp. 15777–15788, 2012.
- [10] M. Reyssat and D. Quéré, “Contact Angle Hysteresis Generated by Strong Dilute Defects,” *J. Phys. Chem. B*, vol. 113, no. 12, pp. 3906–3909, 2009.
- [11] R. Dufour, M. Harnois, V. Thomy, R. Boukherroub, and V. Senez, “Contact angle hysteresis origins: investigation on super-omniphobic surfaces,” *Soft Matter*, vol. 7, no. 19, pp. 9380–9387, 2011.
- [12] R. Dufour, M. Harnois, Y. Coffinier, V. Thomy, R. Boukherroub, and V. Senez, “Engineering sticky superomniphobic surfaces on transparent and flexible PDMS substrate,” *Langmuir*, vol. 26, no. 22, pp. 17242–17247, 2010.
- [13] C. Dorrer and J. Rühe, “Advancing and receding motion of droplets on ultrahydrophobic post surfaces,” *Langmuir*, vol. 22, no. 18, pp. 7652–7657, 2006.

- [14] A. Shastry, S. Abbasi, A. Epilepsia, and K.-F. Bohringer, "Contact Angle Hysteresis Characterization of Textured Super-Hydrophobic Surfaces," in *Solid-State Sensors, Actuators and Microsystems Conference, 2007. TRANSDUCERS 2007. International*, 2007, pp. 599–602.
- [15] A. T. Paxson and K. K. Varanasi, "Self-similarity of contact line depinning from textured surfaces," *Nat. Commun.*, vol. 4, p. 1492, 2013.
- [16] C. Priest, T. W. Albrecht, R. Sedev, and J. Ralston, "Asymmetric wetting hysteresis on hydrophobic microstructured surfaces," *Langmuir*, vol. 25, no. 10, pp. 5655–5660, 2009.
- [17] D. Öner and T. J. McCarthy, "Ultrahydrophobic surfaces. Effects of topography length scales on wettability," *Langmuir*, vol. 16, no. 20, pp. 7777–7782, 2000.
- [18] S. T. Larsen and R. Taboryski, "A Cassie-like law using triple phase boundary line fractions for faceted droplets on chemically heterogeneous surfaces," *Langmuir*, vol. 25, no. 3, pp. 1282–1284, 2009.
- [19] Z. Chen, "Dynamic contact line motion on micro-structured surfaces," M.S. thesis, University of California, Los Angeles, 2009.
- [20] Z. Chen and C.-J. Kim, "Two-Dimensional Sliding of Liquid Contact Line Across Hydrophobic Microstructures," in *Proc. Int. Conf. Miniaturized Systems for Chemistry and Life Sciences (μ TAS)*, Jeju, Korea, 2009, pp. 1362–1364.
- [21] R. N. Wenzel, "Resistance of solid surfaces to wetting by water," *Ind. Eng. Chem.*, vol. 28, no. 8, pp. 988–994, 1936.
- [22] J. F. Joanny and P.-G. de Gennes, "A model for contact angle hysteresis," *J. Chem. Phys.*, vol. 81, no. 1, pp. 552–562, 1984.
- [23] A. Gauthier, M. Rivetti, J. Teisseire, and E. Barthel, "Role of kinks in the dynamics of contact lines receding on superhydrophobic surfaces," *Phys. Rev. Lett.*, vol. 110, no. 4, p. 046101, 2013.
- [24] L. Gao and T. J. McCarthy, "Wetting 101° ," *Langmuir*, vol. 25, no. 24, pp. 14105–14115, Dec. 2009.
- [25] N. A. Patankar, "On the modeling of hydrophobic contact angles on rough surfaces," *Langmuir*, vol. 19, no. 4, pp. 1249–1253, 2003.
- [26] R. E. Johnson and R. H. Dettre, "Wettability and contact angles," *Surf. Colloid Sci.*, vol. 2, pp. 85–153, 1969.
- [27] T. Young, "An Essay on the Cohesion of Fluids," *Philos. Trans. R. Soc. Lond.*, vol. 95, pp. 65–87, Jan. 1805.

- [28] N. K. Adam and G. Jessop, “Angles of contact and polarity of solid surfaces,” *J. Chem. Soc. Trans.*, vol. 127, pp. 1863–1868, 1925.
- [29] X. D. Wang, X. F. Peng, J. F. Lu, T. Liu, and B. X. Wang, “Contact angle hysteresis on rough solid surfaces,” *Heat Transfer—Asian Res.*, vol. 33, no. 4, pp. 201–210, 2004.
- [30] M. J. Santos and J. A. White, “Theory and simulation of angular hysteresis on planar surfaces,” *Langmuir*, vol. 27, no. 24, pp. 14868–14875, 2011.
- [31] W. Xu and C.-H. Choi, “From sticky to slippery droplets: dynamics of contact line depinning on superhydrophobic surfaces,” *Phys. Rev. Lett.*, vol. 109, no. 2, p. 024504, 2012.
- [32] B. M. Mognetti and J. M. Yeomans, “Modeling Receding Contact Lines on Superhydrophobic Surfaces,” *Langmuir*, vol. 26, no. 23, pp. 18162–18168, Dec. 2010.
- [33] B. Zhao, J. S. Moore, and D. J. Beebe, “Surface-directed liquid flow inside microchannels,” *Science*, vol. 291, no. 5506, pp. 1023–1026, 2001.
- [34] G. Sun, T. Liu, P. Sen, W. Shen, C. Gudeman, and C.-J. Kim, “Electrostatic Side-Drive Rotary Stage on Liquid-Ring Bearing,” *J. Microelectromechanical Syst.*, vol. 23, no. 1, pp. 147–156, 2014.
- [35] R. Dufour, P. Brunet, M. Harnois, R. Boukherroub, V. Thomy, and V. Senez, “Zipping effect on omniphobic surfaces for controlled deposition of minute amounts of fluid or colloids,” *Small*, vol. 8, no. 8, pp. 1229–1236, 2012.
- [36] J. W. Krumpfer, P. Bian, P. Zheng, L. Gao, and T. J. McCarthy, “Contact angle hysteresis on superhydrophobic surfaces: an ionic liquid probe fluid offers mechanistic insight,” *Langmuir*, vol. 27, no. 6, pp. 2166–2169, 2011.

Chapter 4 Electrostatically Driven Rotary Stage on Conductive Liquid Bearings

4.1 Introduction

Micromotors have been a signature MEMS device ever since the first micromotor was demonstrated by Fan, Tai and Muller [1]. However, even with considerable efforts to find applications and significant advances in MEMS fabrication technology for more than 20 years, the meaningful utility of micromotor – or more generally, rotating microdevices – has not been found. Two main limitations common to the existing rotating microdevices are: (1) friction against rotation and (2) difficulty of driving other devices. Friction has been found much larger than expected under microscale [1] so that reduced contact [1], [2] or fluid (i.e., air [3], [4] or liquid [5], [6]) lubrication is required to levitate the rotor. To drive other devices, various mechanisms have been used, including microscale gear trains [7], but the success has been limited. The difficulty of mechanical coupling with other devices led researchers to consider a system on the rotating device, which requires the availability of electricity on the rotor. However, electrical availability to the physically separated rotating element has usually been difficult. Even though electrical energy may be transmitted wirelessly in concept, the efficiency is an issue [8]. Apart from fully rotatable micromotors mentioned above, MEMS rotational components with limited rotational angles [9], [10] or limited direction [11] have also been developed while leaving at least one of above limitations unaddressed.

Here we aim to address the limitations mentioned above so as to create a low friction bearing that provides efficient and robust electrical power to the top of the rotor. Armed with the electrical availability to the rotor top, the rotating microdevice would become a

platform enabling various different applications, which we termed it a *rotary stage*, differentiating it from other micromotors and rotational components.

The entire rotary stage is an integrated microsystem that consists of many components and has to be realized in many phases with intensive collaboration. Overall, Prof. Chang-Jin “CJ” Kim, Prof. Chih-Kong Ken Yang, Prof. Yongho Sungtaek Ju and Dr. Chris Gudeman supervised the development of the rotary stage. My early study on the mechanism of liquid-rings bearings was greatly guided by Dr. Prosenjit Sen. The study on the static friction of the liquid rings, electrostatic side-actuation, and power transmission was developed together with Dr. Guangyi Sun which led to our publication in [12]. Integration of the entire rotary stage in microfabrication, which is normally very difficult, was mainly developed by Dr. Guangyi Sun and his collaboration with Dr. Chris Gudeman and Dr. Wenjiang Shen from Innovative Micro Technology (IMT). Prof. Sangwoo Lim provided valuable guidance on the study of electrochemical stabilities of ionic liquids. Mr. Jong Jin Kim and Mr. Yousr Ismail developed the PCB board for actuation and sensing and taught me a lot on capacitance sensing. Without all the above necessary studies and experiments, I would not be able to realize the final design, fabrication, actuation, and sensing of the bottom driven rotary stage to be presented in this Chapter. In this Introduction session, we first review different types of existing micro bearings and summarize their limitations and then analyze the difficulties in delivering power to a microscale rotating component.

4.1.1 Existing Micro Bearings for Rotation and Their Limitations

4.1.1.1 Solid-Solid Contact Bearings

Because of the well known solid-solid sliding friction [1], which manifests its effect more strongly in microscale, solid-solid contact bearings have been developed by minimizing the contact area, such as surface dimples [1], and using low energy coatings, such as octadecyltrichlorosilane (OTS) [13]. To improve, micro bearings based on solid-solid rolling friction has been implemented using micro balls [2] while still suffering from wear [1], [2], [14]. This is because, in order to overcome the large solid-solid contact friction, it requires high voltage, large current, or high magnetic field, etc. to actuate the device using electrostatic [1]–[3] ultrasonic [15], or magnetic [16] forces. Unlike in macroscale but well known in MEMS, thin-film of liquid actually promotes stiction problem due to the capillary effect.

4.1.1.2 Gas-Lubricated Bearings

To avoid solid-solid sliding [1] or rolling [2] friction and wear, some created a gas bearing [3], [4] through levitation, which required complicated fabrication and complex control of pressurized gas [3] or ultrasonic actuation [4] to maintain the levitation. Also the devices tend to suffer from a limited range of a stable operation. A combination of micro balls and pneumatic levitation could be a compromised solution which improve stability and reduce the complication of levitation control compared to gas bearings while reduce friction compared to solid-solid contact bearings, but at the price of complex fabrication and assembly [17].

4.1.1.3 Liquid Bearings

As the third option, liquid bearings [5], [6] are expected to avoid the solid-solid friction as well as the complexity of levitation the gas bearings require. Yet unfortunately, none of the solid-liquid bearing [5], [6] was found to provide a friction low enough to allow pure electrostatic actuation as one would commonly expect. Either the rotor was found tilting on a single droplet bearing and thus unstable for electrostatic actuation [5], or the startup torque became too large when satellite droplets were added to prevent tilting [6]. Because of the unknown large friction from the liquid bearing in [5], [6], macroscale permanent magnets were required for motor rotation. Very recently, inspired by our work to be presented in this chapter [18], [19], [12], a liquid droplet bearing on asymmetric ratchets were developed which harvest environmental vibration and translate it into one-direction rotational motion [11].

There exists another type of liquid-involved micromotors [20] where the liquid droplet is actually an electrowetting-based actuator instead of a bearing. Since liquid is used as an actuator, the droplet has to be of the same size as the rotor and hence strongly affect the stability of rotation (e.g., wobble) [20].

4.1.2 Difficulties in Power Transmission to Rotating Components

The inability to provide electrical power on to the rotating part limits the application of micromotors that have thus far been developed. We note that wiring to an infinitely rotating component is intrinsically difficult even in macroscale. This becomes even worse due to the demand of minimized contact for micro bearings, which does not allow a direct electrical power or signal transmission while lubricating for rotation. Although power or

signal transmission wirelessly (i.e., capacitive or inductive coupling) is possible, the level power and stability of transmittable of power and signal are severely limited.

4.2 Theory and Design

4.2.1 Overall Design

Figure 4-1 shows our design of the rotary stage on liquid-ring bearings. We utilize bearings with solid-liquid contact to avoid the solid-solid dry friction as well as the complexity of levitation the gas bearings require. Unlike liquid-droplet bearings, our bearings are designed to be concentric rings so that the entire system maintains cylindrical symmetry during rotating (i.e., no droplet sliding) while the each liquid ring can be utilized as a direct media to transmit both electrical power and signals if the liquid is electrically conductive (e.g., liquid metal or ionic liquid). Controlled rotational movement of the rotor is realized by electrostatic torque exert through rotor and stator electrodes.

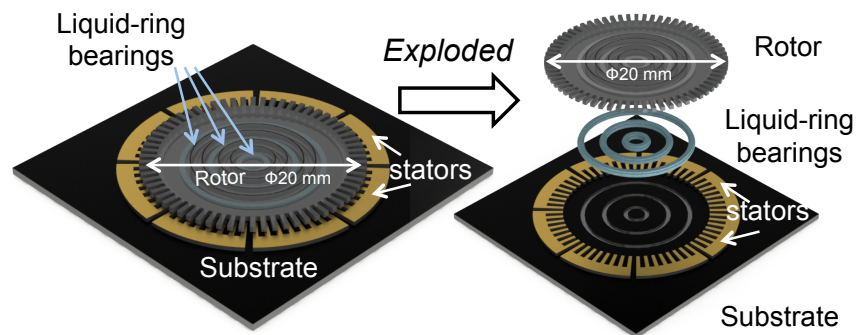


Figure 4-1 Schematic of the electrostatic bottom-driven rotary stage on liquid-rings bearings. We design our device to have 3 liquid rings and 66 electrode teeth on the rotor and 64 electrode teeth grouping as 8 stators.

4.2.2 Engineering Meniscus Shape to Form Liquid Rings

The key in our design is the liquid-ring bearings, which serve not only as mechanical bearings but also as electrical pathway to the top of the rotor. Here we show how we engineer the meniscus shape to be a ring by surface patterning through micro and nano fabrication and tailor the liquid ring to be a robust low-friction bearing. We note that such kind of liquid-ring bearings does not exist either in macroscale or in microscale. This is because liquid can legitimately serve as discrete mechanical elements only in microscale while it tends to become spherical droplets so as to minimize its surface area, satisfying the Young-Laplace's equation [21]. Therefore, a spherical shape is preferable unless the surface energy on the solid surface is modified into some certain pattern so that minimizing of free energy of the modified liquid-solid system prefers a different shape. Consequently, if we pattern the solid surface into a set of concentric rings using a non-wetting material, liquid will be constrained in to a set of rings, as shown in Figure 4-2(a). To prove this concept, we machined a set of concentric grooves on a Poly(methyl methacrylate) (PMMA) surface using a computer numerical control (CNC) mill and patterned the surface outside the groove with a low energy material, e.g., Teflon[®] in our case, while leaving the surface inside the groove hydrophilic. Upon water (dyed in blue color to be distinguished from the PMMA) dispersion, it preferably stayed inside the hydrophilic grooves in the shape of rings because of the preferable surface free energy, as illustrated in Figure 4-2(b).

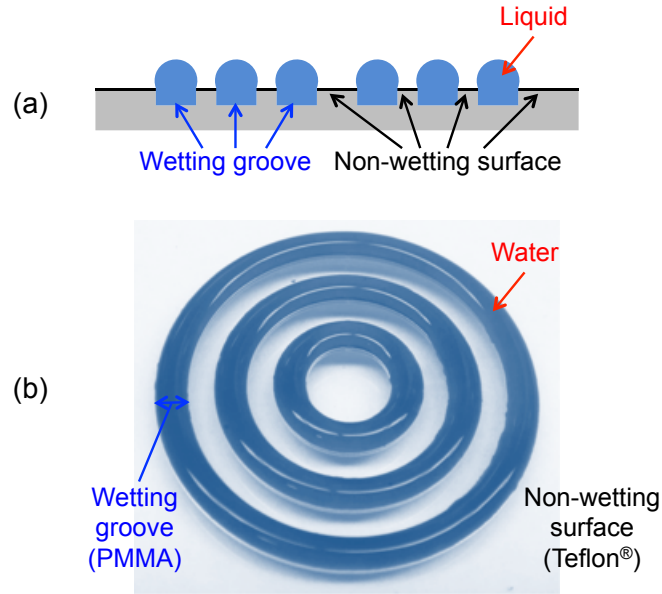


Figure 4-2 Formation of stable liquid rings. (a) Cross-sectional schematic of three liquid rings formed by wetting grooves and non-wetting outer surface (b) Three dyed water rings (blue) are formed on Teflon[®]-coated PMMA surface where PMMA is hydrophilic and Teflon[®] is hydrophobic

4.2.2.1 Liquid Rings as a Mechanical Bearing

Using the concept to form liquid rings, we can fabricate those grooves on both the rotor and stator and assembled them with liquid filled. Figure 4-3 shows the cross-sectional view of the rotary stage with magnified descriptions of one liquid ring. Restricted from spreading to the nonwetting surface outside the groove, the liquid ring is under a Laplace pressure defined by the curved meniscus (Figure 4-3a). With the rotor-substrate gap much smaller than the radius and width of the liquid ring, the vertical supporting force from the liquid rings can be expressed as

$$F_{\text{support}} = \sum_{i=1}^n \left(\Delta p_i A_{\text{ring}_i} - \gamma_{\perp} C_{\text{ring}_i} \right) \quad (4.1)$$

where F_{support} is the force provided by the liquid-ring bearings to support the rotor weight and payloads, n is the number of liquid rings (viz., $n = 3$ for our device), Δp_i is the

Laplace pressure, A_{ring_i} is the groove bottom area of the each liquid ring, γ_{\perp} is the vertical component of the surface tension, and C_{ring_i} is the total perimeter (i.e., including inner and outer) of each liquid ring. In horizontal direction, the horizontal component of surface tension centers the rotor to any external disturbances (Figure 4-3b). As a bearing, the designed liquid rings also provide small static and dynamic friction. Unlike multiple liquid droplets [6], the liquid rings avoid contact line movement and contact-angle hysteresis altogether, nearly eliminating the static friction. The wetting groove on a non-wetting surface, as opposed to a wetting pattern flush on a non-wetting surface, holds the liquid in place more securely and also increases the total height of the liquid ring so that it shears with a smaller viscous drag lubricating the rotational motions.

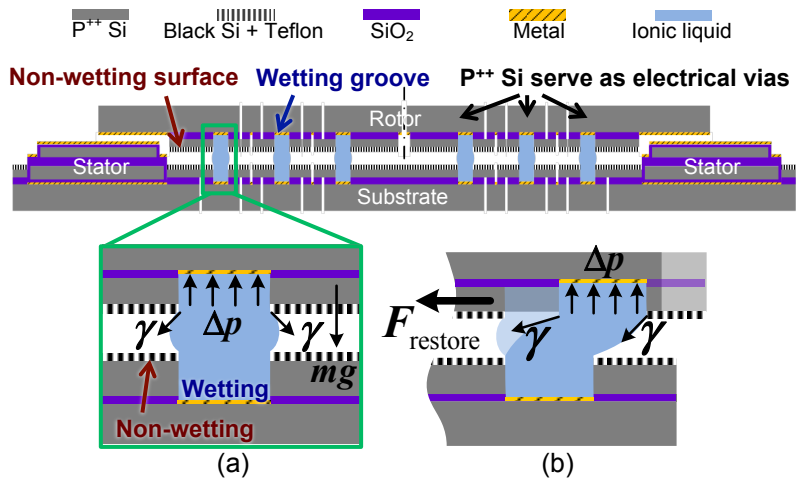


Figure 4-3 Cross-sectional view of the rotary stage.(a) Force balance of one liquid ring where the Laplace pressure built up from the curved meniscus support the rotor (b) Vertical stability provided by Laplace pressure. (c) Horizontal stability provided by surface tension pulling the rotor back to the center position

From Eq. 4.1, we know that the maximum vertical supporting force from a liquid-ring bearing is decided by the maximum Laplace pressure. It can be calculated from the

maximum meniscus angle (α) allowed on the non-wetting surface beyond which the liquid overflows. Based on the Young-Laplace equation,

$$\Delta p = p_l - p_v = \gamma \left(\frac{1}{R_1} + \frac{1}{R_2} \right) \quad (4.2)$$

where Δp is the Laplace pressure, i.e., pressure difference between the liquid and atmosphere (i.e., air), and R_1 and R_2 are radii of on mutually orthogonal planes [22]. Laplace pressure is then related to the shape of the meniscus, which is normally very complicated for liquid bridges sandwiched between two plates even if we neglect the gravitational and inertial distortion of the meniscus. For our liquid rings, rigorous math calculates the meniscus shape to be nodoids given by an elliptical integral [23], however, we can greatly simplify them to be circular arcs considering a much smaller rotor-substrate gap (h) compared to the radius and width of the liquid ring. Using the circular arc approximation, R_1 and R_2 are now in trigonometric functions (i.e., sine, cosine, and tangent) with the meniscus angle (α) and the Laplace pressure can be expressed as,

$$\Delta p = -\frac{2\gamma \cos \alpha}{h} = f(h) \quad (4.3)$$

where h is the distance between the rotor and substrate. We note that α in Eq. 4.3 is the meniscus angle of the outmost meniscus from the rotational center, which is the largest comparing with all other meniscus angles.

We can now analyze the vertical dynamic stabilities of the rotor from Eq. 4.3. If the rotor-substrate gap reduces from h to $(h-\Delta h)$ because of acceleration and we assume that the meniscus angle α does not instantaneously change, the restoring force will be solely from the changes of Laplace pressure, which can be calculated from the difference of Taylor expansion at $f(h-\Delta h)$ and $f(h)$,

$$\Delta p|_{h-\Delta h} - \Delta p|_h = f(h-\Delta h) - f(h) \approx \frac{f'(h)}{1!}(-\Delta h) = \frac{2\gamma \cos \alpha}{h^2}(-\Delta h) \quad (4.4)$$

from which the spring constant per unit area is then found to be $k = 2\gamma \cdot \cos \alpha / h^2$. Note that $k < 0$ when $\alpha > 90^\circ$ while $k > 0$ when $\alpha < 90^\circ$ leading to a very sensitive behavior for meniscus angle near 90° . Such sensitive reaction results in a very unstable (i.e., tilting) state if the meniscus angle along the liquid-ring groove varies around 90° because of the fabrication defect, which will be discussed in the next session (4.2.2.2). Other stabilities (e.g., horizontal and tilting stabilities) can be studied similarly. For example, the horizontal resorting force of a liquid ring with radius r_1 and r_2 can be calculated as:

$$F_{\parallel}(\Delta x)|_{r_1, r_2} \approx -4 \int_0^{\frac{\pi}{2}} \left[\gamma \frac{(\Delta x \cos \beta)}{h} \right] \cos \beta d\beta = -\frac{\pi(r_1 + r_2)\gamma}{h}(\Delta x) \quad (4.5)$$

where we approximate $\alpha \approx 90^\circ$ and $\Delta x \ll h$. The tilting restoring force comes from a combining effect of tilting and vertical compression which could also be studied numerically [24].

In summary, liquid ring serves as a mechanical bearing with vertical, horizontal, and anti-tilting stabilities when $\alpha > 90^\circ$. However, once $\alpha < 90^\circ$, it becomes unstable towards vertical and tilting disturbances. One possible way to reduce such kind of vertical and tilting instability is to increase the meniscus angle α so that it is no longer near 90° . To do so, we can reduce the width of the liquid ring on rotor or substrate so that the liquid ring has uneven width on top and bottom, as shown in Figure 4-4. Although vertical and tilting stabilities have been improved by uneven groove width configuration (Figure 4-4), the spring constant in vertical and horizontal has been reduced and would require the hydrophobic outer surface to be more hydrophobic (e.g., superhydrophobic) to properly confine the liquid inside the groove and prevent overflows.

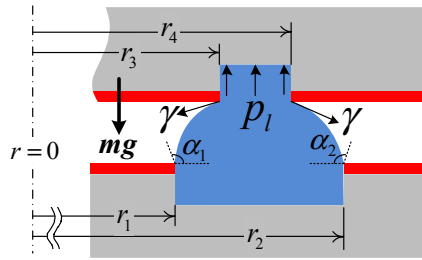


Figure 4-4 Liquid-ring groove with different width on the rotor and the substrate

4.2.2.2 Liquid Rings: Static and Dynamic Friction

In the ideal case, the liquid ring has no static resistance against rotation until it starts to rotate when viscous (i.e., dynamic) drag comes into the picture. This is because our design of the liquid bearing into a ring configuration that liquid always connects together and therefore, unlike the liquid bearing design as many droplets [5], [6], [11], no force is required to overcome the contact angle hysteresis of droplets sliding on the solid surface. However, because our liquid-ring bearing is based on surface tension which stabilizes against disturbances that would increase the surface energy (i.e., surface area), surface tension would create a capillary torque against rotation if the contact line should deviate from a perfect circle [25], which is the actuation force for electrowetting micromotor [20]. Figure 4-5 illustrates the distortion of the liquid-air interface when the contact line is distorted by a sinusoidal perturbation. We note the similarity of meniscus shape in Figure 4-5 and those contorted three-phase contact line we studied in Chapter 3. Thus, a low friction liquid bearing demands minimizing the fabrication defects along the contact line. As we point out in the previous session (4.2.2.1), the rotor becomes unstable when $\alpha < 90^\circ$ which can easily be the case for a distorted contact line as shown in Figure 4-5. Because those distortion decays exponentially [26], an elongated meniscus will eliminate

the capillary torque created by those defects. Because of this, the uneven groove width design also promotes low static friction against rotation since it extends the menisci.

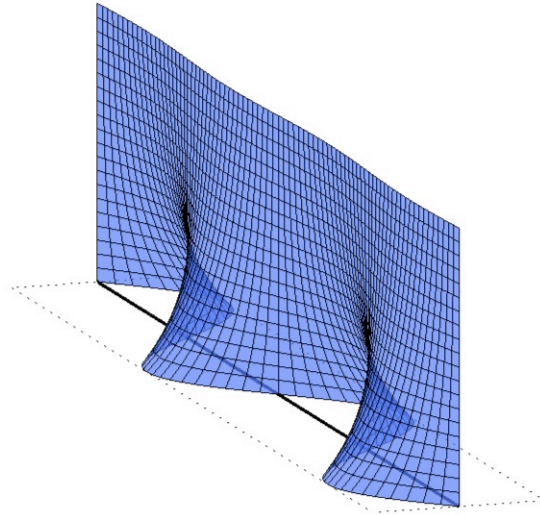
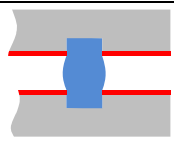
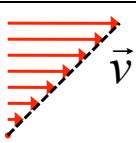
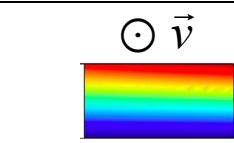
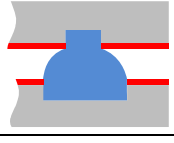
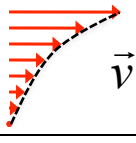
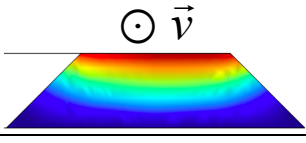
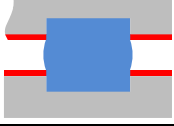
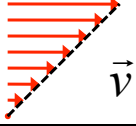
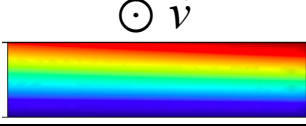


Figure 4-5 Distortion of the contact line lead to asymmetric of the meniscus

To study the dynamic drag of the liquid rings due to liquid viscosity, we used COMSOL to model the liquid ring numerically. Because of the small dimension of the rotor-substrate gap h , the liquids flow stays as laminar flow at moderate rotational speed. Taking the advantage of the axis symmetry of the rotary stage system, we model the system under 2-D axis symmetric module and study three different groove geometries. Their results are summarized in Table 4-1.

Table 4-1 Summary of COMSOL simulation on liquid-ring dynamic drag

Schematic of liquid ring cross section	Liquid-ring groove width (mm)	Velocity profile	Viscous drag (nN)	Cross section of the velocity flow (m/s)
	$d_{\text{rotor}} = 1$ $d_{\text{substrate}} = 1$		1258 ($\sim 50\% f_{v3}$)	
	$d_{\text{rotor}} = 1$ $d_{\text{substrate}} = 2$		1578 ($\sim 60\% f_{v3}$)	
	$d_{\text{rotor}} = 2$ $d_{\text{substrate}} = 2$		2521 (f_{v3})	

As shown in Table 4-1, the viscous drag was roughly proportional to the liquid-ring width on the rotor. Ideally, the liquid rings should be as narrow as possible. Considering the capability of handling and assembly, an uneven groove width design should be adopted at this stage since it provides comparable dynamic friction against rotation as narrow rings together with vertical and anti-tilting stabilities and low static friction while easier to handle experimentally. We will use the uneven groove width design for our device (although this detail is omitted in Figure 4-3 for clarity).

4.2.2.3 Liquid Rings as a Electrical Pathway

Unlike one large droplet in [5] or several sliding droplets in [6], the liquid rings may provide multiple electric paths to close a circuit and operate independent devices on top of an infinitely rotating rotor. When the electrically conductive liquid is used to form liquid rings, the electrical signals applied to the substrate can be transmitted through the electrical vias on the substrate then through the liquid rings and then through the electrical vias on the rotor and finally to the top of the rotor, as shown in Figure 4-6. We

selected an ionic liquid 1-Ethyl-3-methylimidazolium tetracyanoborate, i.e., [EMIM][TCB] to form the liquid rings because of its comparable surface tension with water, high conductivity, and stable electrochemistry (i.e., wide electrochemical window).

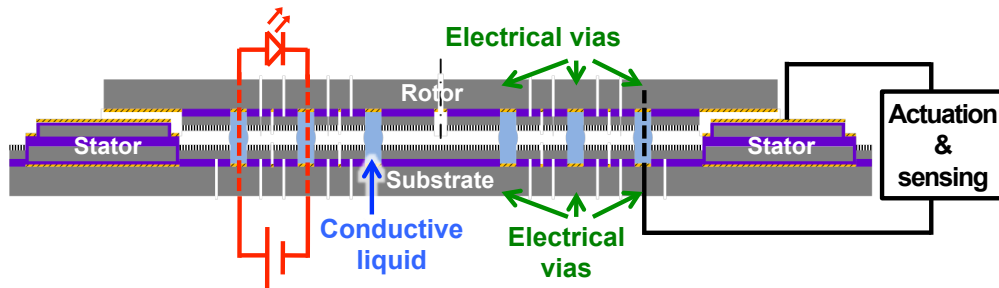


Figure 4-6 Electrical and sensing pathways provided by the liquid-ring bearings. The loop of red lines shows the electrical power and signal applied through the conductive liquid rings and transmitted to the top of the rotating rotor. The loop of black lines shows the electrical signal for actuation and position sensing also through conductive liquid rings

4.2.3 Actuation, Sensing, and Feedback Control

4.2.3.1 Electrostatic Actuation via Voltage Control Variable Capacitance

Variable capacitance electrostatic actuator utilizes electrostatic force/torque from the fringing field so as to minimize of energy in the system, which is, to be more specific for this case, to maximize the capacitance. This can be understood by considering a system that a capacitance is charged by a battery.

Originally, the battery has charges Q and with voltage V . After the charging process, some amount of charges has been moved to the capacitance so that the voltage across the capacitance is also V . Provided the linear relationship between the voltage and charge on a linear capacitor, $q = CV$, the charges in the battery now is $(Q-q)$. Thus, the total energy in the system (i.e. battery and capacitance) is

$$W_{\text{system}} = W_{\text{battery}} + W_{\text{capacitance}} = V(Q - q) + \int_0^q V dq' = VQ - \frac{1}{2}CV^2 \quad (4.6)$$

In a voltage control actuation, V is fixed. Therefore, the only way that the system can minimize its total energy is to maximize the capacitance, and thus causing actuation on the movable part (e.g., one electrode of the capacitor). We can see that the way of thinking how the actuator will behave in terms of maximization of capacitance is pretty helpful for the discussion here after.

It is mathematically convenient to use the co-energy concept to model the voltage controlled electrostatic actuator [27]. The lumped circuit for a general electrostatic actuator is shown in Figure 4-7. In the rotary stage, the equivalent spring (with compliance $1/k$ in Figure 4-7) against rotation comes from the spring-like resistance force from deformed meniscus of the liquid ring (Session 4.2.2.2). Note that the energy stored in this “spring” will be dissipated once the meniscus is broken due to large deforming by rotation of the rotor.

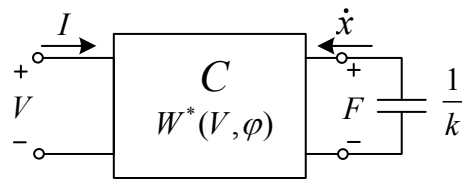


Figure 4-7 Equivalent lumped circuit of an electrostatic transducer

From the capacitance of the actuator, which is determined by geometry and environment (i.e., permittivity), we can write the co-energy as $W^*(V, \varphi) = \frac{1}{2}CV^2$. Then the electrostatic

torque is calculated by taking the partial derivative of W^* with respect to the changing variable, which is the rotating angle φ in our rotating stage, i.e. $\tau_{\text{electrostatic}} = \frac{\partial W^*(V, \varphi)}{\partial \varphi}$.

There are two different configurations to electrostatically actuate the rotary stage: side driving and bottom driving. Both of them have been used in the development of previous rotary stages [1], [2]. Fan et al. used side driving to realize rotation and pull up the rotor to reduce the friction at the same time [1], while Ghalichechian et al. used bottom driving to maximize the rotational force from the fringing field which unfortunately also increase the rolling friction due to the increased load from electrostatic attraction [2]. When the capacitance in our rotary stage is design to be a fan shape that each electrode occupies some certain angle. The geometry of the side drive rotor and stator is shown in Figure 4-8.

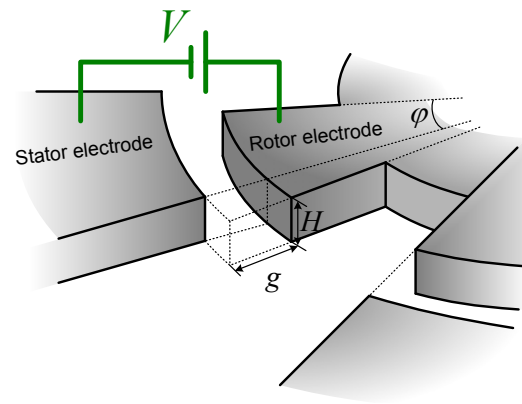


Figure 4-8 Electrostatic side-driving configuration

Assuming the gap is small so that the radian capacitor can be treated as a parallel plate capacitor. Thus, the capacitance per unit radian for the side drive configuration (Figure 4-8) is,

$$C_{\varphi} = \frac{\varepsilon A_{\varphi}}{g} = \frac{\varepsilon RH}{g} \quad (4.7)$$

in which R is the mean radius of the rotor and stator, H is the thickness of the rotor and g is the gap between the rotor electrode and stator electrode (Figure 4-8).

For an electrode with angle φ , the capacitance is expressed as $C = \varphi C_{\varphi} = \frac{\varphi \varepsilon RH}{g}$.

When the voltage across the rotor and stator electrode is V , the co-energy is,

$$W^*(V, \varphi) = \frac{1}{2} C V^2 = \frac{\varphi \varepsilon RH}{2g} V^2 \quad (4.8)$$

Thus, the electrostatic torque yields,

$$\tau_{\text{electrostatic}} = \frac{\partial W^*(V, \varphi)}{\partial \varphi} = \frac{\partial}{\partial \varphi} \left[\frac{\varphi \varepsilon RH}{2g} V^2 \right] = \frac{\varepsilon RH}{2g} V^2 \quad (4.9)$$

As seen in Eq. 4.9, the electrostatic torque is proportional to the thickness of the rotor, the radius of the rotor and inverse proportional to the gap. That indicates the electrostatic torque scales down as L^1 . However, as in the usual case of MEMS, the H is the thickness of the silicon wafer and is fixed. Therefore, the electrostatic torque is fixed when we scale it down in this manner. On the other hand, the electric field tries to minimize the electrostatic gap and thus shift the rotor. Luckily, we can activate two stator electrodes along a diameter so that forces are balanced, ensuring free of touching, as long as the number of electrodes on the rotor and stator are designed to be even numbers.

Figure 4-9 shows the structure of the bottom-driving rotor and stator. Note that in the bottom driving configuration, the electrostatic gap g does not necessarily equals to the rotor-substrate gap h . In other words, we can engineer the electrostatic gap g to maximize the capacitance for actuation and sensing.

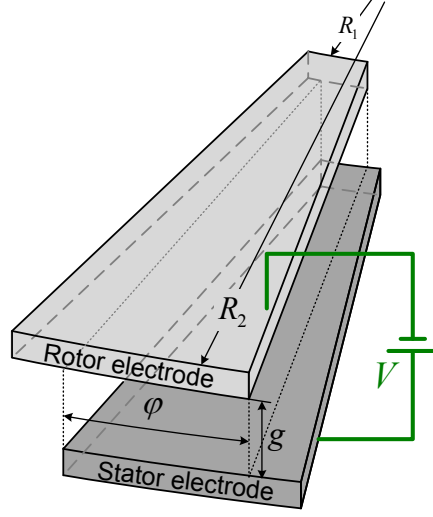


Figure 4-9 Electrostatic bottom-driving configuration

Again, we assume small gap such that approximation as a parallel plate capacitor valids.

The capacitance per unit radian for the bottom-driving configuration is,

$$C_{\varphi} = \frac{\varepsilon A_{\varphi}}{g} = \frac{\varepsilon \pi (R_2^2 - R_1^2)}{g \cdot 2\pi} = \frac{\varepsilon (R_2^2 - R_1^2)}{2g} \quad (4.10)$$

in which R_1 and R_2 are the two radius of the boundary of the electrodes.

For an electrode has angle φ , the capacitance is expressed as $C = \varphi C_{\varphi} = \frac{\varphi \varepsilon (R_2^2 - R_1^2)}{2g}$.

When the voltage across the rotor and stator electrode is V , the co-energy is,

$$W^*(V, \varphi) = \frac{1}{2} C V^2 = \frac{\varphi \varepsilon (R_2^2 - R_1^2)}{4g} V^2 \quad (4.11)$$

Therefore, the electrostatic torque is calculated to be,

$$\tau_{\text{electrostatic}} = \frac{\partial W^*(V, \varphi)}{\partial \varphi} = \frac{\partial}{\partial \varphi} \left[\frac{\varphi \varepsilon (R_2^2 - R_1^2)}{4g} V^2 \right] = \frac{\varepsilon (R_2^2 - R_1^2)}{4g} V^2 \quad (4.12)$$

Compared to the side driving case, where the electrostatic torque scales down as L^1 , the electrostatic torque from the bottom-driving configuration is independent on the thickness

of the rotor and decided by R_1 and R_2 in Eq. 4.12, i.e., the parameters determined by the layout. Note that such increase of overlapping area might cause the rotor to tilt or snap down due to the pull-in effect of electrostatic instability. Fortunately, however, the liquid rings provide some resistance to tilting, restoring the rotor back to the level position.

Capacitive sensing, as we shown in Figure 4-6, is automatically integrated with the electrostatic actuation. We note that bottom-driving design has advantage over side-driving design for sensing in that it is not limited by the rotor thickness.

4.2.3.2 Design of Bottom Driven Electrodes for Actuation and Sensing

Proven by our early system development, the side driving is easier to handle in the sense that it is more stable against tilting [12]. However, we focus on developing the more challenging bottom driven rotary stage here because, by positioning the stator electrodes underneath the rotor (Figure 4-3), the device assembly becomes much simpler and the electrode overlaps much larger to assist the capacitive sensing. We also point out that, although the liquid-ring bearings provide some inherent stability against tilting, a successful bottom driving and sensing would still require careful design and fabrication. The rotational electrostatic force should overcome the static friction of the bearings before the electrostatic attraction between the opposing electrodes overpowers the inherent stability. Also note that in our design, stators are fabricated separately and later bonded to the substrate to obtain a smaller rotor-stator distance (i.e., electrostatic gap g), which will maximize the electrostatic force for actuation and the capacitance for sensing while keeping a reasonable rotor-substrate gap h for assembly. Figure 4-10 shows an equivalent circuit of the sensing path through actuation electrodes on the stator and the

rotor, which is connected by vias on the substrate, conductive liquid, and vias on the rotor in our design (Figure 4-3).

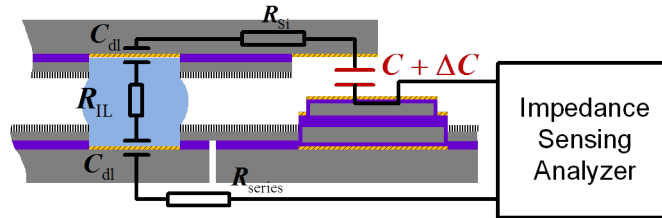


Figure 4-10 Equivalent circuit of the sensing path through actuation electrodes on stator and the rotor. The electrical connection to the rotor is provided through substrate electrode, conductive liquid rings and vias on both the substrate and rotor.

4.3 Experiments

4.3.1 Fabrication and Assembly

The device was fabricated on SOI wafers. Figure 4-11 (a) depicts the process flow to fabricate the rotor. A group of actuation teeth and electrical isolation trenches were first etched for the rotor on the handle layer (300-350 μm thick) down to the buried-oxide layer using deep reactive-ion etching (DRIE). Then black silicon was formed on the device layer (100-150 μm thick) and made superhydrophobic by spin-coating a ~ 150 nm thick Teflon[®] AF 1600. Next, the grooves for the liquid were etched down to the buried-oxide layer with sequential oxide removal by reactive-ion etching (RIE). Finally, a 50 nm/50 nm thick Ti/Pt layer was evaporated and lifted off, leaving the grooves chemically compatible with the ionic liquid (i.e., [EMIM][TCB]). The substrate was fabricated with exactly same steps as the rotor but with a mask layout removing the actuation teeth on the handle layer while including stators-positioning slots on the device layer (Figure 4-11b). Figure 4-11(c) shows the stator electrodes fabricated also on an SOI wafer. An SOI wafer

with 300-350 μm -thick handle layer and 50-100 μm -thick device layer was chosen to obtain ~ 50 μm rotor-stator distance (g) for electrostatic bottom driving actuation after assembly. Eight discrete stators and one unbroken base were patterned on the device layer and the handle layer using DRIE, respectively. Next, the stators were put into an oxidation furnace to oxidize the sidewall of the stators to ensure an absolute isolation between them. Finally, a 50 nm/50 nm-thick Cr/Au layer was evaporated onto the surface of the stators to have a good electric contact to testing probes. The stators were then placed into the etched stator-positioning slots and bonded by CYTOP[®]. Due to the complication of our device, 3-D angled views of Figure 4-11(a) are shown in Figure 4-12 for better illustration of the rotor fabrication process.

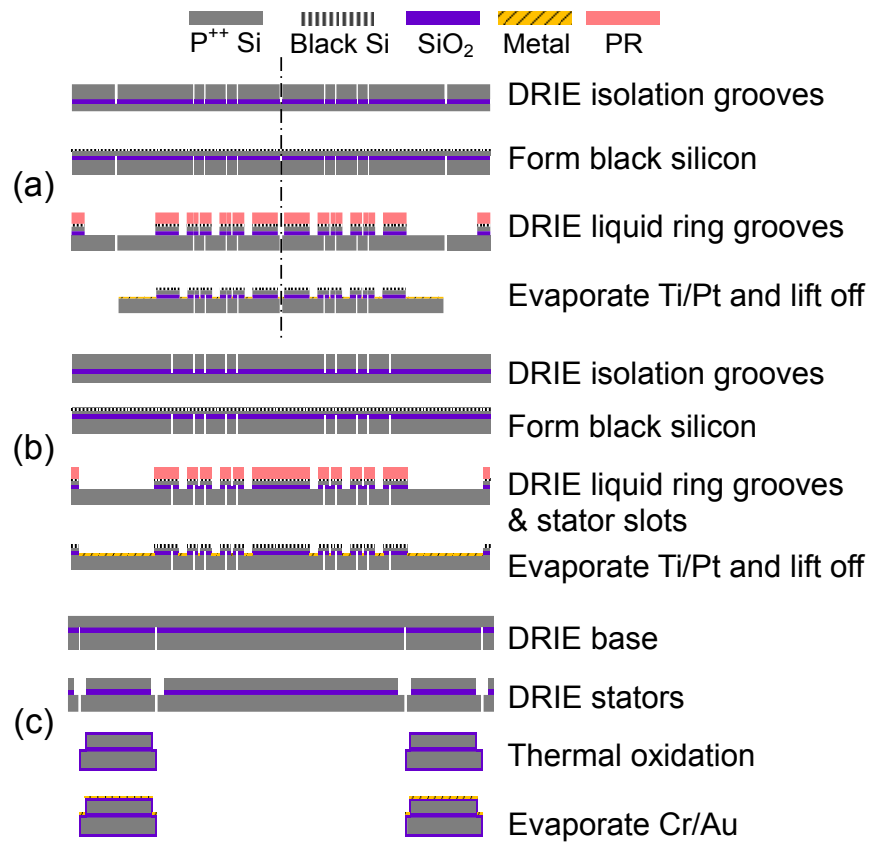


Figure 4-11 Process flows to fabricate (a) the substrate, (b) the rotor, and (c) the stators

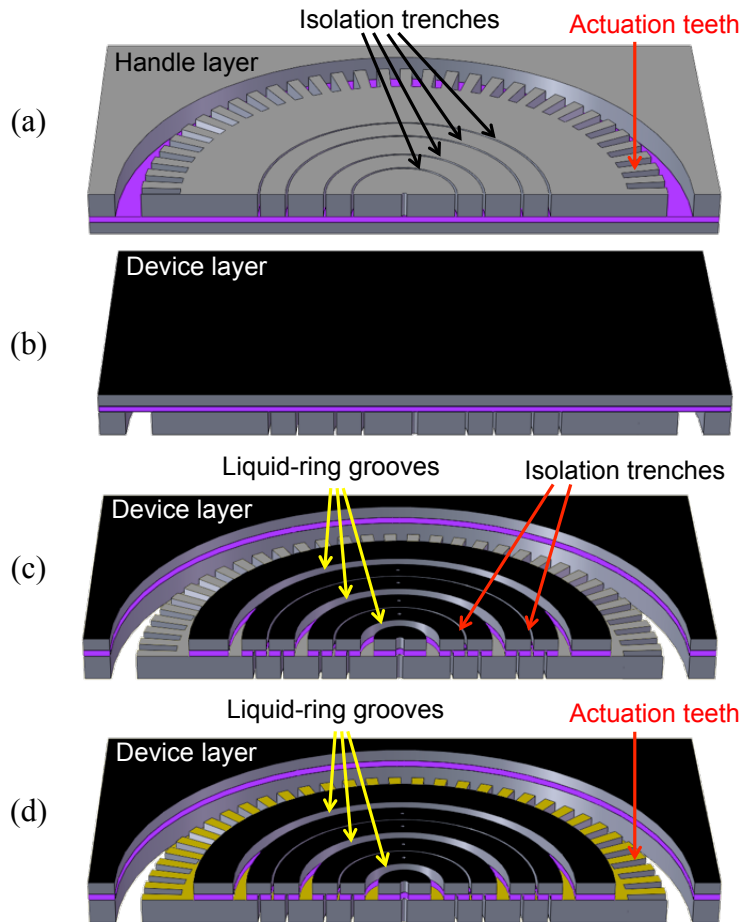


Figure 4-12 3-D illustration of process to fabricate rotor (similar for the substrate as well). (a) DRIE actuation teeth and isolation trenches on handle layer. (b) Form black Si on device layer and coat Teflon[®]. (c) DRIE liquid-ring grooves and isolation trenches on device layer. (d) Evaporate and lift off Ti/Pt layer to metalize actuation teeth and provide chemical innerness to the solid-liquid interface.

4.3.2 Tests

Test of a rotary stage includes device assembly, electrostatic actuation, sensing, and feedback control. Additional device characterization depends on specific application.

4.4 Results and Discussion

4.4.1 Fabricated Device and Assembly

Figure 4-13 shows the fabrication and assembly results. Figure 4-13 (a) and (b) show the rotor and stator-bonded substrate with ionic liquid (i.e., [EMIM][TCB]) rings formed inside the designated groove without wetting the outside superdophobic black silicon surface. The thin isolation grooves amid different liquid rings established $>16 \text{ G}\Omega$ resistance (measured by Agilent B1500A device analyzer) for isolation. All teeth on the rotor were connected together with the Ti/Pt layer and connected to the outer ring to be biased for actuation and sensing. With the matching groove pattern on the rotor and the substrate, the rotor was then flipped over, dropped, and self-assembled to the substrate by the liquid rings, as shown in Figure 4-13 (c) and (d).

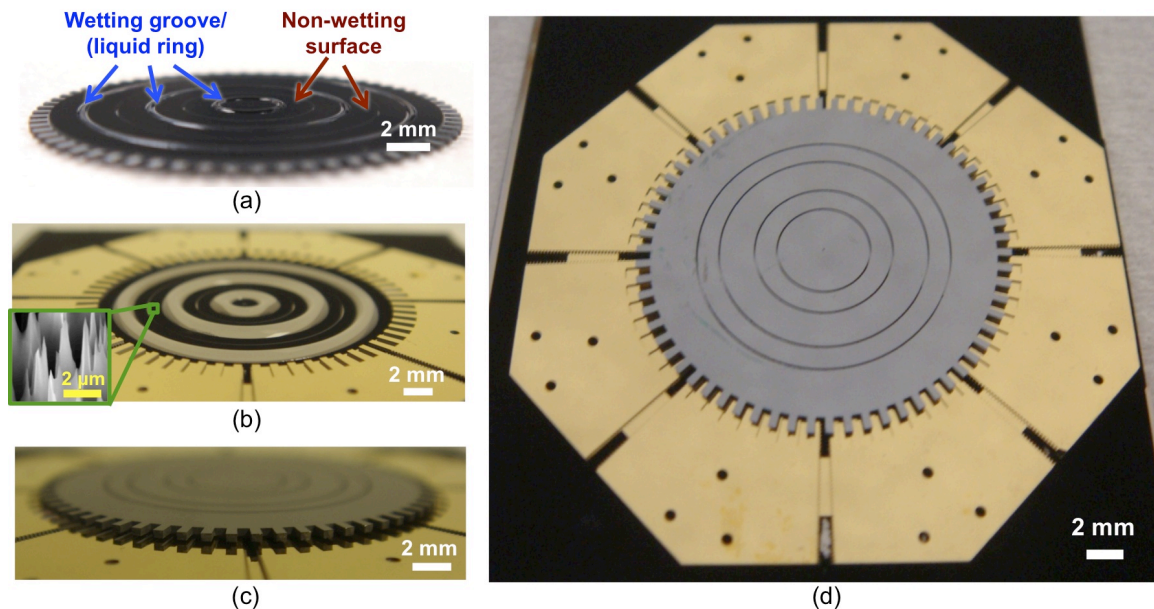


Figure 4-13 Fabricated rotary stage and assembly. (a) Rotor with dispensed ionic liquid rings. (b) Substrate and bonded 8 stators with dispensed ionic liquid rings; Inset shows the SEM image of the black silicon structures. (c-d) Rotor flipped over and assembled to the substrate by liquid rings with the gap controlled by liquid volume.

The rotor-substrate gap was controlled by the amount of the liquid used to form the liquid rings. Figure 4-14 shows the measured liquid volume of the outmost liquid ring in well agreement with ones predicted through simulation results from Surface Evolver [28]. Considering the axisymmetric of the liquid ring meniscus, we use the string model (shown as the cross sections in the insets of Figure 4-14) in Surface Evolver to compute surfaces of revolution which greatly reduces the computation load. Because the tilting is more sensitive to the inner liquid rings, we assembled the rotary stage with the outer rings dominating the rotor-substrate gap so as to gain the best balance. With such a controllable rotor-substrate gap, we assembled our device to have electrostatic gap $g \sim 50 \mu\text{m}$ which increase the sensing signal by 5-10 times compared with side driving case [12] so that sensing becomes more feasible.

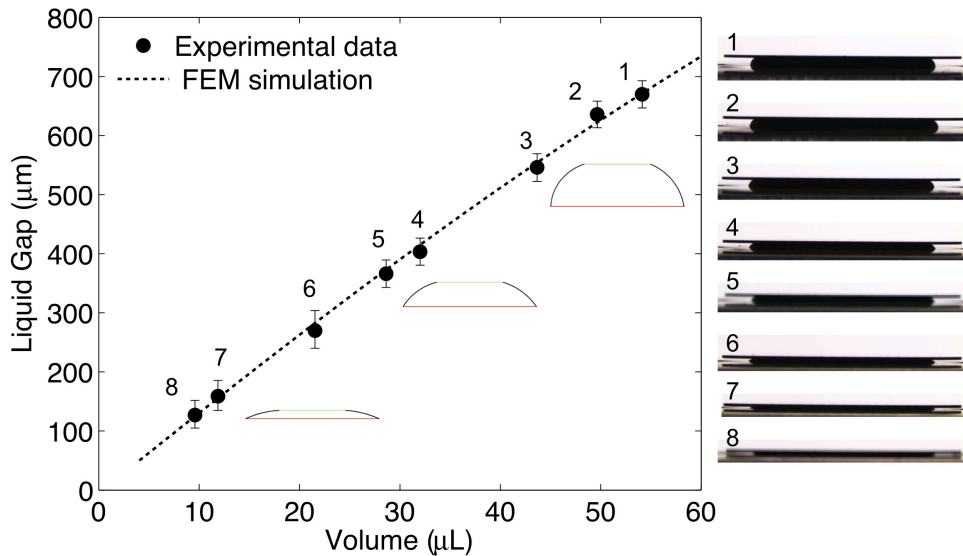


Figure 4-14 Rotor-substrate gap controlled through liquid volume to form the liquid ring. The experimental measured liquid volume (black circles) matched the simulation results (dash line) very well. The error bars show the range of ± 1 pixel error from image analysis. Three insets show the cross section of the meniscus shape of the liquid ring from Surface Evolver simulation. Experimental side views of the eight cases are shown on the right to the plot showing a large range of controllable rotor-substrate gap (h).

4.4.2 Electrostatic Actuation and Start-Up Torque

Electrostatic continuous actuation has been achieved by grounding the rotor through one of the liquid ring (e.g., outer ring in our device) and consecutively applying DC voltages to stators (Figure 4-6). In our test, a minimum 14.1 V_{DC} was needed to robustly rotate the rotor on 3 ionic liquid rings, corresponding to a 0.89 nN•m start-up torque (estimated by Eq. 4.12). Table 4-2 compares the start-up torque of different bearings from literature to our results published in [18]. We note that a direct comparison of the start-up torque between devices with various sizes is inappropriate and thus normalization is needed for a fair comparison. Considering different physics, we performed two different normalization approaches. First, we normalize the start-up torque by the origins of its friction now that the start-up torque is to overcome the static frictional force inherent in certain type of bearings. For solid bearings, the static frictional force is proportional to the contact area, i.e., $\tau \propto L^2$. For gas bearings, the friction is ~ 0 . For liquid bearings, the static friction comes from the distortion of the contact line and hence $\tau \propto L$. Without knowing the details of actual contact area of a solid bearing and contact line of a liquid bearing, a normalization using the rotor diameter will actually lead to inaccurate results. However, we argue that, even this comparison is not fair for liquid bearings, because the start-up torques of solid bearings are greatly underestimated (since we divide the torque by the rotor surface area which is much larger than the actual contact), if our liquid ring(s) still show much smaller start-up torque, which is the results shown in Table 4-2, it definitely confirms the low-friction nature of our liquid-ring bearings. Second, we performed normalization based on the area moment of inertia which lead to $\tau \propto L^4$. We note that this normalization is fair for all bearings while it is not suitable for start-up

situations since the area moment of inertia indicate how difficult an object can be accelerated when it is rotating and thus nonrelated to the start-up torque which requires infinite acceleration theoretically. Even though we lack a proper dimensionless number to fairly compare the performance between different types of bearings, the last three rows in Table 4-2 clearly show the low static friction of our liquid-ring bearings [18], [19], [12], no matter which normalization was used. To compare the current bottom-driven device [18] with two other side-driven rotary stages developed earlier [19], [12], the normalization based on the friction mechanism should be used since they are all liquid bearings. We note that the uneven liquid-ring groove design in [18] has reduced ~90-95% of the start-up torque comparing to [19], [12] accounting for the additional friction of the three liquid rings (vs. the one liquid ring in [19] or two liquid rings in [12]). Such reduction in start-up torque is critical to the success of bottom driving since rotation could be realized at low actuation voltage so that rotor tilting or snapping-down was avoided.

Table 4-2 Start-up of rotary stages of different bearings

Bearing type		Rotor diam. (mm)	Actuation method	Measured start-up torque (nN•m)	Normalized start-up torque by friction mechanism (nN•m)	Normalized start-up torque by area moment of inertia (nN•m)	Ref.
Solid	Sliding	0.06	Electrostatic side drive	0.00096	106	1.2×10^7	[1]
		1	Ultrasonic	1000	4×10^5	1.6×10^8	[4]
	Rolling	14	Electrostatic bottom-drive	220	449	916	[2]
Gas	Floating	4.2	Electrostatic induction	≈ 0	≈ 0	≈ 0	[3]
Liquid	Center droplet	10	Magnetic	150	300	2400	[5]
	Center + satellite droplets	10	Magnetic	300	600	4800	[6]
	1 liquid ring	30	Electrostatic side drive	10	6.7	1.97	[19]
	2 liquid rings	30	Electrostatic side drive	8.13	5.42	1.60	[12]
	3 liquid rings	20	Electrostatic bottom drive	0.89	<u>0.89</u>	<u>0.89</u>	[18]

4.4.3 Position Capacitive Sensing and Feedback Control

Besides the low actuation voltage, the bottom-driving scheme also equips us with a capacitive sensing for a feedback control. Preliminary sensing test configuration is shown in Figure 4-15. We used a DAQ (National Instrument USB-6259) to control the switching of relays to apply a ~ 15 V_{DC} between the 4 adjacent stators and the rotor (grounded through outer liquid ring) while sensing the rotor position with another stator by a capacitance measurement tool (Agilent B1500A device analyzer). With a 10 kHz 250 mV_{AC} sensing signal, the change of capacitance between the moving rotor and the fixed stator could be measured by the device analyzer. With the position fixed by sequential actuation of the 4 stators, changes in phase of the impedance were measured through different rotor positions displaying periodicity as modeled (Figure 4-16). Those data can be utilized to facilitate faster and more accurate rotation by feedback control.

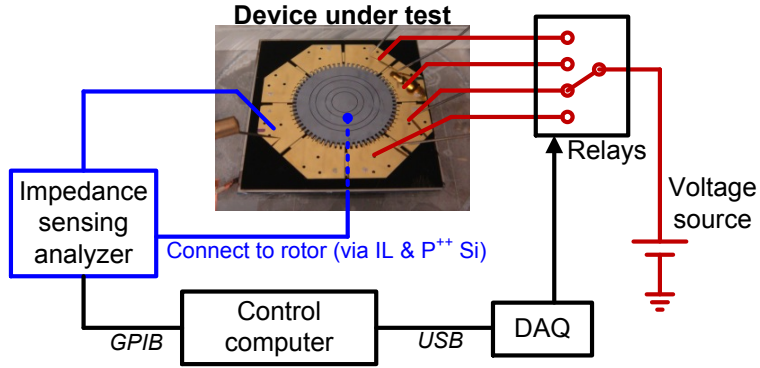


Figure 4-15 Schematic of actuation, sensing and feedback circuit. The rotor electrodes were grounded by the outer ionic liquid ring.

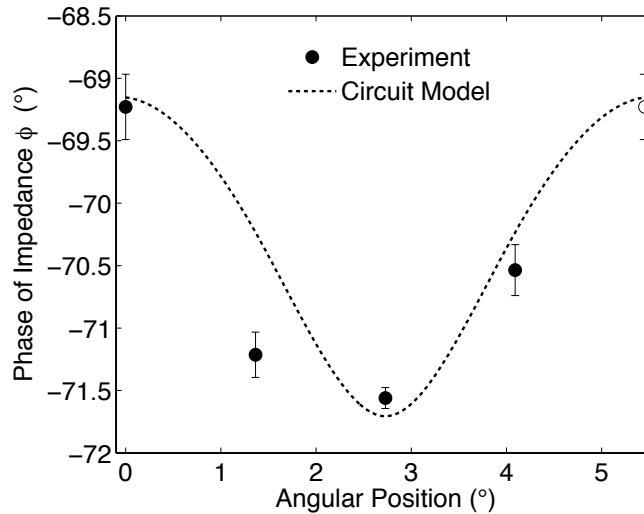


Figure 4-16 Phase of impedance measured at different rotor positions. The measured periodic phase changes as predicted by the equivalent circuit of the sensing path shown in Figure 4-10.

4.5 Summary and Future Works

We have demonstrated the design, fabrication, and electrostatic bottom-driving actuation and sensing of a centimeter-size rotary stage. Three conductive ionic liquid rings served as both mechanical bearings and electrical connections. Intrinsically stable in vertical as well as horizontal direction, the designed liquid ring bearings also provided low friction and wear-free rotations when the fabrication defects along the edge of the liquid grooves

were minimized. A mere ~ 15 V_{DC} was necessary to actuate the fabricated rotary stage on three conductive rings of an ionic liquid. In addition, a capacitive sensing has been realized for the first time, exploiting the bottom-driving configuration. We foresee that active devices (e.g. an LED, 1-axis gyroscope, etc.) could be electrically operated on an infinitely spinning rotor in our rotary stage system.

In the future, more fundamentally study will be required to better understand the mechanism of uneven liquid-ring groove width although it has already provided good results for the current device. The fundamental study will help optimizing the design to further improve the performance of the rotary stage system. Other possible conductive liquids should also be investigated since ionic liquids can only be operated within its electrochemical window, beyond which electrolysis occurs to limit the level of power and reliability of signals it can carry for real applications.

4.6 References

- [1] L.-S. Fan, Y.-C. Tai, and R. S. Muller, "IC-processed electrostatic micromotors," *Sens. Actuators*, vol. 20, no. 1–2, pp. 41–47, 1989.
- [2] N. Ghalichechian, A. Modafe, M. I. Beyaz, and R. Ghodssi, "Design, Fabrication, and Characterization of a Rotary Micromotor Supported on Microball Bearings," *J. Microelectromechanical Syst.*, vol. 17, no. 3, pp. 632–642, 2008.
- [3] L. G. Frechette, S. F. Nagle, R. Ghodssi, S. D. Umans, M. A. Schmidt, and J. H. Lang, "An electrostatic induction micromotor supported on gas-lubricated bearings," in *Micro Electro Mechanical Systems, 2001. MEMS 2001. The 14th IEEE International Conference on*, 2001, pp. 290–293.
- [4] V. Kaajakari and A. Lal, "Micromachined ultrasonic motor based on parametric polycrystalline silicon plate excitation," *Sens. Actuators Phys.*, vol. 137, no. 1, pp. 120–128, 2007.
- [5] M. L. Chan, B. Yoxall, H. Park, Z. Kang, I. Izyumin, J. Chou, M. M. Megens, M. C. Wu, B. E. Boser, and D. A. Horsley, "Design and characterization of MEMS

- micromotor supported on low friction liquid bearing,” *Sens. Actuators Phys.*, vol. 177, pp. 1–9, 2012.
- [6] B. E. Yoxall, M. L. Chan, R. S. Harake, T. Pan, and D. A. Horsley, “Rotary Liquid Droplet Microbearing,” *J. Microelectromechanical Syst.*, vol. 21, no. 3, pp. 721–729, 2012.
- [7] J. A. Walraven, T. J. Headley, A. B. Campbell, and D. M. Tanner, “Failure analysis of worn surface-micromachined microengines,” 1999, vol. 3880, pp. 30–39.
- [8] P.-J. Chen, S. Saati, R. Varma, M. S. Humayun, and Y.-C. Tai, “Wireless Intraocular Pressure Sensing Using Microfabricated Minimally Invasive Flexible-Coiled LC Sensor Implant,” *J. Microelectromechanical Syst.*, vol. 19, no. 4, pp. 721–734, Aug. 2010.
- [9] M. Stranczl, E. Sarajlic, H. Fujita, M. A. M. Gijs, and C. Yamahata, “High-Angular-Range Electrostatic Rotary Stepper Micromotors Fabricated With SOI Technology,” *J. Microelectromechanical Syst.*, vol. 21, no. 3, pp. 605–620, Jun. 2012.
- [10] U. Baran, W. O. Davis, S. Holmstrom, D. Brown, J. Sharma, S. K. Gokce, and H. Urey, “Linear-Stiffness Rotary MEMS Stage,” *J. Microelectromechanical Syst.*, vol. 21, no. 3, pp. 514–516, Jun. 2012.
- [11] C. Varel and K. F. Bohringer, “Liquid droplet micro-bearings on directional circular surface ratchets,” in *2014 IEEE 27th International Conference on Micro Electro Mechanical Systems (MEMS)*, 2014, pp. 983–986.
- [12] G. Sun, T. Liu, P. Sen, W. Shen, C. Gudeman, and C.-J. Kim, “Electrostatic Side-Drive Rotary Stage on Liquid-Ring Bearing,” *J. Microelectromechanical Syst.*, vol. 23, no. 1, pp. 147–156, 2014.
- [13] R. Maboudian and R. T. Howe, “Critical Review: Adhesion in surface micromechanical structures,” *J. Vac. Sci. Technol. B*, vol. 15, no. 1, pp. 1–20, Jan. 1997.
- [14] M. Mehregany, S. D. Senturia, and J. H. Lang, “Measurement of wear in polysilicon micromotors,” *IEEE Trans. Electron Devices*, vol. 39, no. 5, pp. 1136–1143, May 1992.
- [15] P. Muralt, “Ultrasonic Micromotors Based on PZT Thin Films,” *J. Electroceramics*, vol. 3, no. 2, pp. 143–150, Jun. 1999.
- [16] C. H. Ahn, Y. J. Kim, and M. G. Allen, “A planar variable reluctance magnetic micromotor with fully integrated stator and coils,” *J. Microelectromechanical Syst.*, vol. 2, no. 4, pp. 165–173, 1993.

- [17] M. McCarthy, C. M. Waits, M. I. Beyaz, and R. Ghodssi, "A rotary microactuator supported on encapsulated microball bearings using an electro-pneumatic thrust balance," *J. Micromechanics Microengineering*, vol. 19, no. 9, p. 094007, 2009.
- [18] T. Liu, G. Sun, J. J. Kim, C.-K. K. Yang, and C.-J. Kim, "Electrostatic bottom-driven rotary stage on multiple conductive liquid-ring bearings," in *Proc. IEEE Int. Conf. MEMS*, 2013, pp. 86–89.
- [19] G. Sun, T. Liu, P. Sen, W. Shen, C. Gudeman, and C.-J. Kim, "Electrostatically driven rotor on conductive liquid ring bearings," in *Proc. Actuator Microsystems Workshop, Tech. Dig. Solid-State Sensor*, 2012, pp. 78–81.
- [20] A. Takei, K. Matsumoto, and I. Shomoyama, "Capillary motor driven by electrowetting," *Lab. Chip*, vol. 10, no. 14, pp. 1781–1786, 2010.
- [21] P. S. Laplace, *Traité de mécanique céleste*, vol. 4. de l'Imprimerie de Crapelet, 1805.
- [22] A. W. Adamson and A. P. Gast, *Physical Chemistry of Surfaces*, 6 edition. New York: Wiley-Interscience, 1997.
- [23] S. A. Nezamoddini, "Capillary force actuators," Ph.D. Dissertation, University of Virginia, 2008.
- [24] Y. Zhan, "Study of characteristics of liquid-based bridge structure as mechanical elements," M.S. thesis, University of California, Los Angeles, 2012.
- [25] A. Takei, K. Matsumoto, and I. Shimoyama, "Capillary torque caused by a liquid droplet sandwiched between two plates," *Langmuir*, vol. 26, no. 4, pp. 2497–2504, 2009.
- [26] P.-G. de Gennes, F. Brochard-Wyart, and D. Quéré, *Capillarity and wetting phenomena : drops, bubbles, pearls, waves*. New York: Springer, 2004.
- [27] S. D. Senturia, *Microsystem Design*. Boston, MA: Kluwer Academic Publishers, 2001.
- [28] K. A. Brakke, "The surface evolver," *Exp. Math.*, vol. 1, no. 2, pp. 141–165, 1992.

Chapter 5 Superomniphobic Surface Repellent to All Liquids

5.1 Introduction

Understanding the extraordinary liquid repellency of natural surfaces [1], [2] has affected a wide range of scientific and technological areas, from coatings [3], heat transfer [4], drag reduction [5], to biological applications [6]. Although inspiration are originated from nature, scientific intuitions and engineering practice date back from a time (e.g., [7] in 1936, [8] in 1944, and [9] in 1953) even earlier than the secret of those natural surfaces started to be understood by the advancement of imaging tools such as scanning electron microscopy (SEM) which was matured in the mid-1960s. Learning from this fact, we are to create a surface super-repellent to all liquids that has neither been found in nature nor man made. We first review some natural and engineering super-repellent surfaces and their liquid-repellent mechanism and then explain, by reasoning, our philosophy towards omni-liquid repellency.

5.1.1 Natural Super-repellent Surfaces

Many natural surfaces, such as lotus leaves and water strider's leg, have shown strike water repellency so that they are clean and dry even from "dirty" habitats. Although different surfaces display different micro and nano structures, the study from SEM has revealed that their superhydrophobicity is a result of surface roughness coated with epicuticular wax crystal, which has later been summarized as the complementary role of roughness and chemistry of the surface that give rise to the super-repelling effect. There exist controversies in what kind of roughness and chemistry is critical to produce their superhydrophobicity. For example, lotus leaves and water striders present hierarchical

structures, which was believed to be the vital factor [10], [11], while ramee leaves and Chinese watermelon are also superhydrophobic although they only have unitary structures without hierarchy. The necessity of a material's inherent hydrophobicity, on the other hand, has also been questioned since nature does not require very low surface energy material to produce superhydrophobicity, since low surface energy materials such as fluorocarbons does not exist in nature and have only been synthesized by human. In addition, some insects, such as springtails, have shown extreme wetting resistance to not only water but also some other low surface tension liquids (e.g., organic solvents). The nanostructures on their anti-adhesive skin have been revealed recently [12] and found to be coincided with the well-known hypothetical structure raised for boiling heat transfer during 1960s [13], [14]. Another category super repellent surfaces are those produce a specific liquid to repel other liquids, such as *Nepenthes* pitcher plant [15]. With micro and nano structures wetted by liquid (e.g., water from rain), the peristome surface becomes highly slippery. Understanding those findings from nature in the above manner guide our way to design a truly omniphobic surface.

5.1.2 Current Engineered Super-repellent Surfaces

5.1.2.1 Superhydrophobic and Superoleophobic Surfaces

Mimicking lotus leaves, superhydrophobic surfaces were developed by combining a microscale roughness with a low-energy coating so that the water on the surface asperities displays very large apparent contact angle ($\theta^* > 150^\circ$) with a very small roll-off angle ($\theta_{\text{rolloff}} < 10^\circ$) [1], [16], [17]. To further super-repel low energy liquids such as oils or organic solvents, a roughness with overhanging topology was necessary to make the

surface superoleophobic [18], [19] or so-called omniphobic [20] or superomniphobic [21], [22]. To realize roughness with microscale details, many different methods have been employed, including wet chemical reaction [23], dry chemical reaction [17], [20], electrochemical deposition [19], [21], [24], chemical vapor deposition [3], [25], laser machining [26], self-assembly sol-gel method [27], molding or nanoimprint lithography [22], [28], [29], etc., in which dry chemical reaction [18], [20], chemical vapor deposition (e.g., microbeads) and molding/nanoimprint lithography has been widely adopted to fabricate structures with overhangs.

5.1.2.2 Slippery Liquid-Infused Porous Surfaces (SLIPS)

Mimicking *Nepenthes* pitcher plant, SLIPS has been developed to repel liquids by a thin layer of lubricating liquid infused on the porous surface [6]. Because a liquid is used to repel another liquid, it requires three conditions for SLIPS to become repellent: first, the lubricating liquid should wick and be locked by the porosity of the surface which requires micro and nano structures; second, the lubricating liquid should be more wetting to the one to be repelled which requires the lubricating liquid to be with low surface tension and large density (so that it does not get propelled); third, the lubricating liquid should be immiscible to the liquid to be repelled. Because SLIPS is covered by a thin layer of liquid instead of solid, its repellent property is insensitive to the specific micro and nano structures underneath and the lubricating liquid help to self-repair the surface upon physical damage. Other advantages includes low contact angle hysteresis [6], high optical transparency [6], anti-ice [30], anti-biofouling [31], and tunable adhesion [32].

5.1.2.3 Smooth Perfluorinated Hybrid Surfaces

Mimicking SLIPS, lubricating fluid were replaced by loosely packed functional groups so that they can freely rotate and thus show liquid-like properties [33]. Similar to SLIPS, such surface is smooth and shows extreme low hysteresis to liquids in contact regardless of the magnitude of the static contact angles. Surfaces were prepared by a sol-gel reaction based on the co-hydrolysis and co-condensation a mixture of perfluoroalkylsilanes (FASX) and tetramethoxysilane (TMOS) [33], and thus called perfluorinated hybrid (FASX-hybrid) films. No degradation was found on their performance in dewetting even at high temperature ($\sim 250^\circ$) and submersion in various liquids (e.g., boiling water and weak acid).

5.1.3 Clarifying the Definition of Superomniphobicity

Despite the use of prefix omni- [6], [20]–[22], [28], however, no natural or man-made surface has been reported to repel liquids of extremely low surface tension/energy (i.e., $\gamma < 15 \text{ mJ/m}^2$), such as fluorinated solvents, which completely wet any existing material [14], [33]–[35]. We aim to overcome the limitation and obtain a truly superomniphobic surface, which super-repels all liquids without exception. To avoid the confusion with the sticking droplet with a large contact angle, e.g., the petal effect [36], it helps to first clarify that repelling means droplets not only bead up but also roll off on the surface. Following the definition of superhydrophobic surface, we define a superomniphobic surface to be a surface on which *all* liquids form very large apparent contact angle ($\theta^* > 150^\circ$) and roll off the surface with very small tilting angle ($\theta_{\text{rolloff}} < 10^\circ$).

Based on this definition, we found many some authors exaggerate their finding by using “omniphobic” or “superomniphobic” to describe sticking droplets and thus overstated the significance of their work [20], [21], [28]. We note those are the most confusing situation where a highly wetting (intrinsic contact angle $\theta_Y < 10^\circ$) liquid beading on a structured surface with $\theta^* > 90^\circ$, e.g., water on SiO_2 [18], [37] and hexane on nickel [21]. However, they are not considered to repel the liquid despite the large contact angle (usually at the advancing meniscus as explained in Chapter 3) due to the liquid sticking on the surface rather than rolling off, basically due to relatively low receding contact angles.

5.1.4 Our Design Philosophy Based on Current Limits

From the review above, we see that fluorinated solvent is the dead end of all existing approaches. This is understandable because fluorinated solvents pose similar chemistry to the best repellent materials, i.e., fluoro-polymers and perfluorinated liquids. Therefore, they highly wet *all* materials including fluoro-polymers and perfluorinated liquids, which are currently used to make form superhydrophobic/superoleophobic surfaces and perfluorinated liquid-infused/hybrid films, respectively. We reason that, if omniphobicity exists, the surface should be independent of the material from which it is constructed. In other words, the material’s inherent wettability, depicted by the intrinsic contact angle θ_Y , should be irrelevant, and thus repelling a completely wetting liquid ($\theta_Y = 0^\circ$), if possible, should be a pure physical (i.e., structural) matter, i.e., *roughness*.

5.2 Theory and Design

5.2.1 Requirements to Achieve Superomniphobicity

To repel (i.e., $\theta^* > 90^\circ$ with a small θ_{rolloff}) or super-repel ($\theta^* > 150^\circ$ with $\theta_{\text{rolloff}} < 10^\circ$) a wetting liquid (intrinsic contact angle $\theta_Y < 90^\circ$) on a structured surface, two conditions must be met: (1) a successful liquid suspension on the roughness and (2) a low liquid-solid contact. For a structured surface to repel a liquid, the microstructures should first be able to *suspend* the liquid – supporting a composite interface proposed by Cassie and Baxter [8]. Once suspended, decreasing the liquid-solid contact would increase the apparent contact angle and reduce the roll-off angle, hence increasing the repellency. We will analyze each condition in the following.

5.2.1.1 Liquid Suspension by Micro and Nano Structures

Liquid suspension by surface structures, or resisting liquid wetting by surface topologies with characteristic length smaller than the liquid's capillary length, has been proposed in 1960s considering θ_Y as a critical parameter [13], [14]. For $\theta_Y > 90^\circ$, such as water or aqueous solutions on a hydrophobic material, a simple microstructure (Figure 5-1a) would suspend the liquid to a Cassie state [1], [2], [13], [14], [16], [17]. For $\theta_Y < 90^\circ$, such as oils and organic solvents on a hydrophobic material or water on a slightly hydrophilic material, a re-entrant microstructure (Figure 5-1b) is required to suspend the liquid and resist it from wetting into the cavity [3], [13], [14], [18]–[22], [25], [28]. From simple force balance, the re-entrant topology of Figure 5-1(b) would suspend a liquid even with $\theta_Y \sim 0^\circ$ in the absence of any positive liquid pressure. However, there is always a pressure (e.g., hydrostatic, Laplace, environmental perturbation) in reality, and once

pushed into the cavity the liquid spreads spontaneously. So far, the most successful *suspension* was for liquids with surface energy as small as $\gamma \sim 15 \text{ mJ/m}^2$, i.e., pentane [20], [21] and isopentane [21], leaving many fluorinated solvents unaccounted for.

In addition to the re-entrant microstructure, it has long been hypothesized in the literature that surface structures of a doubly re-entrant topology (Figure 5-1c) might provide a stronger resistance against wetting and retain suspension even if $\theta_Y \sim 0^\circ$ [13], [14], [20], [38], [39]. The mechanism of suspending such a perfectly wetting liquid on a doubly re-entrant microstructure is reasoned as follows, using Figure 5-1(c). Upon contacting the surface, the liquid would wet the top surface and continue down along the sidewall of the vertical overhangs. The liquid would stop advancing at the bottom tip of the vertical overhangs, where the surface tension can start to point upwards. While this concept to suspend all liquids has been proposed [13], [14], [20], [38], [39] and recently confirmed by us with water [37], utilization of such topology to repel all liquids has never been reported. This is because a good doubly re-entrant structure like Figure 5-1(c) may *suspend* any liquid, but the resulting surface cannot *repel* the liquid unless the other requirement, i.e., a low liquid-solid contact fraction, is also satisfied. Although the trend may have been understood, the required degree of fraction has not been quantitatively appreciated. A highly wetting ($\theta_Y < 10^\circ$) liquid suspended on the microstructures would still spread (i.e., $\theta^* < 90^\circ$) on the composite surface unless the liquid rests mostly on air. A quantitative examination of the contribution of air will be given in Session 5.2.1.2. Here we continue our discussion on liquid suspension on more general microstructures comparing to Figure 5-1, which only depicts the ideal microstructures in each category.

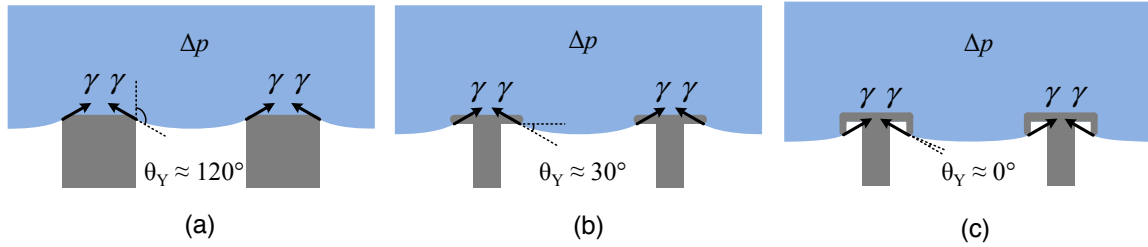


Figure 5-1 Liquid suspension on surface structures of three different topologies. (a) Simple structures require $\theta_Y > 90^\circ$ to suspend water. (b) Re-entrant structures allow $\theta_Y < 90^\circ$ to suspend oil or solvents as well. They would fail if $\theta_Y \sim 0^\circ$, as surface tension acts parallel to the horizontal overhangs with little vertical component to suspend the liquid. (c) Doubly re-entrant structures allow $\theta_Y \sim 0^\circ$ to suspend any liquid, as surface tension acts on the vertical overhangs with a significant vertical component. If the liquid-solid contact fraction is small enough, the surfaces would also repel the liquids, as we aim.

In general, due to the angle of their sidewalls, surface microstructures may be categorized as (a) simple structures with a positive downward slope (Figure 5-2a), (b) re-entrant structures with a negative downward slope (Figure 5-2b), and (c) doubly re-entrant structures with an upward slope (i.e., sidewall running back toward the top surface, Figure 5-2c). The angle of the structure's sidewall (with respect to the horizontal surface) α determines the theoretical range of intrinsic (Young's) contact angle θ_Y that allows liquid suspension. Figure 5-2(a) illustrates that many nonwetting liquids (i.e., $\theta_Y > 90^\circ$) can be suspended on a simple structure of $90^\circ \leq \alpha < \theta_Y$. The more wetting the liquid is (i.e., $\theta_Y \rightarrow 90^\circ$), the more vertical the sidewall should be (i.e., $\alpha \rightarrow 90^\circ$) to be able to suspend the liquid. Figure 5-2(b) illustrates that most liquids (i.e., $\theta_Y > 0^\circ$) can be suspended on a re-entrant structure of $0^\circ \leq \alpha < \theta_Y$. The more wetting the liquid is (i.e., $\theta_Y \rightarrow 0^\circ$), the more horizontal the sidewall should be (i.e., $\alpha \rightarrow 0^\circ$) to be able to suspend the liquid. Lastly, Figure 5-2(c) illustrates that all liquids (i.e., $\theta_Y \geq 0^\circ$) can be suspended on a doubly re-entrant structure of $-90^\circ \leq \alpha < 0^\circ \leq \theta_Y$. Since α is negative while θ_Y cannot be negative, any doubly re-entrant structure satisfies the suspension condition for any liquid.

In summary, re-entrant structures can suspend more types of liquids than simple structures, and doubly re-entrant structures can suspend even more types and in theory all liquids.

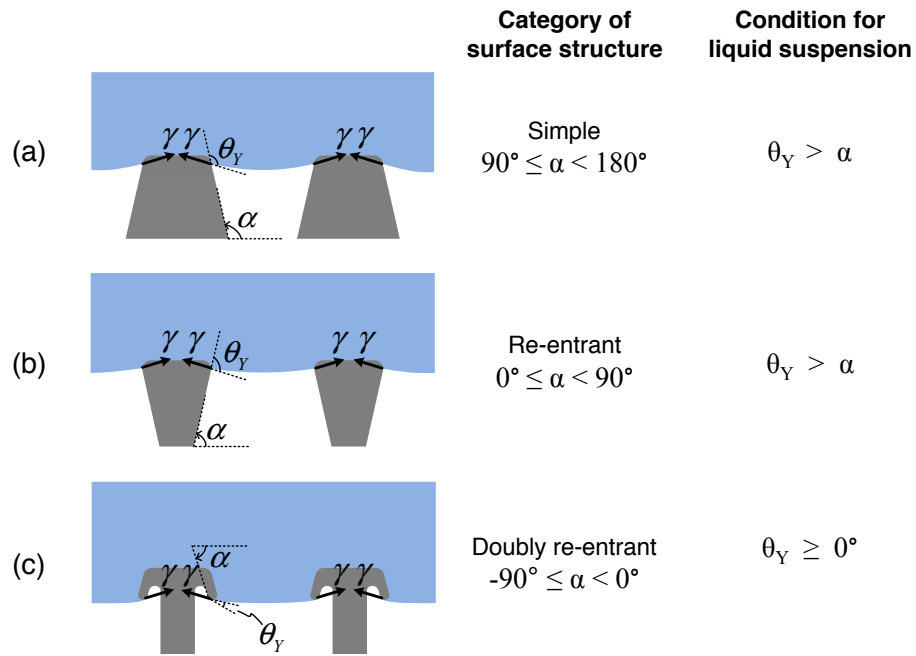


Figure 5-2 Relationship between intrinsic contact angle θ_Y and different surface structures for successful liquid suspension. (a) Microstructures with a simple sidewall (i.e., $90^\circ \leq \alpha < 180^\circ$) require Young's angle larger than the sidewall angle (i.e., $\theta_Y > \alpha$) in order to have an upward suspension force. (b) Microstructures with a re-entrant sidewall (i.e., $0^\circ \leq \alpha < 90^\circ$) also require Young's angle larger than the sidewall angle (i.e., $\theta_Y > \alpha$) to have an upward suspension force. (c) Microstructures with a doubly re-entrant sidewall (i.e., $-90^\circ \leq \alpha < 0^\circ$) always provide an upward suspension force and thus can theoretically suspend any, even perfectly wetting, liquid (i.e., $\theta_Y \geq 0^\circ$).

The minimum θ_Y of each structure category corresponds to a flat liquid-air interface, i.e., zero liquid pressure over the underlying air. In reality, a positive liquid pressure exists whether the liquid is in droplets (i.e., Laplace pressure) or completely covering the surface (i.e., hydrostatic pressure), requiring liquids with a higher θ_Y than the minimum angle for successful suspension. Since the minimum θ_Y decreases with decreasing α ,

structures with a smaller α (i.e., more vertical for simple structure and more horizontal for re-entrant structure) can suspend more types of liquids. Another useful interpretation is that the more wetting the liquid is, the less room the structures have in terms of α to accommodate the liquid pressure. Lastly, note that for Figure 5-2(c) the negative value of α can provide significant room to accommodate a liquid pressure even if $\theta_Y = 0^\circ$. Because the liquid pressure and environmental disturbances are inevitable in practice, only doubly re-entrant structures have a realistic chance to suspend perfectly wetting liquids.

5.2.1.2 Small Solid-Liquid Contact Fraction

To understand how far we are from being able to repel the highly wetting liquids, let us assess the contribution of air to the repellency. The apparent contact angle θ^* for a suspended droplet (i.e., in Cassie state) is described by the Cassie-Baxter model [8] as

$$\cos \theta^* = f_s \cos \theta_Y - f_g \quad (5.1)$$

where f_s is the liquid-solid contact fraction, or solid fraction for short, i.e., the proportion of liquid-solid contact area (including the wetted regions inside the roughness) to the projected area of the entire composite interface, and f_g is the gas fraction similarly defined for liquid-vapor interface and $f_s + f_g \geq 1^*$. If the liquid-solid and liquid-vapor interfaces are perfectly flat (i.e., neglecting any solid roughness and meniscus curvature), i.e., the ideal Cassie state with $f_s + f_g = 1$, Eq. 1 simplifies to

$$\cos \theta^* = f_s (1 + \cos \theta_Y) - 1 \quad (5.2)$$

* This general definition of f_s and f_g follows Cassie and Baxter's original paper, which included all the non-flat (e.g., rough, curved) effect on the liquid-solid and liquid-vapor interface. In addition to the most simplified version of flat liquid-solid and flat liquid-vapor interfaces, which results in $f_s + f_g = 1$, often adopted in the literature is a less simplified version of non-flat liquid-solid and flat liquid-vapor interfaces.

Although valid only for the ideal Cassie state, Eq. 5.2 allows us to qualitatively explore the relation between θ^* , f_s and θ_Y . In addition to the widely appreciated consequence that θ^* can be greatly increased as f_s decreases, we examine the role of the intrinsic contact angle θ_Y by plotting Eq. 5.2 with θ_Y as a parameter in Figure 5-3. It can be seen that the difference between the θ^* values of a large θ_Y and a small θ_Y decreases as f_s decreases. In other words, by minimizing f_s , the contribution of the material's inherent non-wettability (described by the magnitude of θ_Y) on the liquid repellency (described by the magnitude of θ^*) diminishes. This diminishing trend suggests that a structured surface may repel extremely wetting liquids if f_s is very small. For example, even a completely wetting liquid ($\theta_Y = 0^\circ$) may be super-repelled ($\theta^* > 150^\circ$) if $f_s < 6\%$. However, it should not be forgotten that this argument is valid only for the Cassie (i.e., suspended) state, which is exceedingly difficult to achieve if the solid fraction becomes very small. Even for the re-entrant topology of Fig. 1B, the suspension force becomes too small before f_s becomes small enough to repel liquids with very small θ_Y . This fact explains why super-repellency has been shown for liquids with surface tensions above ~ 20 mN/m [18] but not for those with 15-20 mN/m, i.e., pentane [20], [21] and isopentane [21], which have been suspended but not repelled.

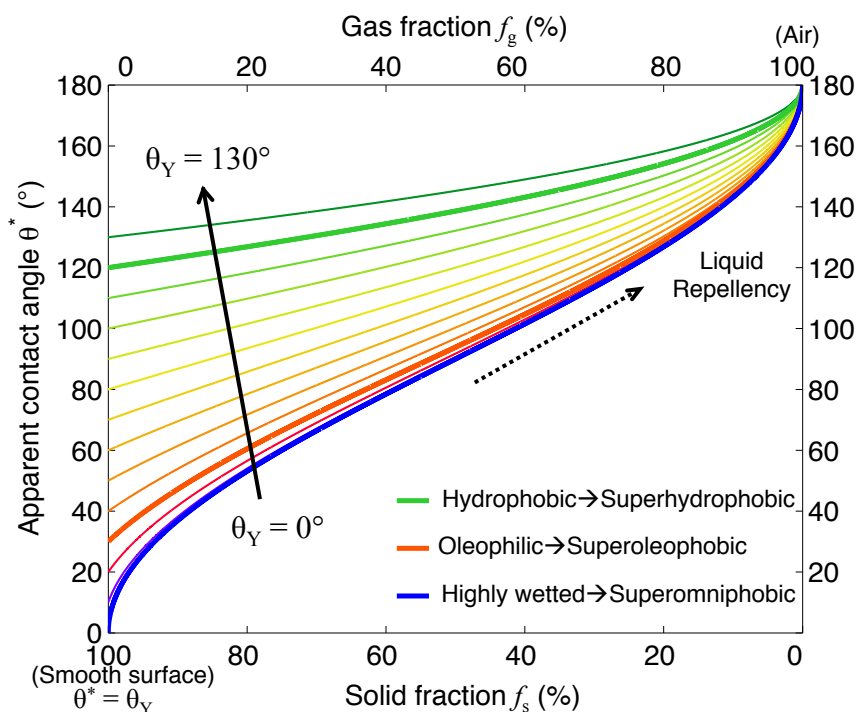


Figure 5-3 Relationship between apparent contact angle θ^* and solid fraction f_s for ideal Cassie state droplets with intrinsic contact angle θ_Y as a parameter. As f_s decreases, the band of lines narrows, indicating that the influence of θ_Y on θ^* diminishes. If f_s is below 6%, θ^* is above 150° even if $\theta_Y \sim 0^\circ$. However, this relationship is only for suspended liquids, i.e., in a Cassie state, which so far could be obtained for many but not all liquids. The greenish, reddish and bluish lines represent the inherent wettability: non-wetting (e.g., water on hydrophobic surface), moderately wetting (e.g., solvent on hydrophobic surface), and highly wetting (e.g., fluorinated solvents on any surface or most liquids on clean SiO_2), respectively. The three bold lines correspond to the three cases shown in Figure 5-1.

5.2.1.3 Key Geometries to Maximize Repellency

From Figure 5-1 and Figure 5-3, one can now reason that a structured surface may repel any liquid if the microstructures are doubly re-entrant and also of a low enough solid fraction. However, such a surface has never been achieved even though the doubly re-entrant topology has been proposed [13], [14], [20], [38], [39] and micro- and nano-fabrication have been available for decades. This is mainly because common doubly re-entrant shapes in the literature [13], [14], [20], [28], [39] produce only a weak suspension and a moderate solid fraction insufficient to repel highly wetting liquids. To suspend

extremely wetting liquids on a surface with a minimal solid fraction, an entire surface should be uniformly covered with doubly re-entrant structures having vertical overhangs as *thin*, *vertical*, and *short* as possible. Illustrated in Figure 5-1(c), such an ideal doubly re-entrant structure minimizes the break-in force by the liquid pressure to wet the cavity and maximizes the surface tension force that suspends the liquid against wetting [38]. Furthermore, the thin and vertical geometry of the overhangs minimizes their projected area added to the solid fraction, and the shortness of the overhang keeps the increase of the solid fraction by the vertical surfaces at bay. The above discussion of ideal doubly re-entrant structures reveals why so far no surface could repel completely wetting liquids or repel liquids on a highly wettable material. Some superhydrophobic or superoleophobic surfaces reported in the literature may partially fulfill the requirements but not all of them. Either only a few doubly re-entrant structures were formed among predominantly simple or re-entrant structures that are prone to wetting [3], [19], [25], or structures that are barely doubly re-entrant and have only a moderate solid fraction from a polymer replication of springtail skin's [28].

5.2.2 Surface Structure Design and Material Selection

To fulfill all the requirements reasoned above and quantified from Figure 5-3, we designed a surface illustrated in Figure 5-4: an array of doubly re-entrant structures consisting of microscale posts with nanoscale vertical overhangs. Posts were chosen over ridges or holes to minimize f_s more easily. Also, the post array allows the air underneath the droplet to always be connected to the atmosphere so that the liquid is suspended only by surface tension and not assisted by the pressure of the trapped air. We chose to form

the surface structures from silicon dioxide (SiO_2) for the following two reasons. First, a clean SiO_2 is highly wetted (i.e., $\theta_Y < 10^\circ$) by most liquids (except liquid metals like mercury) including water [1], [35]. Since roughening of a SiO_2 surface is supposed to amplify the liquid affinity to a complete wetting [1], structuring a SiO_2 surface to repel liquids should provide a stark contrast to the existing approach. Second, silicon (Si) micromachining provides sophisticated equipment and techniques to process SiO_2 .

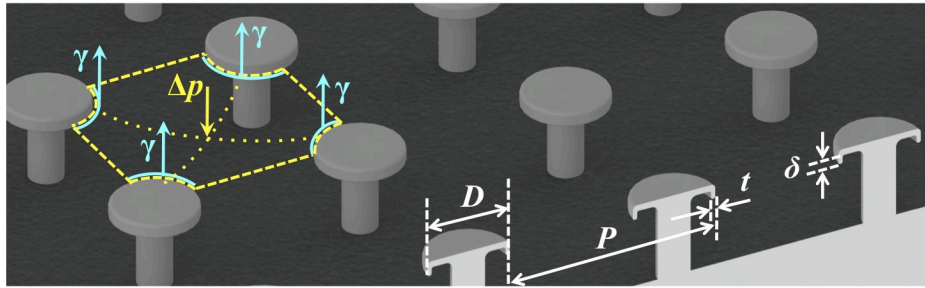


Figure 5-4 Designed surface of micro-posts with doubly re-entrant nano-overhangs. As key geometric parameters, D is the post top diameter, P is the center-to-center distance (i.e., pitch) between adjacent posts, and δ and t are the length and thickness of the vertical overhang. To make f_s small enough ($f_s \sim 6\%$) for our goal of super-repellency to all liquids, δ and t should be shrunk to extreme values.

5.3 Experiments

5.3.1 Fabrication

5.3.1.1 Fabrication Process of Structured Surfaces

We use Si micromachining to micro and nano structure repellent surfaces. To compare, we also fabricated two control surfaces, i.e., the other two liquid-repellent surfaces analyzed in Figure 5-1 for comparisons: a superhydrophobic surface consisting of cylindrical posts (Figure 5-1a) and a superoleophobic surface consisting of posts with re-entrant overhangs (Figure 5-1b), both of which were coated with a hydrophobic layer of

C₄F₈. In short, the main surface (i.e., doubly re-entrant posts) were fabricated by precisely controlled thermal oxidation of a shallow-etched silicon surface followed by three sequential etching steps on SiO₂ and Si to form doubly re-entrant structures. The control surfaces (i.e., vertical posts and re-entrant posts) were fabricated with a subset of process steps developed for the main surface (i.e., doubly re-entrant posts) but with an additional step of hydrophobic coating. The process flows are schematically illustrated in Figure 5-5.

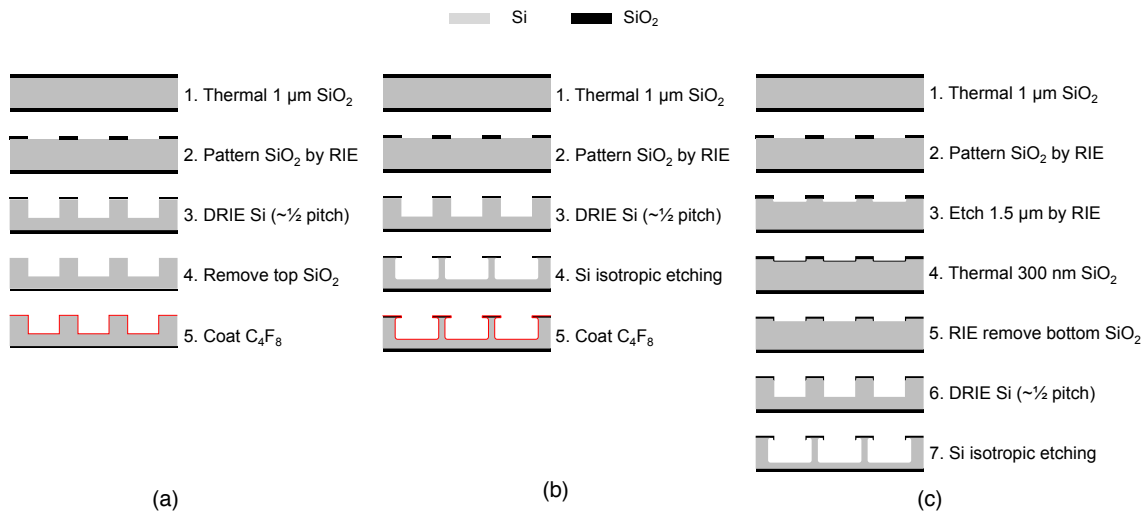


Figure 5-5 Process flow to fabricate (a) vertical, (b) re-entrant, and (c) doubly re-entrant posts

Vertical posts: Starting with thermally oxidized silicon wafers (prime grade, (100) type, 400-500 μm thick), SiO₂ (~ 1 μm thick) was first patterned by photolithography and reactive ion etching (RIE). Using SiO₂ as hard mask, Si was anisotropically etched (~ 50 μm deep) by deep reactive ion etching (DRIE) followed by a buffered oxide etch (BOE) bath to remove the top SiO₂ ensuring there is no re-entrant feature caused by the SiO₂ mask. A ~ 150 nm-thick C₄F₈ was then coated to form a superhydrophobic surface.

Re-entrant posts: Starting with thermally oxidized silicon wafers (prime grade, (100) type, 400-500 μm thick), SiO_2 ($\sim 1 \mu\text{m}$ thick) was first patterned by photolithography and RIE. Using SiO_2 as hard mask, Si was anisotropically etched ($\sim 50 \mu\text{m}$ deep) by DRIE. The re-entrant topology was then exposed by an isotropic Si etching (5-8 μm). A ~ 150 nm-thick C_4F_8 was coated afterwards to form a superoleophobic surface.

Doubly re-entrant posts: Starting with thermally oxidized silicon wafers (prime grade, (100) type, 400-500 μm thick), SiO_2 ($\sim 1 \mu\text{m}$ thick) was patterned by photolithography and RIE. Using SiO_2 as hard mask, a shallow silicon anisotropic etching ($\sim 1.3 \mu\text{m}$) and another shallow silicon isotropic etching (~ 200 nm) were performed both by RIE. Wafers were then cleaned and oxidized again to obtain the sidewall SiO_2 (~ 300 nm thick), which would later form the vertical overhangs. The SiO_2 at the bottom of the grooves was then removed by RIE without any mask, while the sidewall SiO_2 was protected by the initial thick SiO_2 and the recess created from the previous shallow silicon isotropic etching. The doubly re-entrant structures were finally exposed by isotropically etching silicon with RIE or XeF_2 . The surface was ready for test after a final cleaning with O_2 plasma, ALEG™ 380 bath (85°C for 20 minutes), hot Piranha bath ($\text{H}_2\text{SO}_4:\text{H}_2\text{O}_2 = 3:1$, 95°C for 5 minutes) and deionized water rinse to ensure a clean SiO_2 surface without any post-etch polymers and organics remained.

5.3.1.2 Process Conditions and Parameters

Thermal oxidation of Si: Silicon dioxide was obtained on silicon wafer using the standard wet oxide recipe at 1100°C (recipe name: WET1100.001) in Tystar's oxidation tube

located in UCLA's Nanoelectronics Research Facility (viz. Nanolab). Oxidation time to obtain ~1 μm and 300 nm thick thermal silicon dioxide were 3 hours 6 minutes and 21 minutes, respectively.

SiO₂ etching: Silicon dioxide was patterned by reactive ion etching (RIE) in STS MESC MULTIPLEX Advanced Oxide Etcher (AOE) using fluorine and oxygen chemistries. Silicon dioxide was etched by OXIDAPIC recipe, which uses CHF₃ (33 sccm), C₄F₈ (7 sccm), and Ar (10 sccm). The process pressure was set to 10 mTorr with 700 W inductively coupled plasma (ICP) power and 200 W RIE power. The etching rate was ~350 nm per minute. The etched silicon dioxide sidewall was slightly sloped with 91°-100° angle (i.e., α in Figure 5-2a).

Si etching: Silicon anisotropic and isotropic etching were performed in Oerlikon (Unaxis) SLR770 ICP machine. Silicon was etched by SF₆ with sidewall profile control by C₄F₈ polymer deposition. In anisotropic etching mode, a vertical smooth silicon sidewall was realized by 5-second polymer deposition for sidewall passivation (i.e., “Deposition”), 2-second top and bottom polymer removal (i.e., “Etch A” step), and 2-second silicon isotropic etching (i.e., “Etch B” step) with RF1 power set to 3 W, 9 W, 9 W, respectively. ICP power (i.e., RF2) and pressure were set to 825 W and 18 mTorr in all of the three steps. In isotropic etching mode, the “Deposition” and “Etch A” steps were removed, leaving only Etch B step for silicon etching.

C₄F₈ coating and characterization: Low-surface-energy C₄F₈ coating was deposited in Oerlikon (Unaxis) SLR770 ICP machine. Deposition was performed under 22 mTorr with C₄F₈ (70 sccm), SF₆ (0.5 sccm), and Ar (40 sccm). RIE power and ICP power were set to 1 W and 825 W, respectively. A 3-minute process deposited ~150 nm of C₄F₈ on a 4-inch bare silicon wafer, as measured by a profilometer (Detak 6M surface profile measuring system).

5.3.2 Liquids for Tests

To evaluate the liquid repellency of the fabricated surface, we chose fourteen different liquids (Table 5-1) including water, ionic liquid, acid, oils, and numerous polar or non-polar organic or fluorinated solvents with surface tensions ranging from 72.8 mN/m (i.e., water) to the lowest known value, 10 mN/m (i.e., FC-72). Those liquids are commonly used for applications such as electrochemistry, fuel cell, semiconductor industry, microfluidic systems, heat transfer, etc., and our measurement will provide direct references for applications across many disciplines.

Table 5-1 Physical and chemical properties of the tested liquids

Name	Chemical Formula	Surface tension (mN/m)	Viscosity (mPa·s)	Boiling point (°C)	Vapor pressure (Pa)	Density (kg/m ³)	Ref. Source	Chemical Source & Grade
FC-72 [*]	C ₆ F ₁₄	10 ²⁵	0.64 ²⁵	56	30900	1680 ²⁵	3M TM	Acros Organics
Novec 649 [†]	C ₆ F ₉ O	10.8 ²⁵	0.64 ²⁵	49	40360	1600 ²⁵	3M TM	3M TM , ≥ 99.79%
FC-84 [‡]	C ₇ F ₁₆	12 ²⁵	0.91 ²⁵	80	10600	1730 ²⁵	3M TM	Oakwood Chemical
Novec 7100 [§]	C ₄ F ₉ OCH ₃	13.6 ²⁵	0.58	61	26931	1520 ²⁵	3M TM	3M TM , ≥ 99.8%
FC-40 ^{**}	C ₂₁ F ₄₈ N ₂	16 ²⁵	4.1 ²⁵	165	287	1855 ²⁵	3M TM	Acros Organics
Hexane	C ₆ H ₁₄	18.4	0.3	68	17300	660.6	CRC	Sigma-Aldrich, ≥ 95%
2-Propanol	C ₃ H ₈ O	21.2	2.04	82	6020	780.9	CRC	KMG, ≥ 99.5%
Methanol	CH ₄ O	22.5	0.544	65	16900	791.4	CRC	KMG, ≥ 99.9%
Acetone	C ₃ H ₆ O	23.1	0.306	56	30800	784.5	CRC	KMG, ≥ 99.5%
Toluene	C ₇ H ₈	28.3	0.56	111	3790	866.8	CRC	Sigma-Aldrich, ≥ 99.8%
Formic acid	CH ₂ O ₂	38.0	1.607	101	5973	1223	CRC	Sigma-Aldrich, ≥ 95%
Ethylene glycol	C ₂ H ₆ O ₂	48.2	16.06	198	12.3	1113.5	CRC	Micromanipulator
[EMIM][BF ₄] ^{††}	C ₆ H ₁₁ BF ₄ N ₂	52.8	37	> 350	~0	1294 ²⁵	Fluka TM	Sigma-Aldrich, ≥ 99%
Water	H ₂ O	72.8	0.89	100	3169	997	CRC	UCLA Nanolab

Note: Properties are collected at 20°C unless otherwise specified as superscript.

5.3.3 Advancing and Receding Contact Angles

Advancing and receding contact angles were measured on an in-house built goniometer, which consists of an X-Y axis positioning stage amid observation instruments (GO[®] Edmund VZMTM 200i Zoom Imaging Lens with Point Grey FL3-U3-13Y3M-C CCD camera) and a light source (Stocker & Yale Imagelite Lite Mite Series Model 20) and sits on a vibration-isolation plate (Vistek VIP Series 320). A droplet (base diameter 1.5-2.0 mm) was created and held by a syringe (BD PrecisionGlide Needle, 22 G x 1.5 inch) on the test surface, which was placed on the positioning stage, so that an advancing and

* FC-72 is also called perfluorohexane or tetradecafluorohexane.

† Novec 649 is also called dodecafluoro-2-methylpentan-3-one.

‡ FC-84 is also called perfluoro-n-heptane.

§ Novec 7100 is also called methoxynonafluorobutane.

** FC-40 is a mixture of perfluoro-tri-n-butylamine and perfluoro-di-n-butylmethylamine.

†† [EMIM][BF₄] is also called 1-Ethyl-3-methylimidazolium tetrafluoroborate.

receding meniscus are formed at the two ends of the droplet by sliding the stage (~ 100 $\mu\text{m/s}$). All contact angles were measured from certain direction relative to the grid array of the posts so that the measurements are not affected by viewing directions. After capturing the entire ~ 15 - 20 seconds of sliding with the CCD camera at 80 frames per second (fps), the advancing and receding contact angles were calculated from the recorded images. For each image, the profile of the droplet was detected by Canny edge detection algorithm. After the advancing and receding menisci were defined from the detected profile, the pictures were scaled according to their capillary length, and the profiles near the contact points were fitted to quartic polynomial curves by the least squares method. The advancing and receding contact angles were then calculated from the slopes of the curves at the contact point.

5.3.4 Roll-off Angle Measurement

Roll-off angles were measured on an in-house built roll-off angle measurement system, where a goniometer is mounted on a tilting stage (OptoSigma 123-2730, accuracy $\pm 0.1^\circ$). The tilting stage is, in turn, mounted on a customized xyz-stage, which adjusts the test surface to tilt about the center axis of the goniometer view, so that it records a pure rotation. The stage was first leveled with a spirit level (Empire 991-9 torpedo level) attaining less than 0.2° initial tilting. A droplet (10 μL) was dispensed by a pipette (Eppendorf Research 0.5 - 10 μL) onto the test surface and aligned with the tilting axis of the stage. The stage was then tilted at a speed of ~ 0.5 - $1.8^\circ/\text{s}$ and stopped once the droplet start rolling on the surface. The roll-off angle was then read out from the goniometer.

5.3.5 Static and Dynamic Pressure Resistance

The static pressure resistance was measured by evaporating an FC-72 droplet on surfaces with doubly re-entrant SiO₂ posts. Utilizing the same optical setup for contact angle measurement (i.e., removing the syringe), the evolution of the evaporating droplet was recorded at 80 fps by a CCD camera (Point Grey FL3-U3-13Y3M-C). By analyzing the video frame by frame, the liquid droplet pressure is calculated from the droplet profile using the Laplace equation, a similar procedure we used to measure the surface tension of Galinstan[®] from a sessile drop [40]. The last frame before the droplet collapse and broke in the surface gave the maximum static pressure a doubly re-entrant posts surface could provide.

The dynamic liquid pressure was measured by free-falling droplet impacting onto the surface. Liquid droplets were released from a syringe (BD PrecisionGlide Needle, 30 G x 1 inch) using the same goniometer setup as the contact angle measurement. The droplet evolution was recorded at 6000 fps by a high-speed camera (Vision Research Phantom v7.2), which replaced the CCD camera.

5.3.6 High Temperature Stabilities

Two types of tests were performed to evaluate the stability of the superomniphobic SiO₂ surface at high temperatures. In a heat-treatment test, the structured SiO₂ surface was heated at 1100°C in a furnace (Tystar in UCLA's Nanoelectronics Research Facility) for ~ 1 hour with ~3 hours of ramping from and back to the idle temperature at 700°C. The apparent contact angle was then measured at room temperature. In a high-temperature repellency test, a droplet of an ionic liquid [EMIM][BF₄] was placed on the structured

SiO₂ surface kept on a hotplate at ~350°C. Ionic liquids are known to be stable at high temperatures and negligible evaporation (i.e., very low vapor pressure). The temperature of the hotplate (Cimarec[®] HP131225Q) was measured by a surface thermometer (PTC[®] 314C Dual Magnet Surface Thermometers) next to the test surface. The bimetallic sensor is shielded inside the surface thermometer and is in virtual thermal contact with the surface to be measured. Temperature of the test surface were measured by three different methods – the same surface thermometer, an infrared thermometer with adjustable emissivity (OMEGA[®] OS562), and a type K surface probe (OMEGA[®] SPHT-K-12-RA) – on a flat control surface made of the same material.

5.3.7 Visualization of Meniscus Location

To help verify our wetting theory on a doubly re-entrant structure, we dispensed a droplet of low viscosity epoxy (EpoThin[®] Resin No.20-8140 and EpoThin[®] Hardener No.20-8142 mixture, 100:39 by weight) on our surface with inclined doubly re-entrant structures (post diameter $D = 10 \mu\text{m}$, pitch $P = 50 \mu\text{m}$). The epoxy were cured after ~9 hours after when we inspected the sample under SEM to visualize the meniscus location.

5.3.8 Wetting Transition from Capillary Condensation

Although our surface was designed to repel all liquids by resisting their physical intrusion into the cavities, it has no defense against some other intrusion mechanisms such as condensation inside the cavity which is a common issue to all existing superhydrophobic and superoleophobic surfaces [1]. Because our surface is of SiO₂, a highly wettable material, we foresee the preference of capillary condensation to happen at the concave

corners. To confirm capillary condensation to be a mechanism that can cause wetting transition, we fabricated a control surface where the backside of the surface was opened so that condensation would be reduced by an increase of evaporation. This control surface required backside lithography and DRIE to etch through-hole between the posts as two additional steps to our fabrication process. Considering the capability of the machine in Nanolab at UCLA, the process flow was designed and confirmed to work as shown in Figure 5-6. Note that a $\sim 300 \mu\text{m}$ thick Si wafer was used so that the $1 \mu\text{m}$ -thick thermal SiO_2 was sufficient to serve the DRIE etch-through process (selectivity $\text{SiO}_2:\text{Si} = 1:300$ for recipe “Fast Nano DY” using FDRIE machine).

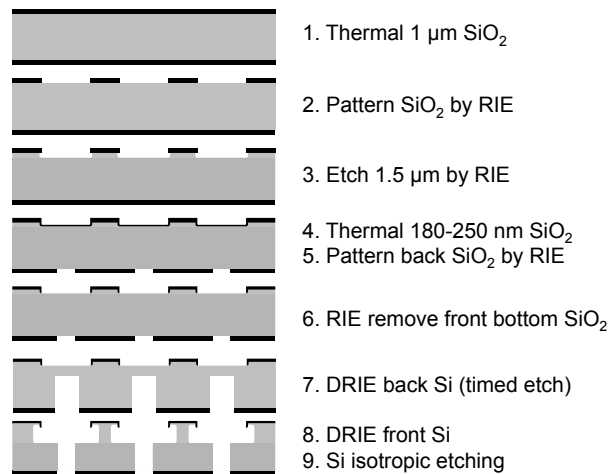


Figure 5-6 Process flow to fabricate doubly re-entrant posts with backside of the surface opened to atmosphere

5.4 Results and Discussion

5.4.1 Doubly Re-entrant SiO_2 Surfaces

We successfully fabricated a SiO_2 surface ($1.7 \text{ cm} \times 1.7 \text{ cm}$) with close-to-ideal doubly re-entrant structures (Figure 5-7). The inclined angle of the vertical overhang is measured

to be $\sim 85 \pm 1^\circ$ (Figure 5-7d), providing a maximum suspension force that is 99.6% of the perfectly vertical overhang shown in Figure 5-1(c). In spite of the overall resemblance between the micro-posts in Figure 5-7(a) and those of superoleophobic surfaces [18], [20]–[22], it is the close-to-ideal nanoscale vertical overhangs in Figure 5-7(b-d) that enable the striking liquid-repellency for this report.

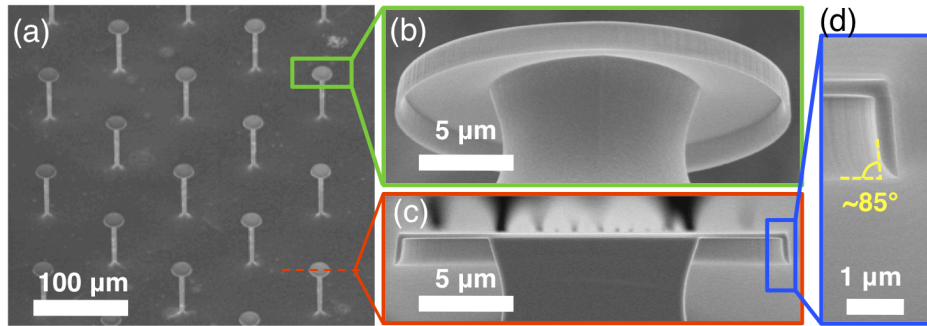


Figure 5-7 SEM micrographs of the fabricated doubly re-entrant SiO_2 surface. (a) Top angled view of the square-array of circular posts with post diameter $D \sim 20 \mu\text{m}$, pitch $P = 100 \mu\text{m}$, length of the doubly re-entrant structure $\delta \sim 1.5 \mu\text{m}$, and thickness of the doubly re-entrant structure $t \sim 300 \text{nm}$, resulting in solid fraction $f_s \sim 5\%$; (b) bottom angled view of one post; (c) cross-sectional view of one post, and (d) magnified cross-sectional view of the vertical overhang. Note the similarity with the ideal topology of Figure 5-1 (c).

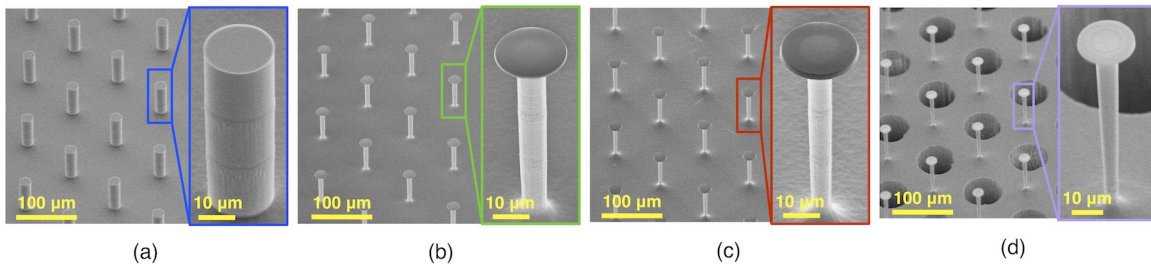


Figure 5-8 SEM micrographs of all fabricated structured surfaces. (a) Angled top view of the fabricated vertical posts structures before the final C_4F_8 coating. (b) Angled top view of the fabricated re-entrant posts structures before the final C_4F_8 coating. (c) Angled top view of the fabricated doubly re-entrant posts structures. (d) Angled top view of the fabricated doubly re-entrant posts structures with etch-through holes open the backside to atmosphere. Surfaces in (c) and (d) are thoroughly cleaned to ensure pure SiO_2 surface.

5.4.2 Liquids Beading on Superomniphobic SiO₂ Surface

Figure 5-9(a) shows three liquids (water, methanol, and FC-72) beading up as droplets on our structured SiO₂ surface. Although the droplets are of similar size, their shapes appear to be quite different; water appears the most spherical while FC-72 appears flattened. Such difference in overall appearance is dictated by the capillary length, $l_{\text{cap}} = (\gamma/\rho g)^{1/2}$, where γ is the surface tension of the liquid, ρ is density of the liquid, and g is gravitation acceleration. The capillary length of water, methanol and FC-72 are ~ 2.7 mm, ~ 1.7 mm, and ~ 0.78 mm, respectively. The water droplet with radius close to its capillary length appears spherical without much gravity effect, while the methanol and FC-72 droplets with radius larger than their respective capillary lengths appear flattened by gravity. Figure 5-9(b) shows snapshots of FC-72 ($\gamma = 10$ mN/m in air) being attached, advanced, receded and detached on our surface without wetting transition even with rough manual pumping. To quantify the repellency of our surface, we need to measure the advancing and receding contact angles and roll-off angles of all the fourteen liquids on the micro-posts with doubly re-entrant overhangs (Figure 5-1c, Figure 5-4, and Figure 5-7) made of SiO₂, which are presented in the following two sections.

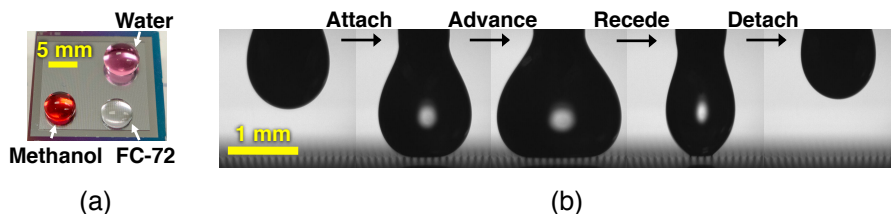


Figure 5-9 Liquids beading up as droplets on the superomniphobic SiO₂ surface. (a) The picture shows water (pink), methanol (red), and FC-72 (clear) droplets on the structured SiO₂ surface. Even though the apparent contact angles are similar for all three liquids, FC-72 is flattened most due to its smallest capillary length (~0.78 mm) among the three liquids. (b) Snapshots of an FC-72 droplet expanding and contracting on the SiO₂ surface of doubly re-entrant posts by a continuous pumping of the liquid in or out from a syringe. The light passing through the air between the microstructures indicates FC-72 has been successfully levitated to a Cassie state.

5.4.3 Apparent Advancing and Receding Contact Angles

Figure 5-10 shows our measured apparent advancing and receding contact angles on our structure SiO₂ surface. It also includes the other two liquid-repellent surfaces analyzed in Figure 5-1 for comparisons: a superhydrophobic surface consisting of cylindrical posts (Figure 5-1a and Figure 5-8a) and a superoleophobic surface consisting of posts with re-entrant overhangs (Figure 5-1b and Figure 5-8b), both of which were coated with a hydrophobic layer of C₄F₈. As expected, while the superhydrophobic surface with vertical posts was wetted by liquids with surface tension below ~40 mN/m, the superoleophobic surface with re-entrant posts repelled liquids with lower surface tension (20-40 mN/m). However, liquids with even lower surface tension (< 20 mN/m) could not be suspended as they wicked between the re-entrant posts. In contrast, on our surface with doubly re-entrant posts, all fourteen liquids formed large contact angles even without any hydrophobic coating. All contact angle measured are tabulated in Table 5-2.

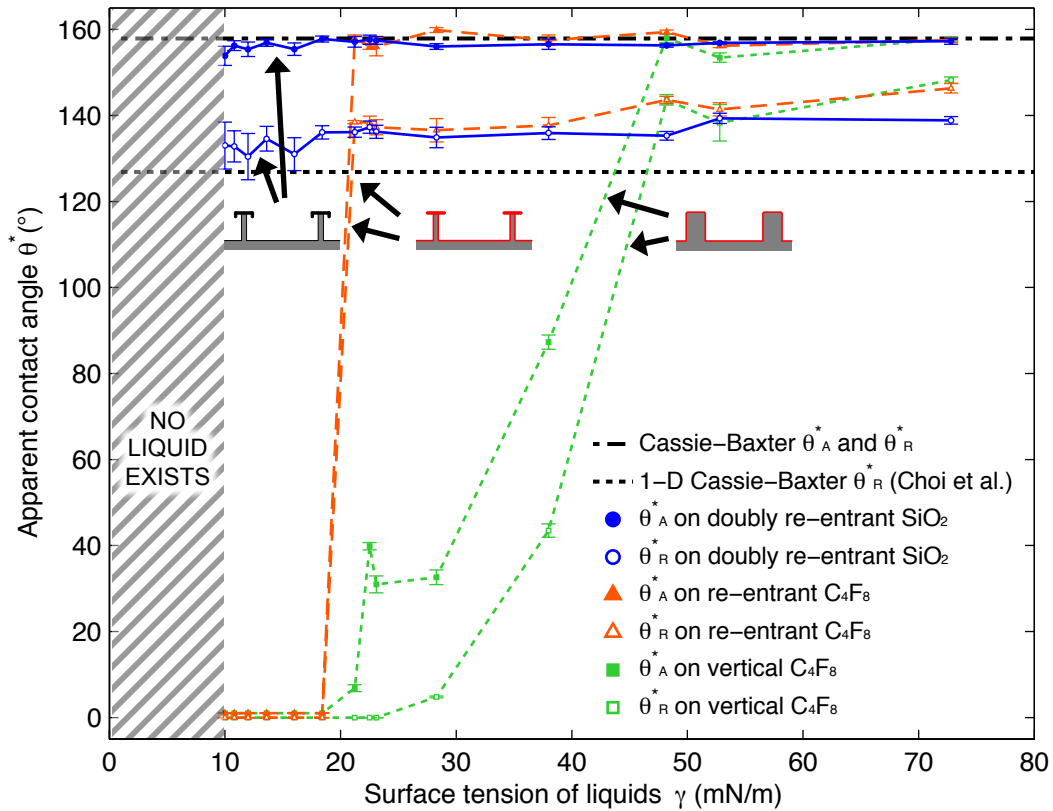


Figure 5-10 Apparent advancing and receding contact angles of the fourteen liquids measured on three liquid-repellent surfaces – our omniphobic surface and two control surfaces of the same nominal solid fraction ($f_s \sim 5\%$). Data on the omniphobic surface are depicted in blue circles (solid and hollow). Data on the control surface with re-entrant and vertical topologies are depicted in orange triangles and green squares, respectively. Data are compared with the theoretical models of advancing and receding contact angles. The classic Cassie-Baxter prediction of advancing and receding contact angles (Eqs. 5.3 & 5.4) are drawn by a black dash-dot line representing the nearly identical θ_A^* and θ_R^* . The receding contact angle predicted by the 1-D Cassie-Baxter model developed by Choi et al. [41] is drawn in a black dashed line. Theoretical predictions for the two control surfaces are nearly identical to that for the omniphobic SiO_2 surface and thus not drawn.

Table 5-2 Contact angles (°) of tested liquids measured on different smooth and structured surfaces in this report

Name	Surface Tension (mN/m)	θ on SiO ₂		θ on C ₄ F ₈		θ^* on doubly re-entrant SiO ₂		θ^* on re-entrant C ₄ F ₈		θ^* on vertical C ₄ F ₈	
		θ_A	θ_R	θ_A	θ_R	θ_A^*	θ_R^*	θ_A^*	θ_R^*	θ_A^*	θ_R^*
FC-72	10 ²⁵	< 10	< 10	< 10	< 10	153.8±2.2	133.0±5.4	0	0	0	0
Novec 649	10.8 ²⁵	< 10	< 10	< 10	< 10	156.2±1.1	132.8±3.6	0	0	0	0
FC-84	12 ²⁵	< 10	< 10	< 10	< 10	155.4±1.7	130.4±5.4	0	0	0	0
Novec 7100	13.6 ²⁵	< 10	< 10	< 10	< 10	156.9±0.8	134.6±2.9	0	0	0	0
FC-40	16 ²⁵	< 10	< 10	< 10	< 10	155.4±1.5	131.0±3.8	0	0	0	0
Hexane	18.4	< 10	< 10	20.3	< 10	157.8±0.7	136.1±1.6	0	0	0	0
2-Propanol	21.2	< 10	< 10	33.4	< 10	157.1±1.3	136.1±1.2	158.8±0.8	138.4±0.4	6.9±0.8	0
Methanol	22.5	< 10	< 10	49.7	32.3	157.6±1.1	137.3±1.4	156.1±0.7	138.3±1.5	39.8±0.9	0
Acetone	23.1	< 10	< 10	49.4	21.1	157.4±0.9	136.2±1.5	156.0±2.1	137.2±1.8	31.0±2.0	0
Toluene	28.3	< 10	< 10	41.8	27.3	156.0±0.7	134.9±2.4	159.9±0.5	136.6±2.7	32.6±1.7	4.8±0.2
Formic acid	38	< 10	< 10	78.6	58.3	156.5±1.2	135.9±1.5	157.5±1.2	137.6±1.9	87.3±1.6	43.5±1.6
Ethylene glycol	48.2	< 10	< 10	96.2	52.5	156.3±0.4	135.3±1.0	159.4±0.5	143.6±0.9	158.0±1.0	143.5±1.2
[EMIM][BF ₄]	52.8	< 10	< 10	96.3	72.9	156.9±0.2	139.3±1.2	156.2±0.4	141.4±1.5	153.4±1.1	138.3±4.2
Water	72.8	< 10	< 10	120.5	91.5	157.3±0.7	138.9±0.9	157.5±0.5	146.3±1.1	157.8±0.5	148.2±0.7

Note: Surface tensions are collected (from literature) at 20°C unless otherwise specified as superscript. All contact angles are measured at 20±1°C.

To compare with existing models, we rewrite some of the equations in Chapter 3 here.

The Cassie-Baxter model [8] directly relates the apparent advancing and receding contact angle on a rough surface (θ_A^* and θ_R^* , respectively) to the advancing and receding contact angle on a smooth surface (θ_A and θ_R , respectively), as

$$\cos\theta_A^* = f_s \cos\theta_A - f_g \quad (5.3)$$

$$\cos\theta_R^* = f_s \cos\theta_R - f_g \quad (5.4)$$

In Figure 5-10, we compare the experimental data with the Cassie-Baxter models.

Theoretical apparent contact angles are calculated with an assumption that the liquids

highly wet the smooth surface with $0^\circ \leq \theta_R < \theta_A < 10^\circ$. For our doubly re-entrant posts, the solid and gas fractions are calculated to be $f_s \approx 0.043$ and $f_g \approx 0.970$, respectively. The resulting theoretical predictions are the two nearly identical horizontal lines of $\sim 158^\circ$ for the advancing and receding cases of the Cassie-Baxter model.

Our measured advancing angle data agreed fairly well with the Cassie-Baxter model (Eq. S2), but the receding angle data deviated $\sim 20^\circ$ from the model (Eq. 5.4). Such $\sim 20^\circ$ contact angle hysteresis is commonly reported and among the smallest for structured surfaces composed of micro-posts (e.g., [18], [20], [21]). Such deviation at the receding ends has also been widely investigated by different researchers [22], [41]–[44]. The receding angle data of Figure 5-10 roughly agree with the 1-D Cassie-Baxter model [41]. Additional studies of comparing our experimental apparent contact angle data with all existing models or developing new models will be conducted in the future. As we explain in Chapter 3, the details of a receding contact line is much more complicated than the advancing due to the contact line distortion from pinning, which is much more profound particularly on our SiO₂ structures that are highly wetted.

We also notice that in Figure 5-10, while the contact angles of all tested liquids on the doubly re-entrant SiO₂ surface are similar and corroborate our theory (Figure 5-3), the data are more scattered for the liquids of small capillary length (i.e., fluorinate solvents). The scatter is due to the image analysis limited by the finite resolution of images, as explained with Figure 5-11. A liquid with a small capillary length (e.g., FC-72) forms a flatter droplet compared with one with a large capillary length (e.g., water), as shown in Figure 5-11(a), giving the flatter droplet an impression of a smaller contact angle, as shown in Figure 5-11(b). The limited resolution near the contact point makes the edge

detection algorithm truncate the wedge prematurely. A correct approach is to scale the images according to their capillary length, as shown in Figure 5-11(c), before analyzing the contact angles. Due to the finite resolution of a digital image, however, fewer points could be used to calculate contact angles of the flatter droplet, resulting in a more scattered data.

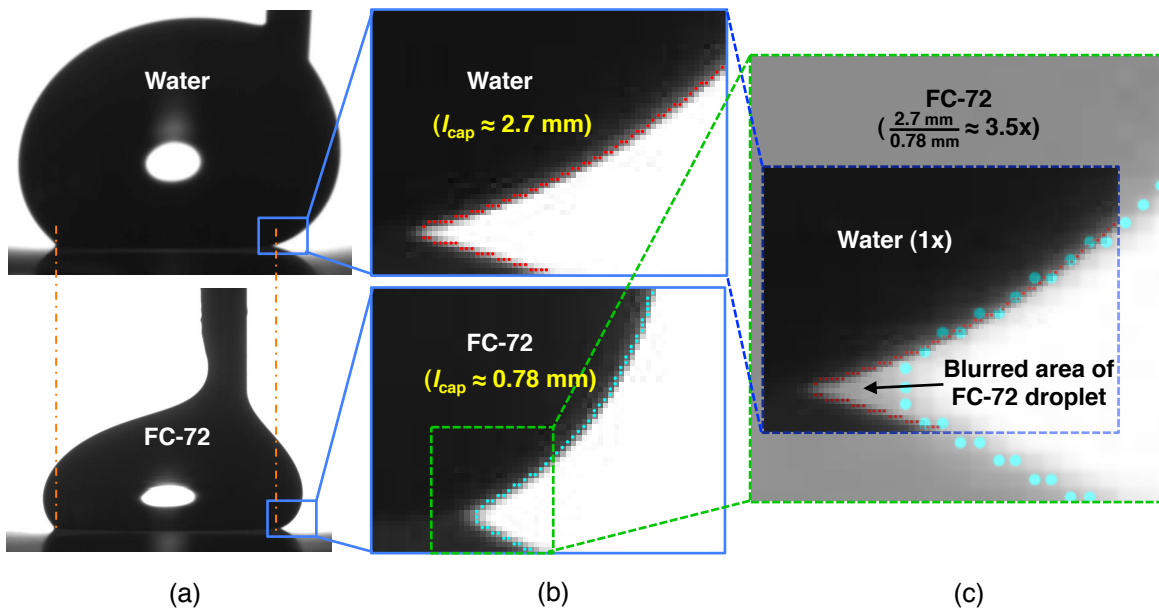


Figure 5-11 Illustration of why the contact-angle data of smaller-capillary-length liquids scatter more in Figure 5-10, using water and FC-72 droplets. (a) Water (capillary length $l_{cap} \approx 2.7 \text{ mm}$) and FC-72 (capillary length $l_{cap} \approx 0.78 \text{ mm}$) droplets of the same base diameter are flattened differently according to their capillary lengths. (b) The advancing menisci of water and FC-72 droplets, highlighted by the detected edge (red dots for water and cyan dots for FC-72), appear dissimilar due to their different capillary length. (c) After scaling the images according to their respective capillary lengths, the non-dimensionalized profiles overlap each other and allow for more consistent measurements of contact angles for different liquids. However, the menisci for FC-72 have fewer points (i.e., lower resolution) available for the contact-angle calculation, resulting in more scattered data.

The extent to which wettability is modulated by surface roughness, compared to the original material, is shown in Figure 5-12 where the apparent wettability (i.e., $\cos \theta^*$) is plotted as a function of the inherent wettability (i.e., $\cos \theta_V$). Data from our doubly re-

entrant posts surface (i.e., blue circles) were populated at the lower right corner in the fourth quadrant near point (1,-1), exhibiting the exceptional ability to render a highly wetting material highly non-wetting. In contrast, while the two control surfaces permit a Cassie state with non-wetting or partially wetting material, they got instantaneously soaked when the material was highly wetted by the liquids of very low surface tension (i.e., hexane and six fluorinated solvents), displaying $\theta^* \sim 0^\circ$ with data populated near point (1,1).

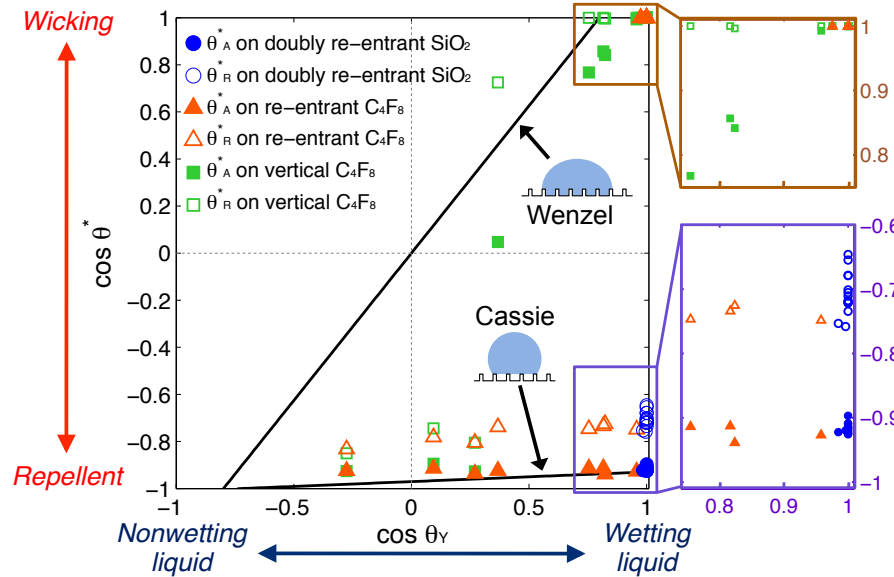


Figure 5-12 Relations of contact angles on smooth surface ($\cos \theta_\gamma$) and on a structured surface ($\cos \theta^*$). The theoretical relations from Wenzel and Cassie-Baxter models are plotted in solid black lines. Data near (1,-1) and (1,1) are shown in the zoomed-in boxes, revealing the difference between our structured SiO_2 surface with the control surfaces, especially when liquids highly wet the material.

5.4.4 Roll-off Angles

Our structured SiO₂ surface also shows very low roll-off angles ($\theta_{\text{rolloff}} < 10^\circ$ for a $\sim 10 \mu\text{L}$ droplet, $n = 3$) against all fourteen liquids tested, including fluorinate solvents, as shown in Figure 5-13.

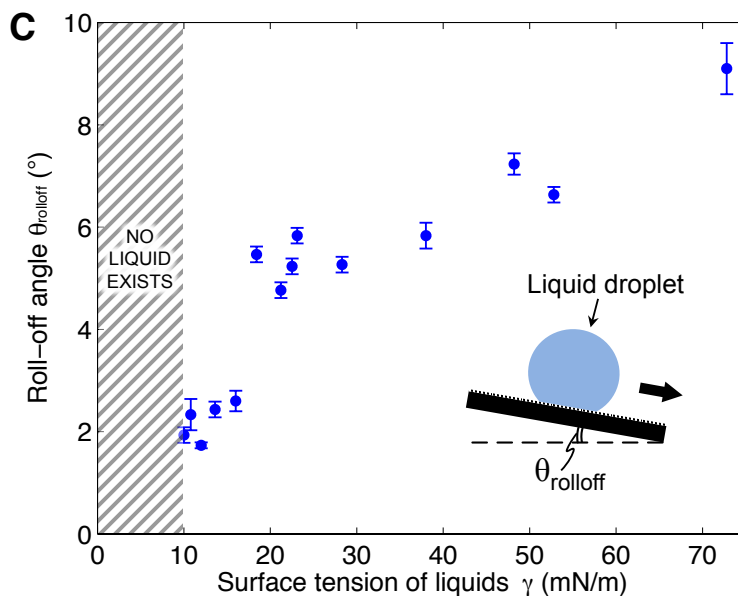


Figure 5-13 Roll-off angles of the fourteen liquids measured on the superomniphobic SiO₂ surface

5.4.5 Static Pressure Resistance: the Break-in Pressure

The break-in pressure, i.e., the maximum static pressure a structured repellent surface supplies without wetting transition, can be analyzed as follows. Within one unit of the square-grid posts, the force balance between surface tensional force and pressure force is depicted in Figure 5-4. Theoretically, doubly re-entrant structures with vertical overhangs (Figure 5-1c) provides the largest break-in (or breakthrough, impalement) pressure against wetting transition as

$$\Delta p_{\max} = \frac{\gamma \pi D'}{P^2 - \pi D'^2/4} \quad (5.5)$$

where γ is the liquid surface tension, D' is the diameter of the circular contact line at the bottom tip of the vertical overhang, Δp is the pressure difference across the liquid-vapor interface, P is the pitch of the posts. In our case, since the thickness of the vertical overhang t is much smaller than the post diameter D , $D' = D - 2t \approx D$. For FC-72 ($\gamma = 10$ mN/m), the theoretical break-in pressure is calculated to be 62.8 Pa on a doubly re-entrant posts surface with $D = 20 \mu\text{m}$, $P = 100 \mu\text{m}$, and $t = 300$ nm. This pressure is equivalent to the Laplace pressure of an FC-72 droplet of $\sim 318 \mu\text{m}$ in radius.

Figure 5-14(a) shows the snapshots of an evaporating FC-72 droplet, and Figure 5-14(b) illustrates the detailed changes in Laplace pressure and droplet base diameter during the evaporation. The pressure difference was calculated by the Young-Laplace equation as $\Delta p_{\text{droplet}} = 2\gamma/R_{\text{droplet}}$, where R_{droplet} is the radius of curvature at the apex of a droplet. The Laplace pressure built up as the droplet shrunk until the wetting occurs, after which FC-72 completely wets the surface (i.e., the last datum). The minimum droplet radius was measured to be $315.4 \pm 2.4 \mu\text{m}$, yielding the maximum pressure to be 63.4 ± 0.5 Pa, which showed great agreement with the theoretical values.

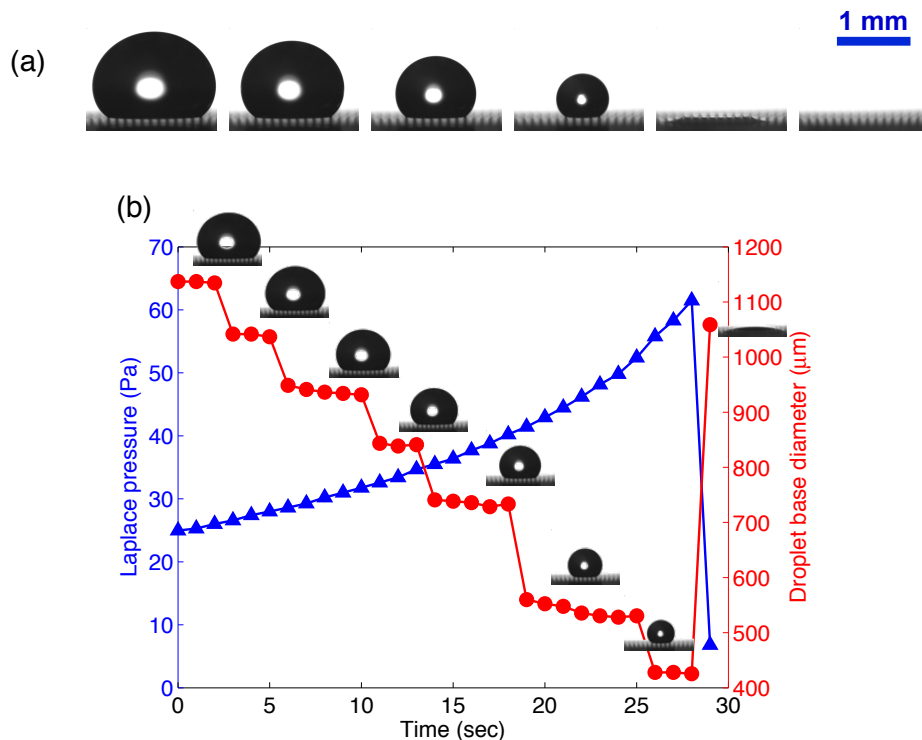


Figure 5-14 Break-in pressure measured from an evaporating FC-72 droplet. (a) Selected snapshots from video of an FC-72 droplet evaporating and subsequently shrinking on a SiO₂ surface of doubly re-entrant microstructures ($D \sim 20 \mu\text{m}$, $P = 100 \mu\text{m}$, and $t \sim 300 \text{nm}$). Wetting occurred between the fourth and fifth snapshots when the Laplace pressure inside the droplet overcame the maximum supporting force provided by surface tension via doubly re-entrant geometries. (b) Laplace pressure and base size of a droplet calculated from snapshots in (a). Insets are snapshots of the evaporating FC-72 droplet, which was suspended until it sat on 4 posts.

5.4.6 Dynamic Pressure Resistance: Droplet Rebounding

The doubly re-entrant structures allow droplets to bounce on even extremely sparse posts (i.e., tens of micrometers pitch and a low solid fraction $\sim 5\%$). With high-speed imaging, water, methanol and FC-72 droplets were confirmed to bounce off the truly superomniphobic SiO₂ surfaces (Figure 5-15). Water ($\gamma = 72.8 \text{ mN/m}$) and methanol ($\gamma = 22.5 \text{ mN/m}$) droplets rebounded on a surface with microposts of $100 \mu\text{m}$ pitch, which is much larger than those reported in the literature [3], [20]. However, FC-72 ($\gamma = 10 \text{ mN/m}$) droplets penetrated and wetted the above surface at impact. A new surface with

scaled-down structures was further prepared to reduce the pitch from 100 μm to 50 μm , which provided enough resistance against impalement and let FC-72 droplets rebound, as shown with snapshots in Figure 5-15(c).

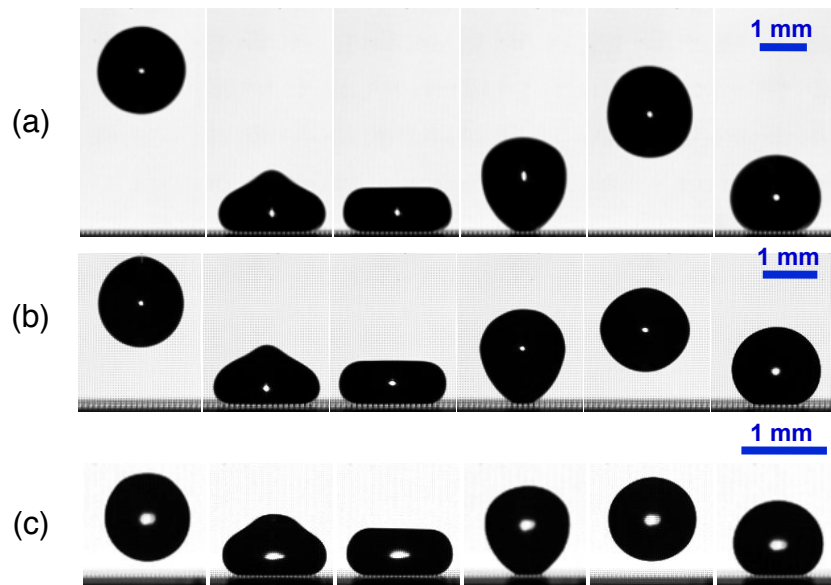


Figure 5-15 Robust repellency of the structured SiO_2 surface demonstrated by bouncing water, methanol, and FC-72 off the surface. (a) Water ($D = 20 \mu\text{m}$, $P = 100 \mu\text{m}$, $t = 300 \text{ nm}$, $f_s \approx 5\%$, Weber number $We \sim 0.70$). (b) Methanol ($D = 20 \mu\text{m}$, $P = 100 \mu\text{m}$, $t = 300 \text{ nm}$, $f_s \approx 5\%$, Weber number $We \sim 0.55$). (c) FC-72 ($D = 10 \mu\text{m}$, $P = 50 \mu\text{m}$, $\delta \sim 920 \text{ nm}$, $t = 270 \text{ nm}$, $f_s \approx 5\%$, Weber number $We \sim 0.42$).

5.4.7 High-temperature Superomniphobicity

Two types of tests were performed to evaluate the stability of the superomniphobic SiO_2 surface at high temperatures. In a heat-treatment test, the apparent contact angle showed no difference comparing with the surface before the thermal treatment, as summarized in Figure 5-10 and **Error! Reference source not found.**. The result confirms that the nanoscale features were not altered and the liquid repellency of the structured surfaces was stable even when subjected to very high temperatures, as high as 1100°C .

In a high-temperature repellency test, a droplet of an ionic liquid [EMIM][BF₄] was placed on the structured SiO₂ surface kept on a hotplate at ~350°C. The droplet stayed beaded and continued rolling on the heated surface, as shown in Figure 5-16. The advancing and receding contact angles were measured to be 149.9±4.5° and 134.3±5.2°. The roll-off angle has not been measured due to the difficulties in accurately tilting with the hotplate at such high temperature. Since the set temperature of the hotplate (~360°C) may be higher than the actual temperature, the temperature of the test surface were measured by three different methods on a flat control surface made of the same material (i.e., SiO₂) and found to be 347±8°C from the surface thermometer (PTC[®] 314C Dual Magnet Surface Thermometers), 330-360°C±7°C from the infrared thermometer (OMEGA[®] OS562) with emissivity 0.7-0.8, and 323±6°C from a type K surface probe (OMEGA[®] SPHT-K-12-RA). We conclude that this high-temperature repellency test was done at 320°C or higher.

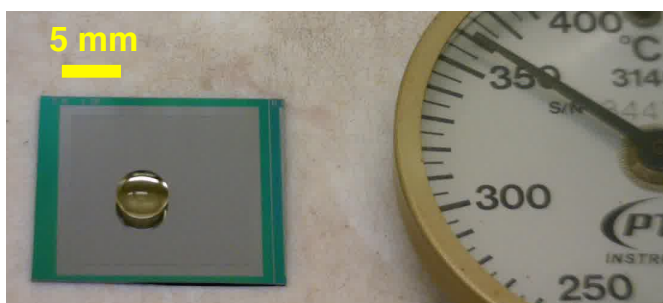


Figure 5-16 Super-repellency of the reported surfaces under very high temperature. A droplet of ionic liquid [EMIM][BF₄] beaded and rolled around, demonstrating a stable super-repellent state at above 320°C.

5.4.8 Visualization of Meniscus Location on Doubly Re-entrant Structures

As the surface suspends all known liquids in air, the epoxy fluid undoubtedly beaded up as a droplet and was gradually cured over 9 hours. Figure 5-17(a) shows the SEM micrograph of a cured epoxy ball on doubly re-entrant SiO_2 structures, and Figure 5-17(c) shows the same epoxy ball lifted up from the surface. The bottom of the ball is shown relatively flat. By comparing the posts on the field near the epoxy (Figure 5-17b) with a post beneath the epoxy ball (Figure 5-17d), it is shown that the meniscus was pinned at the bottom tip of the vertical overhang of the doubly re-entrant posts, confirming the wetting mechanism we reasoned in Session 5.2.1.1 (p. 78). The slit on the meniscus was probably created during separation of the epoxy ball from the surface.

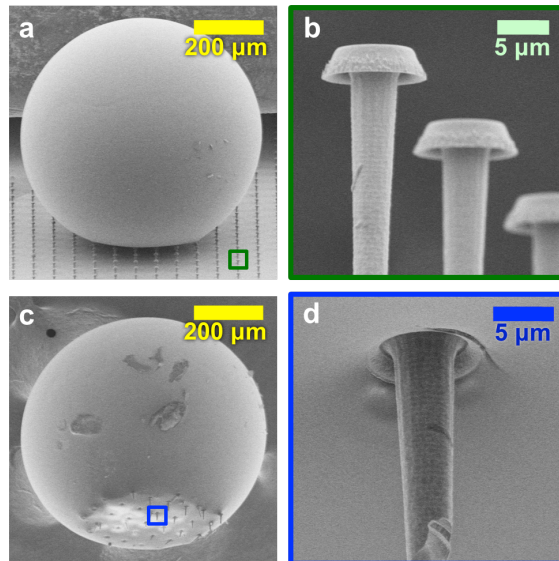


Figure 5-17 SEM images of an epoxy ball cured as a droplet on the doubly re-entrant posts. As the surface of doubly re-entrant structures is to repel all known liquids, the epoxy liquid undoubtedly beaded up as a droplet and was gradually cured over 9 hours. (a) Angled view of an epoxy ball cured on the structures. (b) Magnified image of doubly re-entrant posts in the vicinity of the epoxy ball. (c) The epoxy ball has been manually lifted up with a pair of tweezers. The bottom of the droplet appears flat and found to have taken up a couple of posts away from the structured surface. (d) Magnified image of one of the posts attached to the bottom of the epoxy ball.

5.4.9 Minimization of Capillary Condensation by Enhanced Evaporation

By opening the backside of the superomniphobic SiO₂ surface, we confirmed that the time before a wetting transition due to possible capillary condensation has been greatly expanded. For example, an FC-40 droplet could only bead on the surface for 0.5-1 second (without droplet movement such as sliding), while it was able to bead without wetting transition on a backside-opened superomniphobic SiO₂ surface/membrane for more than 15 seconds, which is 20 to 30 times improvement. It should be note that it is the nonvolatile low surface tension liquids such as FC-40 and FC-70 that suffer from capillary condensation. Because they evaporate slowly when comparing to other liquids, their condensate cannot be evaporated fast enough, especially inside the concave corners, and therefore cause wetting transition. Volatile liquids such as FC-72, FC-84 and many organic solvents do not present such problem probably because their condensed thin films evaporate fast so the concave corners of the doubly re-entrant structures are dry.

5.5 Summary and Applications

We schematically summary our finding in Figure 5-18, which illustrates that, provided a sufficiently low solid fraction, horizontal re-entrant structures can repel more types of liquids than vertical simple structures, and vertical doubly re-entrant structures can repel all liquids, leading to our design of Figure 5-1(c) and Figure 5-4. Providing the maximal suspension per projected area, the extreme topologies of Figure 5-1(c) and Figure 5-4 help minimize the solid fraction necessary for the suspension, thus maximizing the liquid repellency.

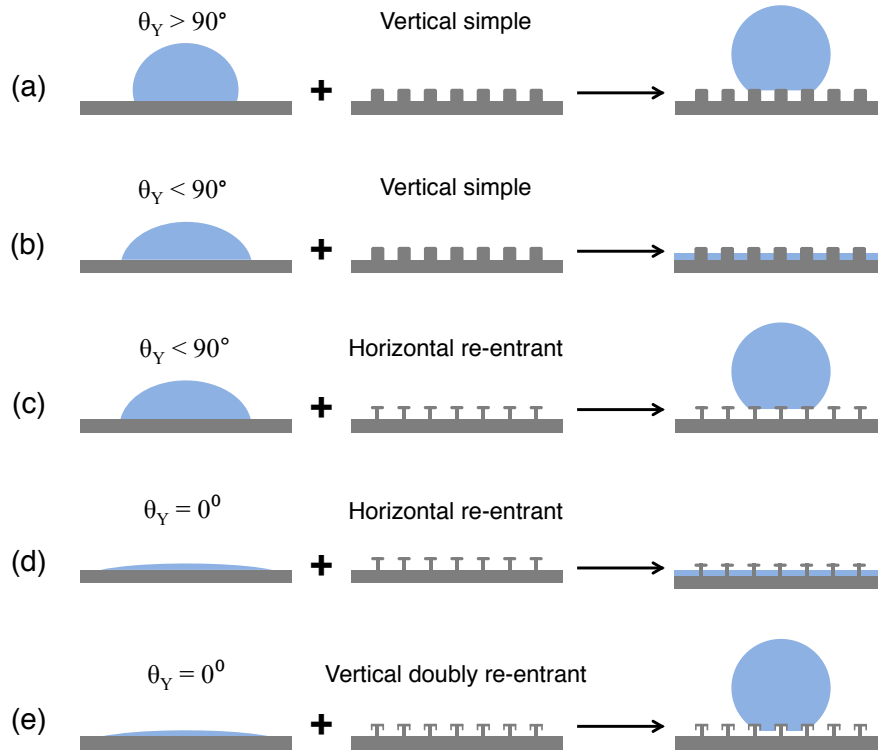


Figure 5-18 Summary of conditions to achieve liquid-repellent surfaces. (a) Vertical simple microstructures may suspend intrinsically nonwetting liquids ($\theta_Y > 90^\circ$). The suspension makes the structured surface more nonwetting and may render them super-nonwetting if solid fraction is low enough. (b) The structures in (a) are wetted by intrinsically wetting liquids ($\theta_Y < 90^\circ$). (c) Horizontal re-entrant microstructures may suspend intrinsically wetting liquids ($\theta_Y < 90^\circ$). The suspension makes the structured surface less wetting and may render them nonwetting or super-nonwetting if solid fraction is low enough. (d) The structures in (c) are wetted by perfectly wetting liquids ($\theta_Y = 0^\circ$). (e) Vertical doubly re-entrant microstructures (this report) may suspend all liquids including the perfectly wetting liquids ($\theta_Y = 0^\circ$). The suspension makes the structured surfaces less wetting and may render them nonwetting or super-nonwetting if solid fraction is low enough.

Proven super-repellent to all liquids without any coating, our superomniphobic SiO_2 surface offers to solve many existing problems and invite new applications. Taking electronic thermal management as an example, the ability to repel fluorinated solvents may allow the surface to be cooled by nucleate boiling (i.e., the most efficient mode of cooling) for supercomputers [45]. Free of polymeric coating, the developed surface is expected to greatly widen the application range of superhydrophobic surfaces as we

confirmed the surface is unaltered after a storage at $> 1000^{\circ}\text{C}$ and demonstrated rolling off of a non-volatile liquid in an environment at $> 320^{\circ}\text{C}$. The ability to stay dry at high temperatures, e.g., in steam environment, is expected to slow corrosion and extend the service life of parts in chemical or power plants, solar cells, and cooking wares, etc. The polymer-free parts are expected to last longer in outdoor environment, e.g., automobiles, aerospace, and buildings, where polymeric materials tend to degrade faster by unfavorable conditions, e.g., ultraviolet radiation. The reduced production of polyfluorinated compounds is also favorable for environmental and potential human health issues [45]. Although demonstrated with surface microstructure of posts and material of SiO_2 here, omniphobic surfaces should be able to be extended to other structures (ridges, honeycomb, etc.) and materials (metals, ceramics, polymers) depending on specific applications.

5.6 References

- [1] D. Quéré, “Non-sticking drops,” *Rep. Prog. Phys.*, vol. 68, no. 11, p. 2495, 2005.
- [2] W. Barthlott and C. Neinhuis, “Purity of the sacred lotus, or escape from contamination in biological surfaces,” *Planta*, vol. 202, no. 1, pp. 1–8, 1997.
- [3] X. Deng, L. Mammen, H.-J. Butt, and D. Vollmer, “Candle Soot as a Template for a Transparent Robust Superamphiphobic Coating,” *Science*, vol. 335, no. 6064, pp. 67–70, 2012.
- [4] A. R. Betz, J. Xu, H. Qiu, and D. Attinger, “Do surfaces with mixed hydrophilic and hydrophobic areas enhance pool boiling?,” *Appl. Phys. Lett.*, vol. 97, no. 14, pp. 141909–141909, 2010.
- [5] C. Lee and C.-J. Kim, “Underwater restoration and retention of gases on superhydrophobic surfaces for drag reduction,” *Phys. Rev. Lett.*, vol. 106, no. 1, p. 014502, 2011.

- [6] T.-S. Wong, S. H. Kang, S. K. Tang, E. J. Smythe, B. D. Hatton, A. Grinthal, and J. Aizenberg, “Bioinspired self-repairing slippery surfaces with pressure-stable omniphobicity,” *Nature*, vol. 477, no. 7365, pp. 443–447, 2011.
- [7] R. N. Wenzel, “Resistance of solid surfaces to wetting by water,” *Ind. Eng. Chem.*, vol. 28, no. 8, pp. 988–994, 1936.
- [8] A. Cassie and S. Baxter, “Wettability of porous surfaces,” *Trans. Faraday Soc.*, vol. 40, pp. 546–551, 1944.
- [9] F. E. Bartell and J. W. Shepard, “Surface Roughness as Related to Hysteresis of Contact Angles. 1. The System Paraffin Water Air,” *J. Phys. Chem.*, vol. 57, no. 2, pp. 211–215, 1953.
- [10] L. Gao and T. J. McCarthy, “The ‘lotus effect’ explained: two reasons why two length scales of topography are important,” *Langmuir*, vol. 22, no. 7, pp. 2966–2967, 2006.
- [11] Y. Su, B. Ji, K. Zhang, H. Gao, Y. Huang, and K. Hwang, “Nano to micro structural hierarchy is crucial for stable superhydrophobic and water-repellent surfaces,” *Langmuir*, vol. 26, no. 7, pp. 4984–4989, 2010.
- [12] R. Helbig, J. Nickerl, C. Neinhuis, and C. Werner, “Smart skin patterns protect springtails,” *PloS One*, vol. 6, no. 9, p. e25105, 2011.
- [13] R. L. Webb, “The evolution of enhanced surface geometries for nucleate boiling,” *Heat Transf. Eng.*, vol. 2, no. 3–4, pp. 46–69, 1981.
- [14] V. P. Carey, *Liquid-vapor phase-change phenomena*. New York: Taylor & Francis Group. LLC, 2008.
- [15] H. F. Bohn and W. Federle, “Insect aquaplaning: Nepenthes pitcher plants capture prey with the peristome, a fully wettable water-lubricated anisotropic surface,” *Proc. Natl. Acad. Sci. U. S. A.*, vol. 101, no. 39, pp. 14138–14143, Sep. 2004.
- [16] T. Onda, S. Shibuichi, N. Satoh, and K. Tsujii, “Super-Water-Repellent Fractal Surfaces,” *Langmuir*, vol. 12, no. 9, pp. 2125–2127, 1996.
- [17] C.-H. Choi and C.-J. Kim, “Large slip of aqueous liquid flow over a nanoengineered superhydrophobic surface,” *Phys. Rev. Lett.*, vol. 96, no. 6, p. 066001, 2006.
- [18] A. Tuteja, W. Choi, M. Ma, J. M. Mabry, S. A. Mazzella, G. C. Rutledge, G. H. McKinley, and R. E. Cohen, “Designing superoleophobic surfaces,” *Science*, vol. 318, no. 5856, pp. 1618–1622, 2007.
- [19] A. K. Kota, Y. Li, J. M. Mabry, and A. Tuteja, “Hierarchically Structured Superoleophobic Surfaces with Ultralow Contact Angle Hysteresis,” *Adv. Mater.*, vol. 24, no. 43, pp. 5838–5843, 2012.

- [20] A. Tuteja, W. Choi, J. M. Mabry, G. H. McKinley, and R. E. Cohen, “Robust omniphobic surfaces,” *Proc. Natl. Acad. Sci.*, vol. 105, no. 47, pp. 18200–18205, 2008.
- [21] A. Grigoryev, I. Tokarev, K. G. Kornev, I. Luzinov, and S. Minko, “Superomniphobic magnetic microtextures with remote wetting control,” *J. Am. Chem. Soc.*, vol. 134, no. 31, pp. 12916–12919, 2012.
- [22] R. Dufour, M. Harnois, Y. Coffinier, V. Thomy, R. Boukherroub, and V. Senez, “Engineering sticky superomniphobic surfaces on transparent and flexible PDMS substrate,” *Langmuir*, vol. 26, no. 22, pp. 17242–17247, 2010.
- [23] S. Wang, L. Feng, and L. Jiang, “One-Step Solution-Immersion Process for the Fabrication of Stable Bionic Superhydrophobic Surfaces,” *Adv. Mater.*, vol. 18, no. 6, pp. 767–770, 2006.
- [24] M.-F. Wang, N. Raghunathan, and B. Ziaie, “A Nonlithographic Top-Down Electrochemical Approach for Creating Hierarchical (Micro–Nano) Superhydrophobic Silicon Surfaces,” *Langmuir*, vol. 23, no. 5, pp. 2300–2303, Feb. 2007.
- [25] Y. Ma, X. Cao, X. Feng, Y. Ma, and H. Zou, “Fabrication of super-hydrophobic film from PMMA with intrinsic water contact angle below 90°,” *Polymer*, vol. 48, no. 26, pp. 7455–7460, 2007.
- [26] T. Baldacchini, J. E. Carey, M. Zhou, and E. Mazur, “Superhydrophobic surfaces prepared by microstructuring of silicon using a femtosecond laser,” *Langmuir*, vol. 22, no. 11, pp. 4917–4919, 2006.
- [27] J. Wang, Y. Wen, J. Hu, Y. Song, and L. Jiang, “Fine Control of the Wettability Transition Temperature of Colloidal-Crystal Films: From Superhydrophilic to Superhydrophobic,” *Adv. Funct. Mater.*, vol. 17, no. 2, pp. 219–225, Jan. 2007.
- [28] R. Hensel, R. Helbig, S. Aland, A. Voigt, C. Neinhuis, and C. Werner, “Tunable nano-replication to explore the omniphobic characteristics of springtail skin,” *NPG Asia Mater.*, vol. 5, no. 2, p. e37, 2013.
- [29] H.-J. Choi, S. Choo, J.-H. Shin, K.-I. Kim, and H. Lee, “Fabrication of Superhydrophobic and Oleophobic Surfaces with Overhang Structure by Reverse Nanoimprint Lithography,” *J. Phys. Chem. C*, vol. 117, no. 46, pp. 24354–24359, Nov. 2013.
- [30] P. Kim, T.-S. Wong, J. Alvarenga, M. J. Kreder, W. E. Adorno-Martinez, and J. Aizenberg, “Liquid-infused nanostructured surfaces with extreme anti-ice and anti-frost performance,” *ACS Nano*, vol. 6, no. 8, pp. 6569–6577, 2012.

- [31] A. K. Epstein, T.-S. Wong, R. A. Belisle, E. M. Boggs, and J. Aizenberg, “Liquid-infused structured surfaces with exceptional anti-biofouling performance,” *Proc. Natl. Acad. Sci.*, vol. 109, no. 33, pp. 13182–13187, 2012.
- [32] X. Yao, Y. Hu, A. Grinthal, T.-S. Wong, L. Mahadevan, and J. Aizenberg, “Adaptive fluid-infused porous films with tunable transparency and wettability,” *Nat. Mater.*, vol. 12, no. 6, pp. 529–534, 2013.
- [33] C. Urata, B. Masheder, D. F. Cheng, and A. Hozumi, “Unusual Dynamic Dewetting Behavior of Smooth Perfluorinated Hybrid Films: Potential Advantages over Conventional Textured and Liquid-Infused Perfluorinated Surfaces,” *Langmuir*, vol. 29, no. 40, pp. 12472–12482, 2013.
- [34] D. Brutin, Z. Zhu, O. Rahli, J. Xie, Q. Liu, and L. Tadrist, “Sessile drop in microgravity: creation, contact angle and interface,” *Microgravity Sci. Technol.*, vol. 21, no. 1, pp. 67–76, 2009.
- [35] D. Janssen, R. De Palma, S. Verlaak, P. Heremans, and W. Dehaen, “Static solvent contact angle measurements, surface free energy and wettability determination of various self-assembled monolayers on silicon dioxide,” *Thin Solid Films*, vol. 515, no. 4, pp. 1433–1438, 2006.
- [36] L. Feng, Y. Zhang, J. Xi, Y. Zhu, N. Wang, F. Xia, and L. Jiang, “Petal effect: a superhydrophobic state with high adhesive force,” *Langmuir*, vol. 24, no. 8, pp. 4114–4119, 2008.
- [37] T. Liu and C.-J. Kim, “Microstructured SiO₂ surface repellent to liquids without coating,” in *Proc. Int. Conf. Solid State Sensors, Actuators and Microsystems (Transducers '13)*, 2013.
- [38] C.-J. Kim, “Structured Surfaces for Enhanced Nucleate Boiling,” MS thesis, Iowa State University, 1985.
- [39] R. Hensel, R. Helbig, S. Aland, H.-G. Braun, A. Voigt, C. Neinhuis, and C. Werner, “Wetting Resistance at Its Topographical Limit: The Benefit of Mushroom and Serif T Structures,” *Langmuir*, vol. 29, no. 4, pp. 1110–1112, 2013.
- [40] T. Liu, P. Sen, and C.-J. Kim, “Characterization of nontoxic liquid-metal alloy galinstan for applications in microdevices,” *J. Microelectromechanical Syst.*, vol. 21, no. 2, pp. 443–450, 2012.
- [41] W. Choi, A. Tuteja, J. M. Mabry, R. E. Cohen, and G. H. McKinley, “A modified Cassie-Baxter relationship to explain contact angle hysteresis and anisotropy on non-wetting textured surfaces,” *J. Colloid Interface Sci.*, vol. 339, no. 1, pp. 208–216, 2009.
- [42] M. Reyssat and D. Quéré, “Contact Angle Hysteresis Generated by Strong Dilute Defects,” *J. Phys. Chem. B*, vol. 113, no. 12, pp. 3906–3909, 2009.

- [43] R. Raj, R. Enright, Y. Zhu, S. Adera, and E. N. Wang, “Unified Model for Contact Angle Hysteresis on Heterogeneous and Superhydrophobic Surfaces,” *Langmuir*, vol. 28, no. 45, pp. 15777–15788, 2012.
- [44] P. Papadopoulos, L. Mammen, X. Deng, D. Vollmer, and H.-J. Butt, “How superhydrophobicity breaks down,” *Proc. Natl. Acad. Sci.*, vol. 110, no. 9, pp. 3254–3258, 2013.
- [45] A. B. Lindstrom, M. J. Strynar, and E. L. Libelo, “Polyfluorinated compounds: past, present, and future,” *Environ. Sci. Technol.*, vol. 45, no. 19, pp. 7954–7961, 2011.

Chapter 6 Artificial Cavities to Enhance Nucleate Boiling of Refrigerants

6.1 Introduction

6.1.1 Boiling Heat Transfer for Thermal Management

Heat transfer with phase changes is the most efficient mode of heat transfer and anticipated to satisfy some of the most challenging needs of cooling in modern engineering, such as the power dissipation issues of integrated electronics [1]. Unlike evaporation, which is also a phase change process, boiling involves creation of new liquid-vapor interfaces, i.e., meniscus, at discrete sites on a heated surface [2]. Among the entire boiling regimes, nucleate boiling, where vapor bubbles are generated and released from a heated surface, is the most efficient [2]; therefore much effort has been put to enhance boiling heat transfer in two aspects: increasing the heat transfer coefficient (HTC), i.e., the thermodynamic efficiency of the boiling exchange, and increasing the critical heat flux (CHF), i.e., the limit beyond which HTC drastically reduces because liquid dries out on the heated surface. Since practical nucleate boiling takes place between a liquid and a solid, scientists have been trying to improve nucleate boiling from those two aspects. Changes to the liquids include mixing it with another liquid [3] or adding some additives, e.g., nanoparticles [4] or surfactants [5]. Modification to solid surfaces has been devoted to surface micro and nano structures and surface chemistry to promote and sustain the nucleation [6]–[9].

6.1.2 Challenges in using Refrigerants for Boiling Heat Transfer

While found effective for water and some solvents, boiling enhancement with surface micro and nanostructures has not been valid for refrigerants and dielectric fluorocarbon liquids (e.g., FC liquids from 3M™), which are the typical coolants for immersion cooling of electronics. Having distinctively low surface tensions, those liquids wet all materials, no matter they are hydrophilic or hydrophobic, and thus flood all the microcavities on a surface, expelling all vapor needed to start the nucleation. Therefore, boiling using FCs usually displays very high superheat (e.g., ~30°C for FC-72 on SiO₂ [10]) at boiling incipience while CHF may happen at superheat ~50°C, showing a small allowable temperature range of nucleate boiling.

6.2 Theory and Design

6.2.1 Meniscus Shape on Artificial Cavities for Enhanced Boiling Transfer

Following the long-proposed approach [7], [8] in the literature that microscale cavities with a re-entrant shape would be more resistant against flooding (Figure 6-1), we developed doubly re-entrant structures that can suspend all liquids including FCs in the Chapter 5. As shown in the first row of Figure 6-1, the wall superheat, which is caused by Laplace pressure ($\Delta p = p_v - p_l > 0$) between the vapor and liquid, is the same for cylindrical, re-entrant, or doubly re-entrant cavities when they all have the same mouth radius R_m . However, this static analysis does not guarantee the vapor embryo can sustain during boiling since a film of liquid might be pushed into the cavity after a bubble leaves [2]. Therefore, the level of resistance that a cavity can provide to prevent liquid penetration determines the stability of nucleate boiling. As shown in the second row of

Figure 6-1, cylindrical (or conical) cavities provide no resistance to prevent liquid flooding and re-entrant cavities provide little resistance ($\Delta p = 0$) while doubly re-entrant cavities prevent liquid penetration even when $\Delta p < 0$, i.e., a convex meniscus towards the cavity.

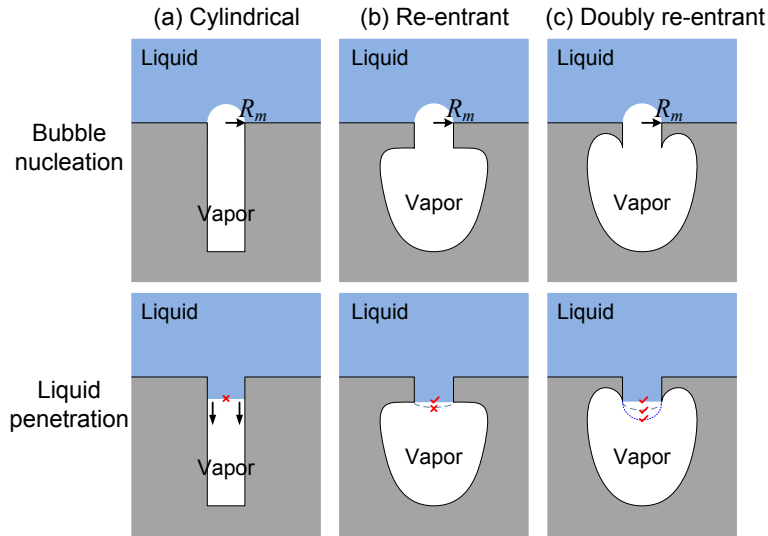


Figure 6-1 Three types of cavities in literature to enhance boiling nucleation. With identical cavity mouth radius R_m , all three types are to nucleate at the same low superheat. However, perfectly wetting liquids like FC-72 may penetrate into the cavity during a bubble departure even if it is stable under static conditions. Our goal is to add more protection by making the cavity doubly re-entrant.

6.2.2 Theoretical Temperatures of Boiling Incipience and Dormancy

The incipient boiling temperature for a bubble embryo with radius R_b is derived as follows. We assume that (1) vapor inside the bubble is an ideal gas; (2) the temperature is continuous across the meniscus, i.e., the liquid temperature at the top of the bubble equals to the vapor temperature right inside the top of the bubble. To ensure boiling happens, the liquid right on top of the bubble should at least be at the saturation pressure p_{sat} so that it

can be turned into vapor and the bubble grows. The pressure of the bubble (i.e., vapor) over the liquid is given by the Laplace pressure,

$$\Delta p = p_v - p_l = \frac{2\gamma}{R_b} \quad (6.1)$$

where p_v is the pressure of the vapor inside the bubble (assuming uniform), p_l is the liquid pressure at the top of the bubble, and γ is the liquid surface tension at saturation point. Therefore, the vapor temperature is higher than the saturation temperature according to the ideal gas law. Since we assume no temperature jump between the liquid and vapor across the meniscus, the liquid temperature equals to the vapor temperature, i.e., the liquid is superheated, as shown in Figure 6-2.

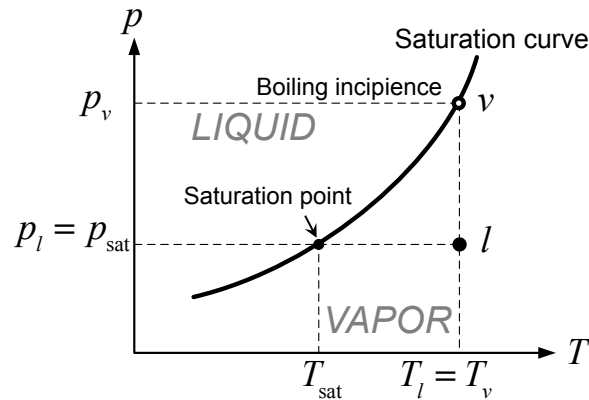


Figure 6-2 Pressure-temperature relationship (p - T) of a boiling bubble

For an isothermal phase change process and we assume the density of liquid is much larger than vapor so that $1/\rho_v - 1/\rho_l \approx 1/\rho_v$, the Clausius-Clapeyron equation [7] gives,

$$T_l - T_{\text{sat}} = \frac{2\gamma}{R_b} \frac{T_{\text{sat}}}{\rho_v h_{lv}} \quad (6.2)$$

where T_l is the liquid temperature, T_{sat} is the saturation temperature, ρ_v is the density of the vapor, h_{lv} is the latent heat of vaporization. For a circular cavity with mouth radius R_m , the maximum superheat is given by the smallest radius of the bubble, which equals to the cavity mouth radius R_m . Therefore the superheat required for boiling on these cavities is,

$$T_l - T_{\text{sat}} = \frac{2\gamma}{R_m} \frac{T_{\text{sat}}}{\rho_v h_{lv}} \quad (6.3)$$

6.2.3 Shift of Saturation Curve by Capillary Condensation

Due to the highly wetting of FCs, even when they can be suspended on doubly re-entrant structures and displays a non-wetting appearance, they might condense in concave corners below the saturation temperature, i.e., capillary condensation. Capillary condensation originates from the pressure difference of a curved meniscus (i.e., Laplace pressure) and has been described by the Kelvin equation shown below.

$$\ln \frac{p_{v_eq}}{p_{\text{sat}}} = \frac{2\mathcal{H}\gamma V_{m_l}}{\mathcal{R}T} \quad (6.4)$$

where p_{v_eq} is the equilibrium vapor pressure of the curved meniscus, p_{sat} is the saturation vapor pressure of the flat meniscus, $\mathcal{H} = 1/2 \cdot (1/R_1 + 1/R_2)$ is the mean curvature of the meniscus as defined from the Young-Laplace equation, γ is the liquid-vapor surface tension, V_{m_l} is the liquid molar volume given by the ratio of molar mass to mass density, i.e., M/ρ , \mathcal{R} is the ideal gas constant and $\mathcal{R} = 8.31 \text{ J}/(\text{mol} \cdot \text{K})$, and T is the temperature. \mathcal{H} is positive when the radius of curvature is inside liquid phase and \mathcal{H} is negative when the radius is inside vapor phase. Hence, for FCs, \mathcal{H} is negative which results in $p_{v_eq} < p_{\text{sat}}$. This can be understood as for a given temperature T , the equilibrium vapor pressure for a curved FCs' meniscus (e.g., at concave corners) is smaller than a flat meniscus. As shown

in Figure 6-3, this change in equilibrium pressure can be represented as a vertical downward shift of the saturation curve. If the pressure is fixed instead of temperature, then the shift of saturation curve can be viewed as an increase of saturation temperature T_{v_eq} . In other words, for a given pressure (e.g., p_{sat}), capillary condensation causes the equilibrium vapor temperature for a curved FCs' meniscus to be larger than a flat meniscus.

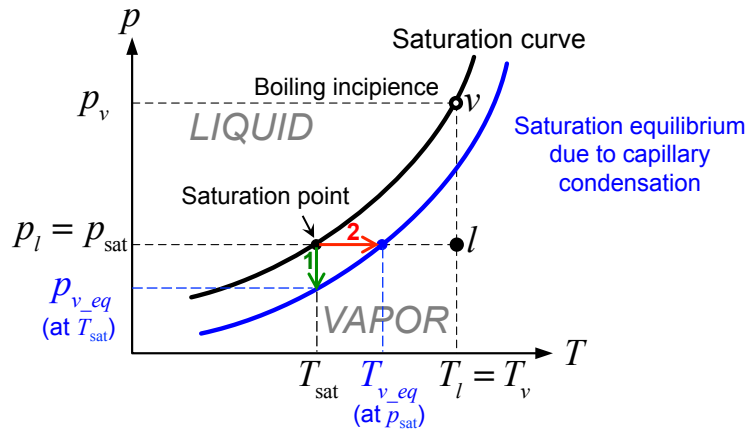


Figure 6-3 Schematic illustration of how the saturation equilibrium changes by capillary condensation. The changes can be understood as a downward shift of saturation pressure for a given temperature (green arrow) or a rightward shift of saturation temperature for a given pressure (red arrow).

The consequence of such shift of saturation curve by capillary condensation is that artificial cavities can be wetted/flooded even when the system is superheated. From Eq. 6.4, the maximum capillary condensation is caused by the minimum radius of curvature of the meniscus which is determined by the minimum radius of curvature of the roughness of the surface (R_r). We quantitatively calculate the extent of the shift on saturation temperature ΔT_{sat} with R_r for FC-72 in Figure 6-4. For example, a surface with

roughness of minimum radius of 25 nm will have a saturation temperature at $\sim 58.4^\circ\text{C}$ at 1 atm, which is $\sim 1.85^\circ\text{C}$ higher than the normal saturation temperature (56.6°C).

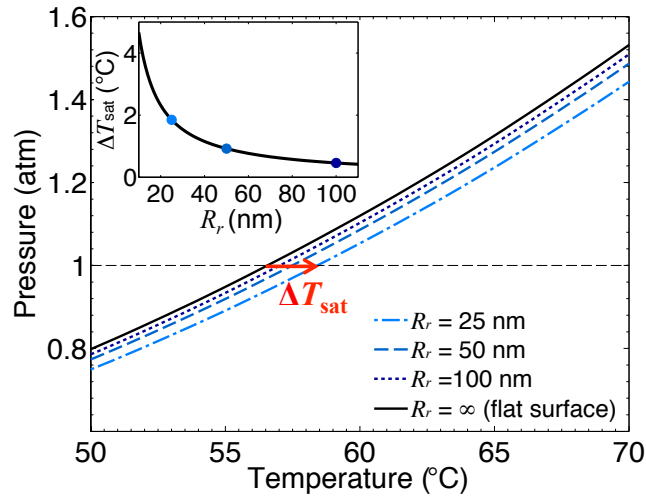


Figure 6-4 Normal saturation curve of a liquid-vapor system and a couple of curves shifted towards a higher saturation temperature due to the capillary condensation on a rough wetting surface. The extent of the shift is dictated by the Kelvin equation such that the smaller the minimum radius of curvature (R_r) of the surface roughness the larger the increase in saturation temperature (inset).

6.3 Experiments

6.3.1 Chip Design and Fabrication

Unlike other research that studied the overall heat transport performance, we focus on comparing with other artificial cavities (Figure 6-1a,b) to confirm the effectiveness of doubly re-entrant cavities (Figure 6-1c). Each test chip has a collection of cavities only at the center to help observing the active nucleation. Two sizes ($\phi 5 \mu\text{m}$ and $\phi 10 \mu\text{m}$ opening) for each of the three cavity types (Figure 6-1) are fabricated and tested.

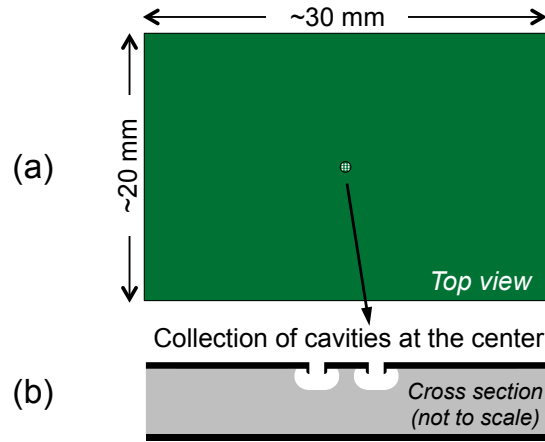


Figure 6-5 Design of boiling chips to study the nucleation dynamics. (a) The chip is designed to be 20 mm by 30 mm with a collection of cavities in the central area while leaving the outer surface smooth. (b) shows the cross section on one boiling chip that consists of doubly re-entrant cavities.

Following the process we developed for superomniphobic SiO_2 surfaces, cylindrical and re-entrant cavities are fabricated as a subset of the process for doubly re-entrant cavities. Figure 6-6 shows the fabrication process flow to create doubly re-entrant cavities in which the Si deep anisotropic etching has been removed before the last step to create smoother cavities and eliminate sharp corners at the bottom.

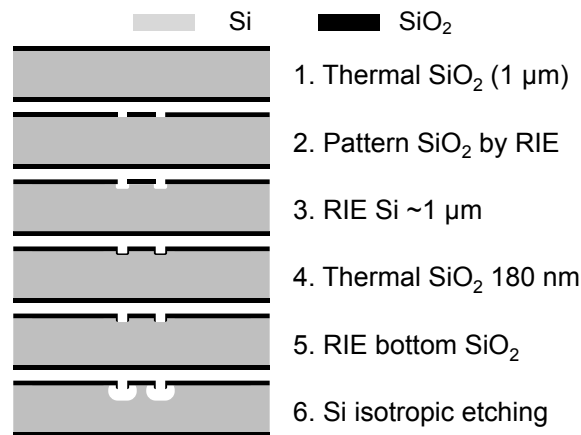


Figure 6-6 Process to fabricate boiling chip consists of doubly re-entrant cavities by micro and nano Si machining. Different from the superomniphobic doubly re-entrant posts shown in Chapter 5, the microstructured cavities are isolated holes that are not connected to atmosphere.

6.3.2 Pool Boiling Tests

Figure 6-7 shows the apparatus for pool boiling experiment. By controlling the temperature of the FC-72 pool with the outer water bath, the FC-72 and the chip are at the same temperature at all times. For each test, the chip was heated separately on a hot plate before placed in the heated FC-72 pool to avoid capillary condensation inside the cavities before the test. During a controlled cooling ($-0.08^{\circ}\text{C}/\text{minute}$), the nucleation was monitored with the superheat measured in sync. When nucleation ceased, the cooling stopped and the temperature was maintained. To observe whether the ceased nucleation can restart, we reapplied heat by raising the temperature of the water bath. A computer program was developed to collect the temperature, pressure data from various sensors and monitor the nucleation (from a camera) at the same time. To better achieve an equilibrium state, the FC-72 pool and the boiling chip are levitated so that they were heated/cooled by the water bath or the FC-72 only.

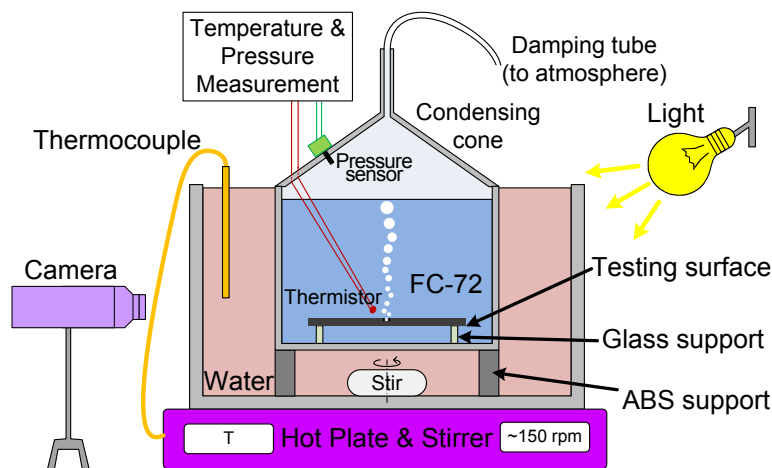


Figure 6-7 Experimental setup of FC-72 pool boiling test. A water bath is feedback-heated and served as a uniform heat source for FC-72 pool. FC-72 is degassed before experiment. A thermistor ($\pm 0.1^{\circ}\text{C}$ accuracy) placed close to the test chip measures the liquid/chip temperature and connects with feedthrough to outside. A condensing cone with a damping tube is used to recollect FC-72 condensate while providing atmospheric pressure during the experiment.

6.4 Results and Discussion

6.4.1 Fabrication Results

Figure 6-8 shows the fabricated doubly re-entrant cavities ($\phi 10 \mu\text{m}$). The collection of cavities in the center of the chip is shown in Figure 6-8(a) while the cross sections are shown in Figure 6-8(b) to (d). The minimum radius of the curvature of the cavity was located as the inner corner of the doubly re-entrant structure and measured to be $\sim 30 \text{ nm}$, as shown in Figure 6-8(d). The roughness of the cavity surface from Si isotropic etching was found better by using SCREAM recipe in DRIE comparing to XeF_2 etching but still visible in Figure 6-8(c) and (d).

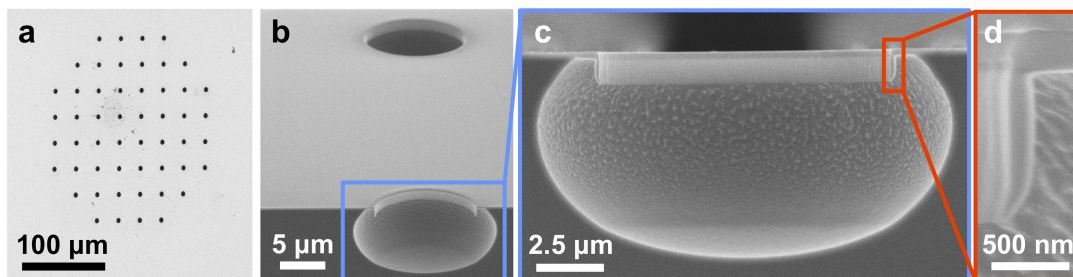


Figure 6-8 SEM micrograph of fabricated boiling chips. (a) Top view of the collections of microstructured cavities at the center of the chip. (b) Angled cross-sectional view of the doubly re-entrant cavities. (c) Cross-sectional view of one doubly re-entrant cavity. (d) Magnified cross-sectional view of the vertical overhang of the doubly re-entrant structure.

6.4.2 Measurements of Nucleation Incipience

When the chip was put into the preheated ($\sim 60.6^\circ\text{C}$, viz., 4°C superheat) FC-72 pool, nucleate boiling started on all three types of cavities tested. However, nucleation on cylindrical cavities ceases even when the FC-72 was superheated by 4°C , showing that the nucleation is not stable on cylindrical cavities and they got wetted within 10 seconds even with active nucleation. Nucleation on $\phi 5 \mu\text{m}$ cavities continued for ~ 6 minutes but

then ceased even when the superheat was maintained at 4°C. Nucleation on $\phi 10 \mu\text{m}$ re-entrant cavities and both $\phi 5 \mu\text{m}$ and $\phi 10 \mu\text{m}$ doubly re-entrant cavities continued for ~30 minutes steadily. We then started the controlled cooling at the rate of -0.08°C per minute and monitored the nucleation with the temperature and pressure. During the cooling, nucleation on the doubly re-entrant cavities persisted down to a very small superheat ($1.81\text{-}1.97^\circ\text{C}$ for $\phi 5\mu\text{m}$ cavities, $0.88\text{-}1.08^\circ\text{C}$ for $\phi 10 \mu\text{m}$ cavities), matching Eq. 6.3 near perfectly (solid circles in Figure 6-9). Nucleation on $\phi 10 \mu\text{m}$ re-entrant cavities ceased early at a larger superheat (open square in Figure 6-9), suggesting that the FC-72 still penetrated into the cavities during a bubble departure [2]. Those results clearly show that the doubly re-entrant structures protect the cavities from liquid penetration and therefore capable of not being wetted during the bubble departure. Since $\phi 10 \mu\text{m}$ re-entrant cavities got wetted during active nucleation, we knew that the Laplace pressure did become negative sometimes (i.e., $\Delta p = p_v - p_l < 0$), along with the bubble departure most likely.

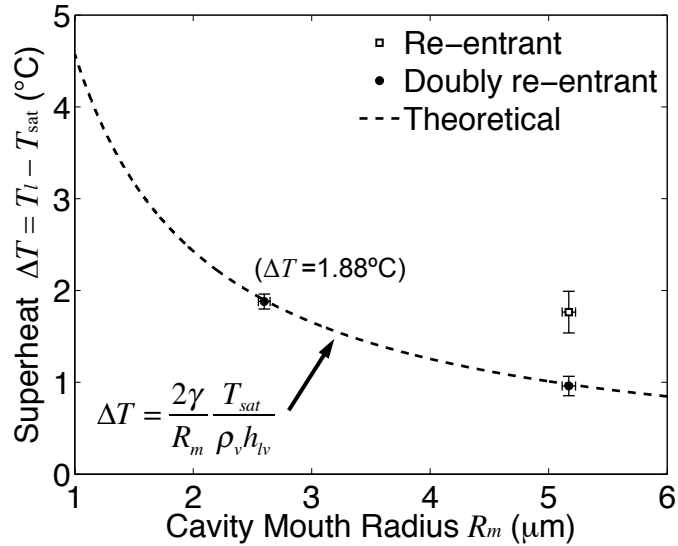


Figure 6-9 Comparison of liquid superheats required to maintain nucleation on different cavities ($n = 3$ for each experimental datum). On both the doubly re-entrant cavities ($\phi 5 \mu\text{m}$ and $\phi 10 \mu\text{m}$), the experimental data matched perfectly with the theoretical prediction (standard deviation $< 0.1^{\circ}\text{C}$). On the re-entrant cavities of $\phi 10 \mu\text{m}$, more superheat was needed than the theory to maintain nucleation. On the re-entrant cavities of $\phi 5 \mu\text{m}$ and all the cylindrical cavities, nucleation ceased even before the cooling started and therefore no data were obtained for those cavities.

6.4.3 Restart Boiling Nucleation from Doubly Re-entrant Cavities

Whenever the chip ceased nucleation, we maintained the temperature of FC-72 pool and reapply heat to see whether nucleation can start with small superheat which only happens when the nucleation sites have not been fully flooded. We found that only the doubly re-entrant cavities can resume nucleation when the chip was heated after leaving it for ~ 5 minutes without nucleation. Figure 6-10 shows this phenomenon and data recorded on $\phi 5 \mu\text{m}$ doubly re-entrant cavities. The time from 0 to t_1 is the controlled cooling period, and the nucleation ceased at time t_1 . FC-72 temperature continued to decrease due to thermal inertia and then increased as we reapplied heat. At time t_2 , nucleation resumed at $\sim 1.85^{\circ}\text{C}$, which matched the temperature they ceased to nucleate at t_1 (i.e., $\sim 1.88^{\circ}\text{C}$ shown in Figure 6-9). This is strong evidence that doubly re-entrant cavities can preserve

vapor and not wetted even when nucleation ceased. This is also the first time a refrigerant such as FC-72 can resume nucleation after it ceased at such a low superheat. In comparison, the cylindrical and re-entrant cavities could not reactivate nucleation even when other random spots inside the FC-72 pool started to nucleate ($\sim 7^\circ\text{C}$). It may require a superheat similar to that for a smooth surface ($\sim 30^\circ\text{C}$ [10]) to restart nucleation from those flooded cavities.

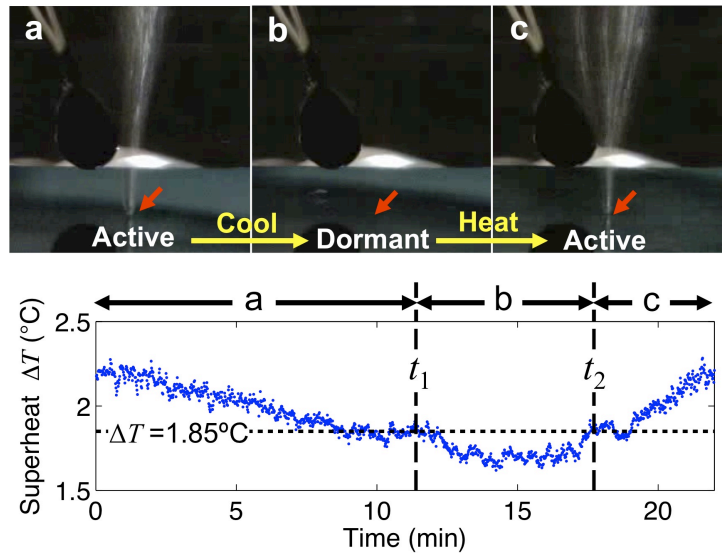


Figure 6-10 Nucleation ceasing and resuming on doubly re-entrant cavities. Snapshots show the nucleation stopped upon cooling and restarted upon heating on $\phi 5 \mu\text{m}$ doubly re-entrant cavities (red arrow). Note that at both t_1 (stop) and t_2 (restart), the liquid superheat is $\sim 1.85^\circ\text{C}$, matching the theory in Figure 6-9.

6.4.4 No Resume of Boiling Nucleation if Cooled Below Saturation Point

Because doubly re-entrant cavities were proposed to sustain certain subcooling [7], [8], we also tried to reduce the FC-72 temperature below the saturation point and then reheat to see whether nucleation can restart at low superheat. Unfortunately, none of the tested surface could resume nucleation even at high superheat when some other random spot in

the pool start to nucleate (e.g., upon shock). This indicated that the doubly re-entrant cavities we fabricated were flooded during subcooling. Moreover, even without going to subcooling, nucleation could not be started when FC-72 temperature was reduced closer the saturation temperature. For example, on $\phi 5 \mu\text{m}$ doubly re-entrant cavities (same chip as Figure 6-10), nucleation could no longer be resumed when the superheat was below 1.5°C . We suspected this was caused by capillary condensation discussed in Session 6.2.3. We used the measured minimum radius of curvature on our fabricated surface ($\sim 30 \text{ nm}$) and calculated the increase of saturation temperature from capillary condensation to be $\sim 1.54^\circ\text{C}$, very closed to the superheat below which cavities were flooded. Although matching almost perfectly for this single datum, we believe more controlled experiments are need to confirm that it is the capillary condensation that causes the shift of saturation point and leads to early phase change to liquid inside the cavities which triggers FC-72 flooding.

6.5 Summary

We report a surface cavity from which boiling nucleation in FC-72 (from 3M™) can be restarted after being stopped. To our best knowledge, this is the first success with the electronics refrigerant FC-72, which has the lowest surface tension of all liquids and wets all materials (even Teflon) perfectly so that all cavities get flooded once nucleation stops. The developed cavity has a microscale opening ($\phi 5 \mu\text{m}$ hole) with nanoscale details of a doubly re-entrant shape and restarted nucleation at mere $\sim 1.8^\circ\text{C}$ of superheat. In stark comparison, both a cylindrical cavity and a re-entrant cavity with the same opening could

not restart nucleation upon $\sim 7^\circ\text{C}$ of superheat and may require a superheat similar to that for a smooth surface ($\sim 30^\circ\text{C}$).

6.6 References

- [1] E. Pop, “Energy dissipation and transport in nanoscale devices,” *Nano Res.*, vol. 3, no. 3, pp. 147–169, 2010.
- [2] V. K. Dhir, “Boiling heat transfer,” *Annu. Rev. Fluid Mech.*, vol. 30, no. 1, pp. 365–401, 1998.
- [3] Y. Fujita and Q. Bai, “Critical heat flux of binary mixtures in pool boiling and its correlation in terms of Marangoni number,” *Int. J. Refrig.*, vol. 20, no. 8, pp. 616–622, Dec. 1997.
- [4] S. M. You, J. H. Kim, and K. H. Kim, “Effect of nanoparticles on critical heat flux of water in pool boiling heat transfer,” *Appl. Phys. Lett.*, vol. 83, no. 16, pp. 3374–3376, Oct. 2003.
- [5] G. Hetsroni, J. L. Zakin, Z. Lin, A. Mosyak, E. A. Pancallo, and R. Rozenblit, “The effect of surfactants on bubble growth, wall thermal patterns and heat transfer in pool boiling,” *Int. J. Heat Mass Transf.*, vol. 44, no. 2, pp. 485–497, Aug. 2000.
- [6] R. L. Webb, “The evolution of enhanced surface geometries for nucleate boiling,” *Heat Transf. Eng.*, vol. 2, no. 3–4, pp. 46–69, 1981.
- [7] V. P. Carey, *Liquid-vapor phase-change phenomena*. New York: Taylor & Francis Group. LLC, 2008.
- [8] C.-J. Kim, “Structured Surfaces for Enhanced Nucleate Boiling,” MS thesis, Iowa State University, 1985.
- [9] A. R. Betz, J. Jenkins, C.-J. Kim, and D. Attinger, “Boiling heat transfer on superhydrophilic, superhydrophobic, and superbiphilic surfaces,” *Int. J. Heat Mass Transf.*, vol. 57, no. 2, pp. 733–741, 2013.
- [10] S. M. You, A. Bar-Cohen, and T. W. Simon, “Boiling incipience and nucleate boiling heat transfer of highly wetting dielectric fluids from electronic materials,” *Compon. Hybrids Manuf. Technol. IEEE Trans. On*, vol. 13, no. 4, pp. 1032–1039, 1990.

Chapter 7 Summaries and Future Directions

7.1 Dissertation Summaries

In this dissertation, we have presented scientific studies on the shapes of liquid meniscus at micrometer scale and engineering applications of meniscus shaping by micro and nano fabrication. Our research has focused on two critical parameters in studying interfacial phenomena: *surface tension* and *contact angle*. Because the interfaces of a liquid in microscale normally involve three phases – solid, liquid, and vapor, we can study and engineer a meniscus by controlling the conditions imposed on them.

We start our journey with a study of the two parameters for a non-toxic liquid metal Galinstan[®], as its meniscus shape is highly affected by the oxygen content in the vapor phase. We have measured the surface tension and contact angles of Galinstan[®] with and without surface oxidation and showed the dramatic difference in its meniscus shape under different oxygen levels. In the second study, we generalize the Cassie-Baxter model, which describes the contact angle of a liquid levitated on surface structures. The study proposed a friction-based model to generalize the Cassie-Baxter model from its original pure static and 2-D description to a dynamic and 3-D description. The generalized model agreed well with the contact angle data reported in literature.

Next, we have demonstrated three different examples of meniscus shape engineering through micro and nano fabrication for practical applications. First, a low-friction electrically conductive liquid-ring bearing has been developed to mechanically and electrically support a micro rotary stage. With the menisci shaped through surface micromachining and selective chemical patterning, the liquid-ring bearings have been proven to provide vertical, horizontal, and anti-tilting stabilities while lubricating the

motion to start and maintain rotation. Additionally, utilizing the direct electrical pathway through a couple of liquid rings filled with a conductive ionic liquid, electrostatic actuation with position sensing has been demonstrated. The presented liquid-ring supported micro rotary stage has displayed a friction hundreds of times less than existing micro-bearings while providing a direct power transmission to the top of an infinitely rotating component. Second, we have advanced the theory of liquid-repellent surfaces by successfully repelling all liquids on a micro and nano structured SiO₂ surface without any coating. Although SiO₂ is a completely wettable material, we have discovered the key micro and nano geometries to suspend a meniscus so that it can repel any liquid regardless of the inherent chemistry of the solid material. This is the first truly superomniphobic surface that can repel all liquids including fluorinated solvent such as FC-72, which completely wets all existing materials and have never previously been found beading up on any surface. Third, we have addressed one of the fundamental issues in electronic cooling with refrigerants. By utilizing the liquid-repellent theory developed above, we have shown, for the first time, certain types of artificial cavities on the solid surface can enhance nucleate boiling of refrigerants. In some experimental conditions, the nucleate boiling was shown to restart even after it has been stopped. However, the meniscus around boiling point is exceedingly complicated due to the interplay between the liquid, solid, and vapor. More investigation is required to make the nucleate boiling of FC-72 more robust.

7.2 Future Research Directions

Superomniphobic surface have been developed with SiO_2 , using Si micromachining and lithography. New fabrication methods should be developed for superomniphobic surfaces made of polymers, which can be made as a film to laminate on any surface, and metals, which would provide mechanical durability and electrical conductivity. Surfaces made with a gradient of liquid-solid fraction may find application in liquid collection, separation, transportation, etc. For example, water droplets can be collected and transported towards less hydrophobic (i.e., more hydrophilic) spots in space with no gravity. Upon our success on creating super nonwetting surface from a highly wettable material, it would be interesting to see whether the reverse can be realized, i.e., wetting all liquids from a hydrophobic material.

For boiling heat transfer applications, despite the unprecedented success, the current result should be considered of scientific value, because the nucleation did not resume if the surface was cooled below the boiling temperature perhaps due to capillary condensation inside the cavities. Further investigation is needed to understand if the success can be extended to subcooling. A better understanding of liquid adsorption characteristics near boiling point is needed. Model surface cavities with optical transparency and controlled roughness may be fabricated to inspect the liquid adsorption, wetting, and capillary condensation. If the flooding is found to be inevitable during cooling, engineering solutions may be considered next.